FACULDADE DE ENGENHARIA DA UNIVERSIDADE DO PORTO

Computer Aided Detection of Perforating Arteries in CT Angiography

Ricardo Jorge Terroso de Araújo

Mestrado Integrado em Bioengenharia

Supervisor: Hélder Filipe Pinto de Oliveira, PhD

Co-Supervisor: Maria Antónia Vasconcelos, MD

June, 2016

Resumo

As mulheres que sofrem de cancro da mama são frequentemente submetidas à mastectomia. A perda desse orgão representa um peso emocional importante nas suas vidas. Os métodos de reconstrução existentes permitem ultrapassar parte dessa perda e diferentes opções estão disponíveis. Estas podem ser divididas em dois grandes grupos: próteses e uso de tecido autólogo. O último grupo representa uma solução comum, uma vez que o seu uso numa cirurgia de reconstrução tem um carácter mais natural e permanente. Apesar desse tecido poder ser colhido de diferentes locais do corpo, a escolha mais comum é a região abdominal. O retalho DIEP (perfurante da artéria epigástrica profunda), baseado em artérias perfurantes, é a atual técnica padrão para fazer esse tipo de reconstrução, uma vez que permite uma boa vascularização e não envolve remoção de tecido muscular. No entanto, torna necessária a realização de estudos imagiológicos antes do ato cirúrgico, de forma a criar um mapa dos vasos perfurantes e extrair as suas características, o que é essencial para planear a intervenção cirúrgica. Das diferentes técnicas de imagiologia propostas para o estudo, a Angiografia por Tomografia Computadorizada (Angiografia CT) é considerada a modalidade padrão, principalmente devido à sua alta resolução e porque é independente do operador.

Atualmente, a informação relevante dos vasos perfurantes é extraída por um técnico ou um radiologista, após realização da Angiografia CT. Um relatório é elaborado e o cirurgião decidirá a sua abordagem consoante a informação nele presente. Este processo é inerentemente subjetivo e leva a incoerências entre o que é reportado antes da cirurgia e o que é encontrado no bloco operatório. Assim sendo, um método capaz de extrair a informação necessária de forma precisa e objetiva tornaria o processo mais eficaz.

O objetivo desta tese é apoiar a atividade do clínico, através do desenvolvimento de um algoritmo de deteção assistida por computador que permite extrair as informações necessárias de forma precisa, objetiva e semi-automática. A metodologia proposta começa por extrair pontos ao longo da porção subcutânea da perfurante através de um filtro de Kalman que combina informação resultante da análise dos vetores de gradiente locais e uma característica proveniente da imagem 2D da secção transversal da perfurante. A extração do esqueleto termina assim que o processo atinge a fáscia e o último ponto é considerado o local em que o vaso perfura esta camada. Além disso, o calibre é também estimado, de acordo com medidas obtidas ao longo do processo de deteção do esqueleto. Finalmente, a porção intramuscular das perfurantes é detetada através de um algoritmo de caminhos mínimos. Os resultados mostram que a metodologia proposta extraiu corretamente o percurso dos vasos perfurantes. As regiões subcutânea e intramuscular foram estimadas com um erro médio de 1.35 *mm* e 1.06 *mm*, respetivamente. Ainda assim, alguns aspetos merecem foco no futuro, de forma a garantir que algumas das informações necessárias pelo clínico, como o calibre por exemplo, estão a ser devidamente calculadas.

Abstract

Women diagnosed with breast cancer are commonly submitted to mastectomy. The loss of the breast(s) brings a heavy loss to their life. Reconstruction methods allow to overcome an important part of this loss and several options exist. The more natural and permanent character of autologous tissue flaps when compared to implants, makes the former a common solution for the reconstruction procedure. Although the tissue can be collected from different regions of the body, abdominal flaps are preferred to reconstruct the breast shape. The Deep Inferior Epigastric Perforator (DIEP) flap is the current state-of-art method to conduct such type of reconstruction, given that it allows a proper blood supply and decreases the abdominal wall morbidity. However, such technique requires preoperative imaging studies, in order to create a map of the abdominal perforator vessels and to extract their characteristics, which are essential to design a suitable flap. From the several imaging techniques proposed for the effect, Computerized Tomographic Angiography (CTA) is regarded as the state-of-art modality, mainly due to its high resolution and operator independent acquisition.

Currently, the relevant information of the perforators is extracted by a technician or a radiologist after acquiring the CTA data from the patients. Then, a report is created and the surgeon will act according to it. Thus, this process is inherently subjective and might create incoherencies between the preoperative and surgical findings. A method capable of retrieving accurately the required information in an objective and automatic way would bring a major benefit to this process.

The goal of this thesis is to support the clinician activity, with the development of a Computer Aided Detection (CAD) algorithm which is able to detect the required characteristics of the Deep Inferior Epigastric Artery (DIEA) perforators in an accurate, objective and semi-automatic way. The proposed methodology starts by tracking the subcutaneous portion of the perforator using a Kalman filter to join the information given by local gradient vectors and a 2D cross section feature. The tracking procedure ends as soon as it reaches the *fascia*, being the last point the estimation of the location where the vessel perforates this layer. Besides, the caliber is also estimated according to measures extracted throughout the tracking iterations. Finally, the intramuscular portion of the perforator is extracted using a 3D minimum cost path approach. The results show that the methodology was able to correctly detect the course of the DIEA perforators. The mean error of the extracted courses was 1.35 *mm* for the subcutaneous portion and 1.06 *mm* for the intramuscular one. Nonetheless, some aspects still need to be focused in the future, in order to guarantee that some of the information required by the clinician, e.g. the caliber, is being accurately retrieved.

Agradecimentos

Começo por agradecer a todos os que fizeram e/ou fazem parte da minha vida, pois a pessoa que sou hoje deve-se a todos eles.

Esta dissertação é o culminar de muitos esforços direccionados para um objetivo comum. Ao Hélder, que foi incansável no seu papel de orientador. Esteve sempre ali ao lado a apoiar, motivar e apontar o melhor caminho a seguir. Ao João Teixeira, pelas sessões de brainstorming inspiradoras e por todo o apoio que sempre deu. Ao António, que se juntou aos nossos devaneios e pelo percurso que fomos percorrendo juntos. A vocês, Pedro Ferreira, Kelwin, João Monteiro, Eduardo e Ana, por me fazerem sentir que nunca saí de casa. Um obrigado ao Prof. Jaime pela chance de trabalhar com o grupo VCMI e pela sua capacidade de construir uma verdadeira equipa de trabalho. Quero agradecer também à Unidade de Mama do Centro Clínico Champalimaud por possibilitar a realização desta tese, e deixo um agradecimento especial à Dra. Maria Antónia pela cooperação.

À Catarina por todas as etapas que passámos juntos nesta vida universitária e por ter estado sempre presente, nos melhores e piores momentos. Um obrigado por todos os sorrisos que partilhámos. À Cláudia, ao Pedro, à Sofia e à Tânia, uma vez que foram pilares para mim ao longo deste percurso. Obrigado pelos bons momentos que passámos e pelas noitadas na FEUP que enfrentámos com um sorriso cansado na face.

Ao João por tudo o que caminhámos lado a lado. Por todos os momentos em que a vida pregou partidas e fomos capazes de estar lá a apoiarmo-nos. Pela infância feliz que tanta nostalgia me traz. Ao Bruno pelas gargalhadas fáceis e por estar sempre presente. Por toda a força e motivação que sempre transmitiu. Agradeço-vos por todas as histórias que vivemos. Ao Nuno pelo apoio que me deu nesta fase e pela alegria que sempre transmitiu.

À minha família, que sempre me apoiou e me possibilitou ser feliz. Aos meus avós, que me viram e fizeram crescer. Espero continuar a deixar-vos orgulhosos de mim e estou eternamente grato por tudo o que fizeram e fazem por mim. Aos meus tios e aos meus primos por me apoiarem em todas as situações. Ao meu primo João por todos os momentos que passámos juntos e por ser como um irmão para mim. Ao meu pai, que sei que tinha um orgulho enorme em mim e me dá a força necessária para ultrapassar as situações mais adversas. Espero ser quem tu gostavas que eu fosse. À minha mãe, por tudo o que foi capaz de enfrentar para nunca me faltar nada, e por ter sempre acreditado em mim. Nunca te poderei agradecer o suficiente, mas todos os dias dou o meu melhor por ti.

Ricardo Araújo

"A fool thinks himself to be wise,
but a wise man knows himself to be a fool."

William Shakespeare

Contents

List of Figures

List of Tables

List of Abbreviations

1D	One-Dimensional
2D	Two-Dimensional
3D	Three-Dimensional
4D	Four-Dimensional
CAD	Computer-Aided Detection
CT	Computerized Tomography
CTA	Computerized Tomographic Angiography
DICOM	Digital Imaging and Communications in Medicine
DIEA	Deep Inferior Epigastric Artery
DIEP	Deep Inferior Epigastric Perforator
MRA	Magnetic Resonance Angiography
MRI	Magnetic Resonance Imaging
ORG	Ordered Region Growing
SIEA	Superficial Inferior Epigastric Artery
SNR	Signal-to-Noise ratio
TRAM	Transverse Rectus Abdominis muscle
US	Ultrasonography

Chapter 1

Introduction

Breast cancer is a malignant tumour with origin in the breast tissue, as defined by the American Cancer Society. In the United States, it is the leading cause of cancer death in women aged 20 to 59 years, being only surpassed by lung cancer in higher ages. It is estimated that more than 230.000 new cases of breast cancer will affect women in the United States during 2016. This represents about 29% of all new cancer cases and 15% of all cancer deaths among women [1]. However, incidence rates vary around the world. In general, developed countries present higher rates than non-developed countries. In the latter, it is the most common cause of cancer mortality while in the former it is the second one, being exceeded by lung cancer. Developed countries possess more efficient early diagnosis and treatments which leads to a lower mortality rate (25%) than the verified in non-developed countries (37%) [2].

Women who were diagnosed with breast cancer have higher chance of suffering from anxiety and depression resulting from the fear of recurrence, body image disruption, sexual dysfunction and mortality concerns [3]. Although breast conservative methods have shown equivalent survival rates to mastectomy [4], the latter is still a highly recurrent procedure and has even been increasing in some institutions [5, 6, 7]. This might suggest that some patients consider the removal of the entire breast a safer approach to completely eliminate the tumour. The option to reconstruct the breast after mastectomy makes this idea more viable.

Reconstruction methods allow to recreate the breast shape, improving the way how women feel about themselves and their image after their breast(s) was(were) removed. Breast reconstruction rates vary greatly according to the country, region and socioeconomical ground of the patient [8]. The Deep Inferior Epigastric Perforator (DIEP) flap has become the state-of-art technique for autologous tissue breast reconstruction [9].

Medical imaging has been playing a huge role in breast reconstruction since microsurgery started to be required to perform techniques such as the DIEP flap. The viability of these flaps is related to several features of the included perforator(s) [10]. Then, preoperative imaging allows to plan the surgery according to the findings. A method capable of retrieving accurately the required information in an objective and automatic way would play a major role in the field.

1.1 Motivation

Many women affected by breast cancer undergo mastectomy in order to remove the tumour. The lack of breast or shape deformation brings a heavy loss to any woman, since this organ plays a major role throughout their life.

This raises the importance of breast reconstruction, as it allows to reconstruct the breast shape of a woman who did a mastectomy. It is possible to use implants or autologous tissue from other body parts such as tissue from the thighs or abdominal wall [11]. Autologous solutions have been evolving in order to reduce donor-site morbidity [12]. Designing a flap is a complex task, as it involves maximizing its blood supply while minimizing the damage inflicted to the donor tissue. Imaging techniques have been used to preoperatively analyze each patient abdominal wall anatomy, focusing on the vasculature [13]. This gives the surgeon the information he needs to design a good flap and perform the surgery. Computer Tomographic Angiography (CTA) is being used to study the patient anterior abdominal vasculature in order to identify the best flap available for reconstruction [10, 14]. Therefore, it would be useful to have a Computer Aided Detection (CAD) system which could automatically retrieve the caliber and course of the perforator vessels in an accurate and objective manner.

1.2 Objectives

This thesis aims to have an impact on current healthcare services in the area of Breast Reconstruction, by improving the service given to a woman who undergoes mastectomy.

The goal is to support the clinician activity by developing a CAD tool capable of retrieving the necessary characteristics of the Deep Inferior Epigastric Artery (DIEA) perforators in an accurate, objective and semi-automatic manner. This allows to plan the surgery according to objectively retrieved data, instead of relying on subjective findings.

1.3 Contributions

The contributions of this thesis are the following:

- the *Ground Truth* annotation of the perforators included in the available database;
- the proposal of a method for segmenting the anterior abdominal wall *fascia*;
- the development of a vessel tracking framework whose estimations are produced by a Kalman filter which fuses local volume gradient vector information with a correction measure based on the vector gradient field divergence of the 2D cross section of the vessel;
- the estimation of the caliber based on the combination of measures taken throughout the tracking procedure;

- the formulation of an A* based pathfinding method for the detection of perforators intramuscular course.

1.4 Document structure

This document is divided in 6 chapters. The present Chapter introduced the relevance of breast reconstruction and the motivation behind preoperative imaging studies. Besides, the objectives and contributions of this thesis were presented. Chapter 2 starts by describing the anatomy of the anterior abdominal wall and also presents a characterization of the most important breast reconstruction methods and preoperative imaging techniques. Chapter 3 covers the state-of-art of vessel segmentation approaches. In Chapter 4, a brief description of the available database is made. Chapter 5 explains in detail the developed framework for the detection of perforators course and their important characteristics. Finally, Chapter 6 is a conclusion of the findings achieved along this thesis.

Chapter 2

Background

This Chapter presents a set of concepts which are important for this thesis. Section 2.1 briefly describes the abdominal wall anatomy, section 2.2 characterizes the existing breast reconstruction options and, finally, section 2.3 includes an overview of the available medical imaging techniques to perform the preoperative studies.

2.1 Abdominal Wall Anatomy

Section 2.2 will describe breast reconstruction methods that rely on tissue from the abdominal region. This requires that the reader is comfortable with the anatomy of the region, mainly the vasculature. In this section, a brief description of the anatomy of the abdominal wall is presented in subsection 2.1.1, following the description made in [15]. A more detailed characterization of the DIEA and its perforators is made in subsection 2.1.2, following [10].

2.1.1 Abdominal region location and vascularization

The abdomen is a region of the trunk, and is located right below the thorax. It is bounded superiorly by the xiphoid process and costal margins, posteriorly by the vertebral column and inferiorly by the pelvic bones. It comprises a cavity known as abdominal cavity and its surrounding musculomembranous walls. This region can be visualized in Figure 2.1.

Both superficial and deep regions of the abdominal wall are vascularized. More anteriorly, the superior part of the wall is supplied by branches of the musculophrenic artery, while the inferior region is supplied by the medially located superficial epigastric artery and the laterally placed internal thoracic artery. Posteriorly, the superior region of the wall is supplied by the superior epigastric artery while the inferior part is supplied by the medially placed inferior epigastric artery and the laterally placed deep circumflex iliac artery, both branches of the external iliac artery. The superior and inferior epigastric arteries enter the *rectus* sheath and anastomose with each other. This relation is represented in Figure 2.2.

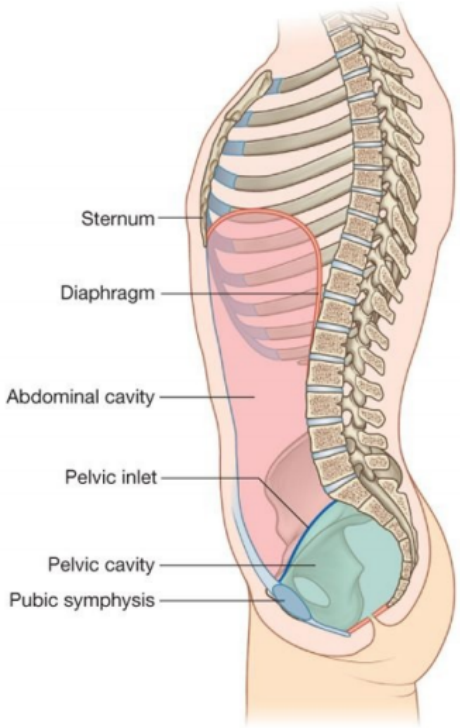

Figure 2.1: Location of the abdominal cavity. Adapted from [15].

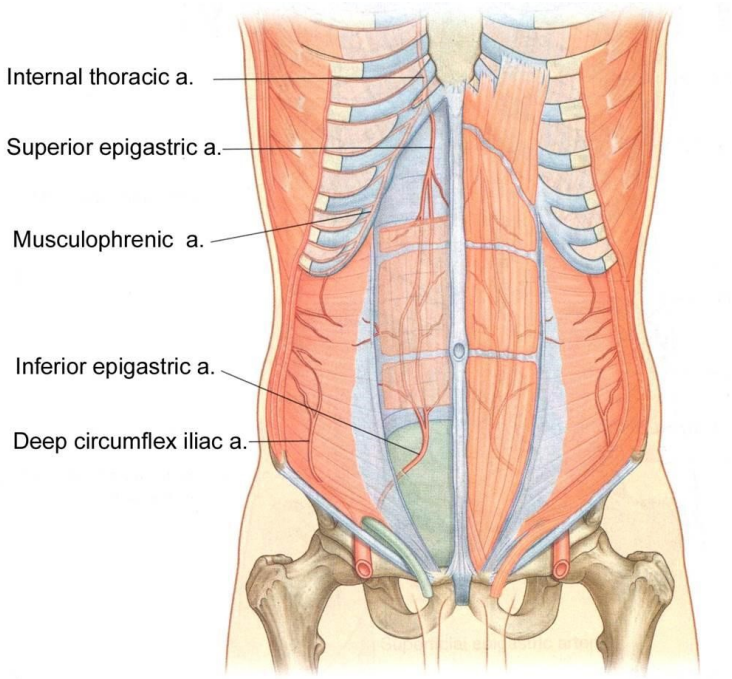

Figure 2.2: Abdominal wall deep vascularization. Adapted from [15].

2.1.2 Deep Inferior Epigastric Artery (DIEA) anatomy

The DIEA has origin in the external iliac artery above the inguinal ligament and ascends along the medial margin of the abdominal inguinal ring (see Figure 2.3). Then, it pierces the *transversalis fascia* and ascends between the *rectus abdominis* muscle and the posterior lamella of its sheath. Finally, it divides in several branches that anastomose with other arteries above the umbilicus.

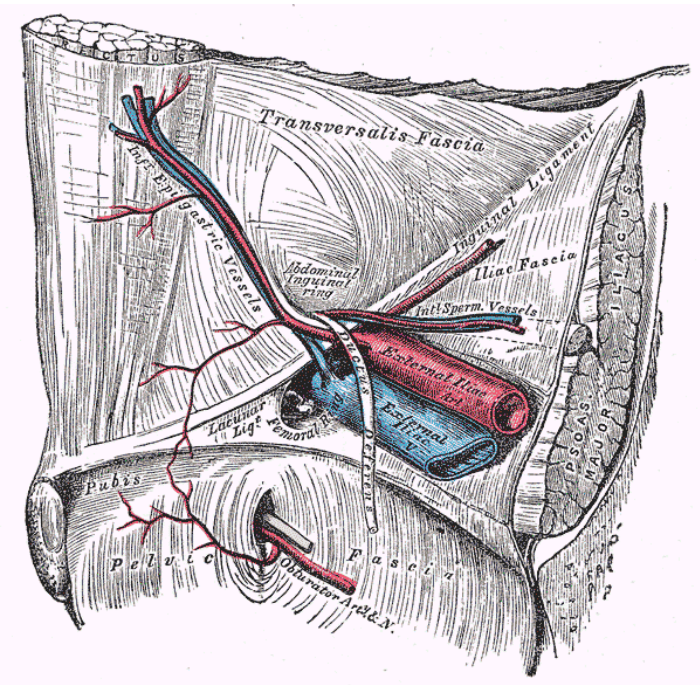

Figure 2.3: Origin of the DIEA from the external iliac artery. Adapted from [16].

Moon and Taylor (1988) described three different patterns of the DIEA, according to the bifurcation type. Type I, II and III have, respectively, one, two and three major trunks at the umbilicus level. These patterns are represented in Figure 2.4.

Despite the anatomical variations of the DIEA, the course that its perforators take is similar (Figure 2.5).

These perforators have origin at the DIEA and penetrate in the posterior surface of the *rectus abdominis* and can have variable intramuscular segment (important detail when planning surgery as shall be explained in Section 2.2). This segment is absent in cases where the artery penetrates a musculotendinous intersection. Usually, this segment perforates the anterior surface of the *rectus* sheath and the anterior layer of the fascial sheath. Alternatively, it can have a varying subfascial segment between those two regions. The subcutaneous segment may present several course and branching configurations and it involves several anastomoses with the superficial inferior epigastric artery (SIEA).

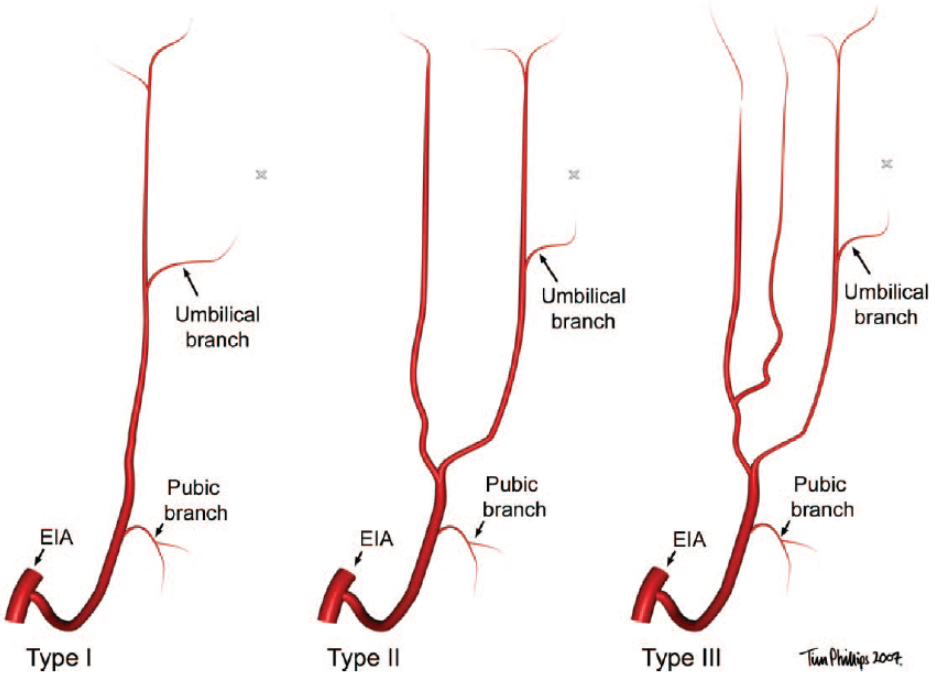

Figure 2.4: DIEA classification described by Moon and Taylor. Adapted from [10].

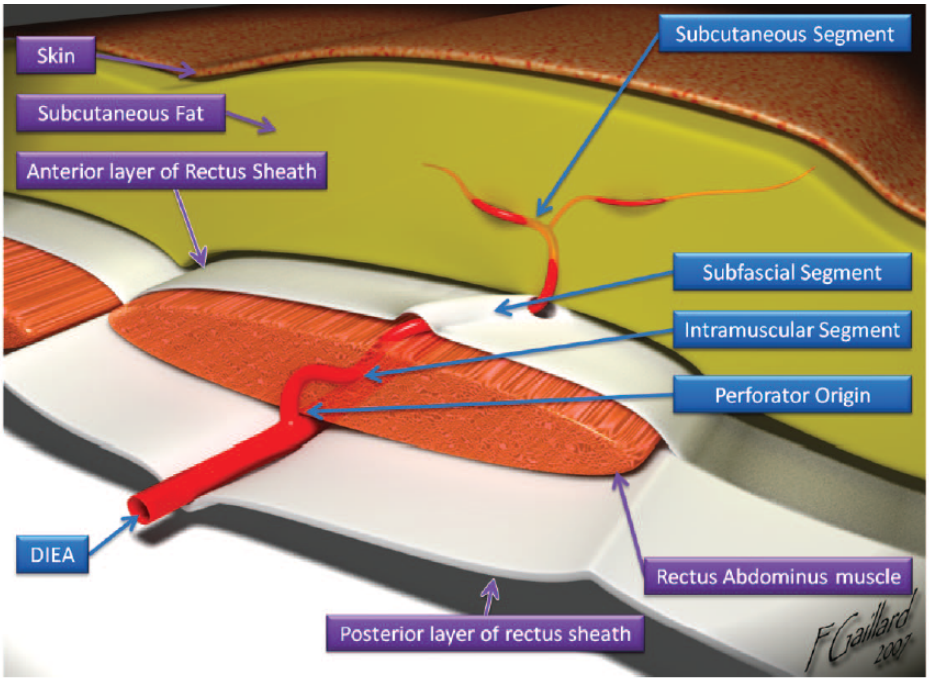

Figure 2.5: 3D illustration of the course of a perforator. Adapted from [10].

2.1.3 Summary

This section provided a brief description of the anatomy of the human body which is relevant to understand the content covered in this thesis. In the first subsection, the abdominal region was located in the body and its vasculature was analyzed. A higher focus was given to the anatomy of the DIEA and its perforators in the second subsection, since this thesis focuses on the segmentation of those vessels. Besides, the anatomical characteristics of the different perforators is crucial when designing a flap, as will be seen in Section 2.2.

2.2 Breast Reconstruction

Typically, breast reconstruction is performed during mastectomy or a short period after. If not, the process can still be undertaken years after the removal of the breast(s).

To reconstruct the breast shape, the surgeon has several alternatives, although the patient specific situation might turn some of them more reliable. They include the use of artificial implants and flaps of different autologous tissues. Implants have been favored by surgeons but autologous tissue flaps are seeing their use increased in the last decades due to the evolution of microsurgery.

This chapter describes the different possibilities for breast reconstruction and their advantages and disadvantages.

2.2.1 Implant based reconstruction

This option requires less surgery than flap reconstruction since it does not involve an additional donor site surgery. Even then, implants must be replaced from time to time, requiring multiple surgeries in the future [17].

Implants are a good option for women who:

- do not have extra belly tissue to use for flap reconstruction (same occurs in other regions of the body);
- want to avoid incisions and/or sacrifice muscle;
- do not need radiation therapy, since it might bring problems after implant reconstruction;
- do not want to be submitted to longer operations;
- do not mind about surgically altering their natural breast in order to achieve symmetry.

The implant might contain saline solution, silicone, or both. Silicone implants have two variants: the first has a single chamber and the latter has a second chamber filled with saline solution posterior to the silicone filled chamber [11].

The reconstruction procedure also has two versions: the first consists in only one step, where the implant is inserted in a retropectoral position. The second has two steps, starting by the retropectoral insertion of a tissue expander which is gradually filled with saline solution until

the soft tissue stretches adequately; then the expander is removed and a permanent implant is put in its place. This approach is preferred for patients with little residual cutaneous tissue at the mastectomy defect and/or those at risk for suboptimal skin healing [11].

2.2.2 Autologous Reconstruction

Also called autogenous reconstruction, it uses tissue from another place in the body to reconstruct the breast. This tissue, also known as flap, contains skin, fat and in some cases, muscle, and it comes from the belly, the back, buttocks or inner thighs. In this description, only abdominal flaps are considered, since they are the most common for reconstructing the breast shape. The reasons behind such fact are the similarity between the tissues, high flap design versatility and associated low donor-site morbidity. Besides, the goal of the thesis is the segmentation of abdominal vessels, the DIEA perforators.

When the tissue is completely separated from its blood vessels, the flap takes the designation of free flap. When this is not the case and the tissue is moved under the skin, the term is pedicled flap. The latter kind of flaps have been around longer and are easier to perform, such that they tend to be widely available. Free flaps require surgeons capable of performing microsurgeries in order to attach tissue vessels to the breast ones, which is a skill that only some possess [17].

Autologous reconstruction has several advantages over implants:

- Lasts longer given that implants have to be replaced every 10 or 20 years;
- Similarity of tissues leads to natural feeling, although little sensation, at most, is achieved;
- Foreign body reactions are avoided.

In the next subsections, different techniques for breast reconstruction using abdominal flaps are presented, namely the Transverse *rectus abdominis* Muscle (TRAM) flap, the DIEP flap and the SIEA flap.

2.2.2.1 TRAM flap

TRAM is a muscle located in the lower abdomen, between the waist and the pubic bone. In a TRAM flap, there is a reconstruction of the breast with a flap of the skin, fat and a portion of the underlying *rectus abdominis*. This kind of flap is the most common since most surgeons are already familiar with it and because the tissue is similar to the breast one [17]. TRAM flaps are considered to yield superior esthetic results in comparison with both the *latissimus dorsi* myocutaneous flap and prosthetic implants [11]. There are different types of TRAM flaps:

- Pedicled TRAM flap (Figure 2.6): the tissue is moved under the skin up to the chest, keeping the blood vessels attached to their original blood supply in the abdomen. This kind of flap involves a large portion of the muscle and is also known as “muscle transfer” flap. Larger recovery periods are expected. One common problem with this kind of flap is that the moved tissue may not get enough blood circulation and there might occur partial flap loss [17].

- Free TRAM flap (Figure 2.7): blood vessels of the flap are carefully attached to blood vessels of the chest (thoracodorsal or internal mammary vessels), leading to a more robust vascular supply. Over time, it evolved to the "muscle-sparing" free TRAM flap. This involves even less invasive excision due to the precise identification and dissection of each DIEP vessel in the flap. It includes subcutaneous fat and skin such as the TRAM flap and the free TRAM flap, but it incompletely transects the *rectus abdominis* muscle [11].

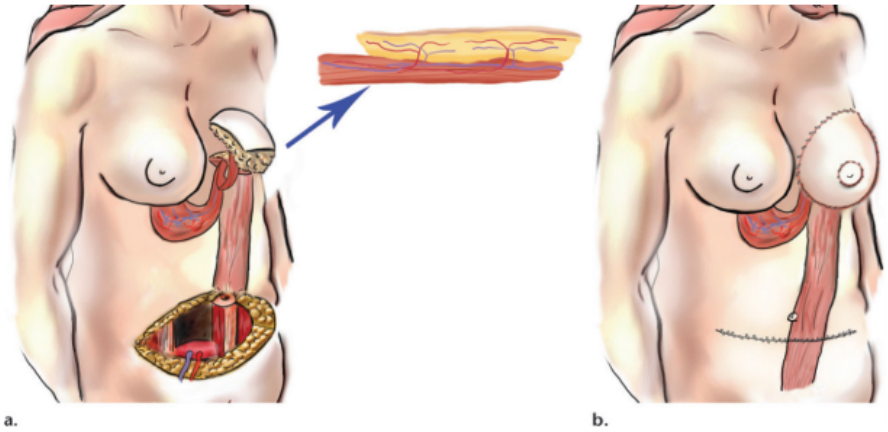

Figure 2.6: Reconstruction with pedicled TRAM flap. The flap is rotated on its vascular pedicle and extended upward from the lower abdomen to the mastectomy site (a), where it is sutured to the residual skin overlying the mastectomy defect (b). Adapted from [11].

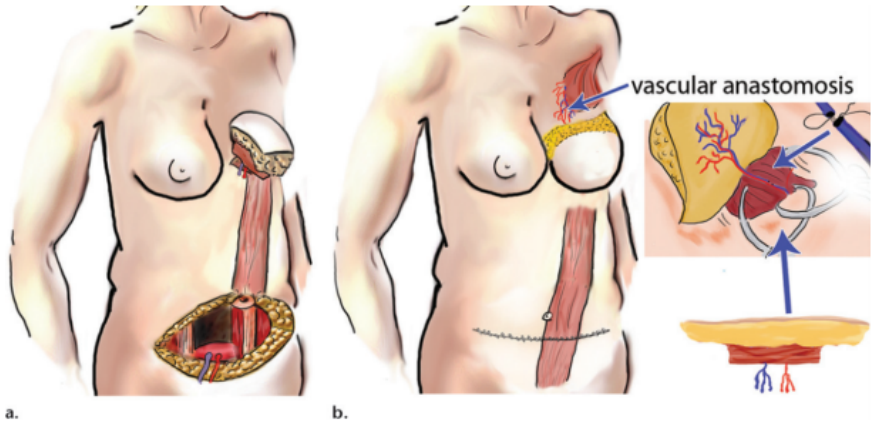

Figure 2.7: Reconstruction with free TRAM flap. (a) tissue is separated from abdominal blood supply and positioned over the mastectomy defect. (b) surgical reanastomosis of the perforating deep enferior epigastric vessels to breast site vessels is performed. Adapted from [11].

Although its popularity, according to [17], a TRAM flap is not adequate in some cases:

- Women without extra belly tissue;
- Women who had multiple abdominal surgeries;

- Women who plan on getting pregnant;
- Women who are concerned about losing strength in their lower abdomen.

2.2.2.2 DIEP flap

A DIEP flap is similar to the already described muscle-sparing free TRAM flap, with the difference that no muscle is used to rebuild the breast. In this flap, fat, skin and blood vessels are cut from the wall of the lower belly and moved to the chest. As this technique involves microsurgery, it is not available at all institutions. Usually women recover more quickly and have a lower risk of losing abdominal strength with this kind of flap when comparing with the TRAM techniques [17]. Although patients do not perceive a significant difference between abdominal donor-site morbidity of free muscle-sparing TRAM flap and DIEP flap reconstructions [18], studies demonstrated greater measured abdominal strength in patients who had breast reconstruction with the latter [12, 19]. In the past few years, the DIEP flap has become the state-of-art in breast reconstruction [9], however, it should be avoided in the following cases [17]:

- Women who do not have enough extra belly tissue, although a "stacked" approach has been proposed;
- Women who already had certain abdominal surgeries;
- Women whose abdominal blood vessels are small or not in the best location to perform a DIEP flap.

A key element for a successful DIEP procedure is the correct choice of the perforator artery that perfuses the flap. This decision is the reason why the success rate is highly variable many times. Table 2.1 describes the relevant characteristics of the DIEA and its perforators that should be considered when planning the DIEP flap surgery.

Rozen *et al.* [20] observed a reduced intramuscular transverse distance (mean of 1.41 *cm*) for perforators of DIEA with type II branching pattern while for type III they observed the biggest distance (mean of 1.73 *cm*). The authors did not detect any association between branching pattern and number of perforators and found that type II were the most common (58%) while type III the most uncommon (16%). Therefore, preoperative knowledge of the DIEA branching pattern can aid the surgeon about which perforator and hemiabdomen to consider for the surgery.

2.2.2.3 SIEA flap

The SIEA flap is very similar to the DIEP flap, except that the vessels that are moved are different. In this case, no incision in the *fascia* is done, what is mandatory in the DIEP flap. This means that this flap does not disturb the muscle at all [17]. Besides the reasons stated for DIEP flap, most women are not eligible for this flap due to:

- Very small superficial blood vessels;

Table 2.1: Relevant perforator characteristics for planning the DIEP flap surgery. Adapted from [10].

Abdominal Wall Artery	Relevant Characteristic	Importance to DIEA Perforator Surgery
DIEA	Caliber	A large-caliber trunk is a more favorable pedicle.
DIEA	Branching pattern (type I, II, or III)	The DIEA branch forms the pedicle for the anastomosis. Type I and type II arteries have perforators with shorter intramuscular segments. Type II arteries often have perforators arranged in rows along each trunk; two or more of these perforators may be dissected to a single trunk. Type II and type III arteries have a lateral branch that is in the vicinity of the motor nerves to the rectus abdominus; dissection of this branch raises the risk of muscle denervation.
DIEA	Any intramuscular course	Any intramuscular course makes dissection of the DIEA more difficult.
DIEA perforator		
Intramuscular perforator	Direction and length	Oblique intramuscular segments require more dissection of the rectus abdominus. Perforators that penetrate a musculotendinous intersection may not have an intramuscular segment and are preferred by some surgeons.
Subfascial perforator	Length and direction	Radiologically, the subfascial segment origin can be confused with the subcutaneous segment origin. Long subfascial segments require careful dissection to preserve the perforator when incising the rectus sheath.
Subcutaneous perforator	Location and caliber	Large-caliber (≥1 mm in diameter) arteries supply a greater volume of adipocutaneous tissue and represent better vascular pedicles. Preoperative knowledge of the subcutaneous segment origin facilitates accurate planning of dissection.
Superficial inferior epigastric artery	Caliber and location	Use of a large-caliber superficial inferior epigastric artery as a vascular pedicle for a free flap is favored by some surgeons.

- Superficial vessels have been cut during a C-section or hysterectomy;

- Non-existence of the superficial system.

2.2.3 Summary

Breast reconstruction techniques give women who undergone mastectomy a chance to reconstruct the removed breast(s), which has a major impact in their life. Although implant based reconstruction is recommended for several situations and is widely used, generally it performs worse than autologous techniques in terms of approximating the natural breast texture. Abdominal flaps weaken the abdominal wall but, for many women, the required abdominoplasty is also seen as a procedure they would like to undergo. The DIEP flap technique was proposed to reduce the donor site morbidity and recovery time associated to the TRAM flaps, with the cost of requiring great surgical expertise. SIEA flaps disturb even less the abdominal wall and should be performed if the patient meets the required conditions, which is not common. These are the details that made the DIEP flap become the state-of-art technique for breast reconstruction using abdominal flaps. Figure 2.8 presents a comparison of the blood supply in free TRAM, DIEP and SIEA flaps. The advantages and disadvantages of these reconstruction techniques can be analyzed in more detail in Table 2.2.

Table 2.2: Advantages and disadvantages of the autologous reconstruction techniques. Adapted from [11].

Autologous Breast Reconstruction Techniques

Type of Autologous Tissue Flap	Year of Origin	Description of Flap Tissue Contents	Vessels Supplying the Flap	Advantages	Disadvantages
Myocutaneous					
Latissimus dorsi flap	1897	Skin, subcutaneous tissue, portion of the latissimus dorsi muscle	Thoracodorsal vessels	More easily created than other autologous flaps, does not result in abdominal wall weakness, has a robust blood supply	Less pleasing esthetically than TRAM and DIEP flaps; results in a large scar at the middle back and, frequently, a seroma
Pedicled TRAM flap	1982	Skin, subcutaneous tissue, portion of the rectus abdominis muscle	Deep superior epigastric vessels	Produces a more natural breast texture than prosthetic implants, allows simultaneous abdominoplasty	Surgical procedure is more complex than that used with prosthetic implants, leads to loss of abdominal wall strength
Free TRAM flap	1976–1979	Skin, subcutaneous tissue, smaller portion of rectus abdominis muscle than in pedicled TRAM flap	Deep inferior epigastric vessels	Produces a more natural breast texture than prosthetic implants, allows simultaneous abdominoplasty	Surgical procedure is more complex than that used with prosthetic implants, leads to loss of abdominal wall strength
Free muscle-sparing TRAM flap	1976–1979	Skin; subcutaneous tissue; and two to three individually dissected perforating vessels, each with a small cuff of surrounding rectus abdominis muscle fibers	Deep inferior epigastric vessels	Less invasive dissection of rectus abdominis muscle helps minimize loss of abdominal wall strength; use of surgical mesh is avoided; has a more adequate blood supply, with fewer ischemic complications, than pedicled TRAM flaps	Requires greater surgical expertise and more time in the operating room, with a higher associated risk of necrosis due to venous thrombosis, than pedicled TRAM flaps
Skin and fat					
DIEP flap	1989	Ellipsoid section of lower abdominal skin and subcutaneous fat, selective dissection of one to three perforating vessels arising from the inferior epigastric artery	Deep inferior epigastric vessels	Leads to less donor site morbidity, requires less recovery time	Requires greater surgical expertise, with a high risk of ischemic complications and resultant fat necrosis
SIEA flap	1991	Lower abdominal skin and subcutaneous fat	Subdermal vascular plexus supplied by superficial circumflex iliac artery	Obviates dissection of perforating vessels, requires less surgical time, leads to less donor site morbidity	Has a less robust blood supply than TRAM and DIEP flaps, with a resultant increased incidence of fat necrosis

Note.—DIEP = deep inferior epigastric perforator, SIEA = superficial inferior epigastric artery.

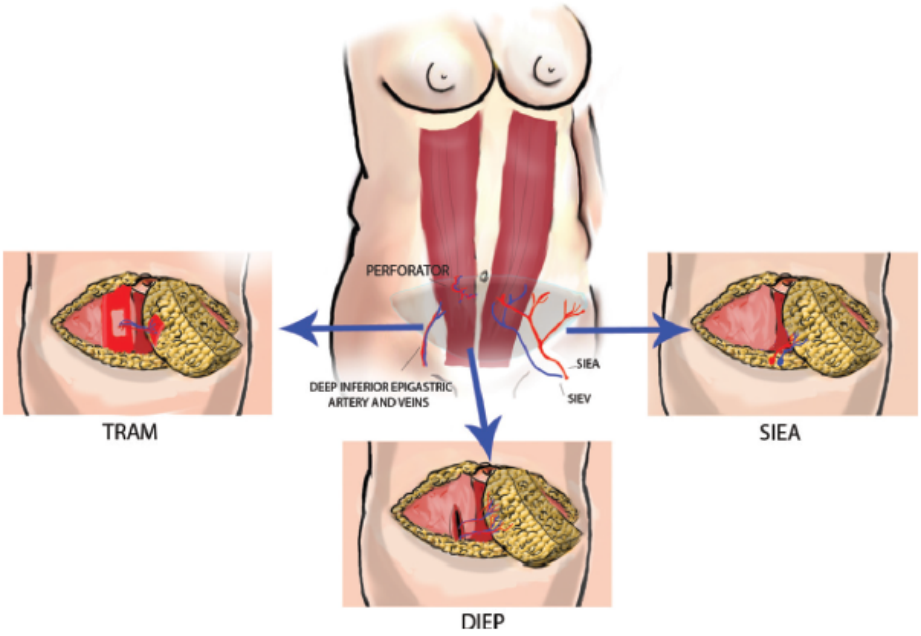

Figure 2.8: Comparison of the blood supply in free TRAM, DIEP and SIEA flaps. Adapted from [11].

2.3 Preoperative Imaging Studies

Since microsurgeries started to be used for tissue reconstruction, a great interest in preoperative imaging started to develop. At that time, the handheld Doppler Ultrasound probe was the most common imaging technique performed [13].

In order to achieve a successful DIEP reconstruction, the flap must be perfused by the right perforator artery. The criteria that influence this are its location, caliber and intramuscular trajectory, as already described in Section 2.2. Flap failures and partial necrosis are believed to be related to the great variability of the perforators anatomy between different people and even from one hemi abdomen to the other [9, 14]. Then, preoperative imaging studies have been made to avoid time-consuming dissections throughout the surgical procedure, allowing to choose the dominant perforator before the surgery. Several noninvasive techniques have been used to preoperatively create a map of the perforators. They include the handheld continuous-wave Doppler ultrasonography (US) [21, 22], color Doppler US [23, 24], and recently, CTA [25, 26] and Magnetic Resonance Angiography (MRA) [13]. These techniques will be briefly described next, according to Pratt *et al.* [13].

2.3.1 Continuous-wave Doppler US

Continuous-wave Doppler US is performed with a handheld ultrasound Doppler probe, which is a relatively inexpensive unit commonly found in most hospitals. It requires an interface layer of ultrasound gel between the skin and the probe to facilitate the transmission. An audible signal is

emitted when the probe is over a blood vessel, and it becomes stronger if the direction of the vessel is pointing to the probe. Some studies have shown that the Doppler probe has reasonable accuracy in identifying perforators for different free-flap operations [21, 22, 27], while others report bad accuracy when comparing with surgical findings, especially when the studied vessels are small and at deeper regions [28]. Besides, some authors report that this technique is less accurate and suffers more from interuser variability than modalities such as CTA [29].

2.3.2 Color Doppler US

Color Doppler US creates a grayscale image by using ultrasound. The pixel intensity is related to the blood flow, being possible to distinguish between slow and fast flow, which is important to separate arteries from veins. Color Doppler US is an operator-dependent procedure with a steep learning curve. It was the standard imaging technique for DIEP flap until very recently, being substituted by the CTA.

Cina *et al*. [9] found Color Doppler US to be reliable for estimating the caliber of the perforator and for giving an accurate mapping of the perforators when performed by experienced personnel. In addition, the authors verified that this technique was able to differentiate between the opacified artery and the unopacified veins, which run close together and have small calibers, something that CTA was not capable of. However, Color Doppler Ultrasound gave less information about the intramuscular course of perforator vessels and possible superficial venous communications. Figure 2.9 shows an example of an image acquired through this technique.

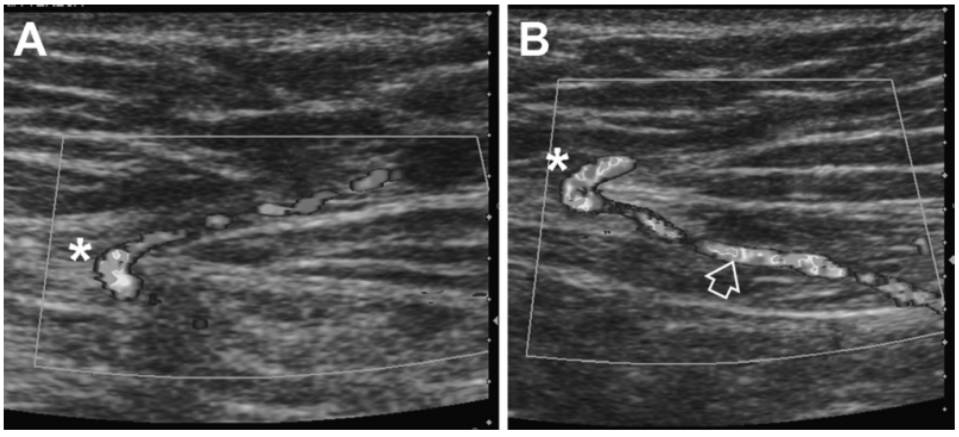

Figure 2.9: Color Doppler Ultrasound of the abdominal wall vasculature. (A) Subcutaneous course of the perforator, superficial to the anterior *rectus* sheath (asterisk). (B) Subfascial and intramuscular course of the perforator (arrow), deep to the anterior *rectus* sheath (asterisk). Adapted from [13].

2.3.3 Computed Tomographic Angiography

CTA involves a combination of computer-analyzed-x-ray images with a bolus of venous contrast medium in order to obtain high-resolution images of blood vessels (Figure 2.10). Technology advances have been allowing faster and more detailed acquisitions and, at the same time, reducing the time of the process. Despite the cost, radiation exposure and iodinated contrast media associated to multidetector CT, the excellent accuracy it has demonstrated led many authors to propose that it should become the standard preoperative imaging technique in DIEP surgery. Advantages include noninvasive nature, more accurate images than Doppler and color Doppler, detailed information on intermuscular course of perforators, information on other vessels present in the area like the SIEA and less interuser variability.

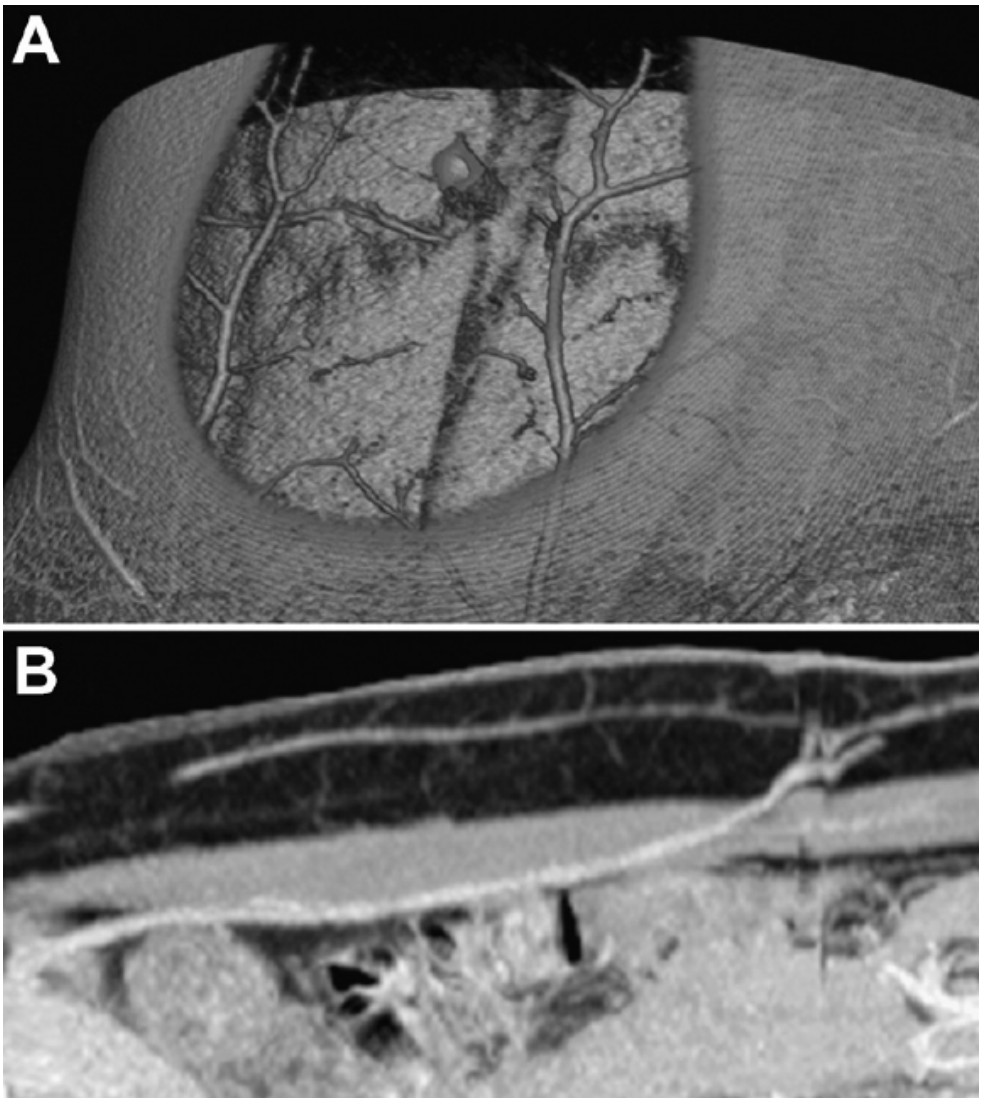

Figure 2.10: CTA of the abdominal wall vasculature. (A) Oblique 3D volume rendered image showing the subcutaneous portion of the DIEA perforators and superficial venous system. (B) sagittal MIP image showing intramuscular course of a perforator. Adapted from [13].

Cina *et al.* [9] concluded that in some cases, CTA cannot distinguish between perforator artery and adjacent veins. Even then, this did not affect the selection of the main perforator. The authors also found that multidetector CT, in comparison to color Doppler US, is better to evaluate the intramuscular course of the perforator and to assess the superficial venous communications, which might be an important indicator of the survival of large flaps.

Rozen *et al.* [30] found trends for shorter operating times, decrease in fat necrosis and shorter lengths of hospital stay among patients undergoing preoperative CTA. Besides, the authors found statistical significance for reduced incidence of partial flap loss, abdominal wall herniation, donor site morbidity and surgeon's stress level.

Smit *et al.* [31] verified that preoperative CTA decreases surgery time and a tendency to less morbidity. Although the cost of a CTA was around 350 pounds, a mean of 1750 pounds per patient was saved due to the reduction of surgery time and its associated costs. Besides, the authors found that CTA helped to determine if a patient was suitable for a DIEP flap, to design the flap and to plan the incision to perform.

Masia *et al.* [14] experienced no false negatives nor false positives in the identification and location of the dominant perforator. Plus, the imaging allowed the authors to discover the existence of the SIEA in 62% of the cases and to perform a SIEA flap in 19% of the cases. They found a decrease of postoperative complications when using multidetector CT before surgery.

Rozen *et al.* [32] stated that CTA was able to accurately identify the size, location, caliber and course of perforators throughout their intramuscular, subfascial and subcutaneous courses. The authors also found that, by limiting the scan range to the flap donor site, the radiation dose was less than 6mSV for a DIEP flap (less than a standard abdominal CT scan).

2.3.4 Magnetic Resonance Angiography

Magnetic Resonance Imaging (MRI) has been recently proposed for preoperative planning, in order to avoid the radiation dose inherent to the CTA. It uses the properties of magnets to align hydrogen nuclei in the tissues such that they resonate. The resulting signal can be processed, leading to the creation of an image (Figure 2.11). The disadvantages related to this technique include its high cost, large scanning time and the fact that it is not suitable for claustrophobic patients and for those who have metallic implants.

Although MRI allows to visualize vessels, supplementing the scan with nonionizing paramagnetic contrast material such as gadolinium, allows to increase even more the contrast of arteries. This technique is commonly known as MRA.

Despite the investigation and evolution of the technique, its lower spatial resolution leads to worse accuracy than CTA, as reported by Rozen *et al.* [33].

2.3.5 Summary

Different imaging techniques have been used to preoperatively study the abdominal wall vasculature. When microsurgery based reconstruction methods started to develop, Continuous-wave US

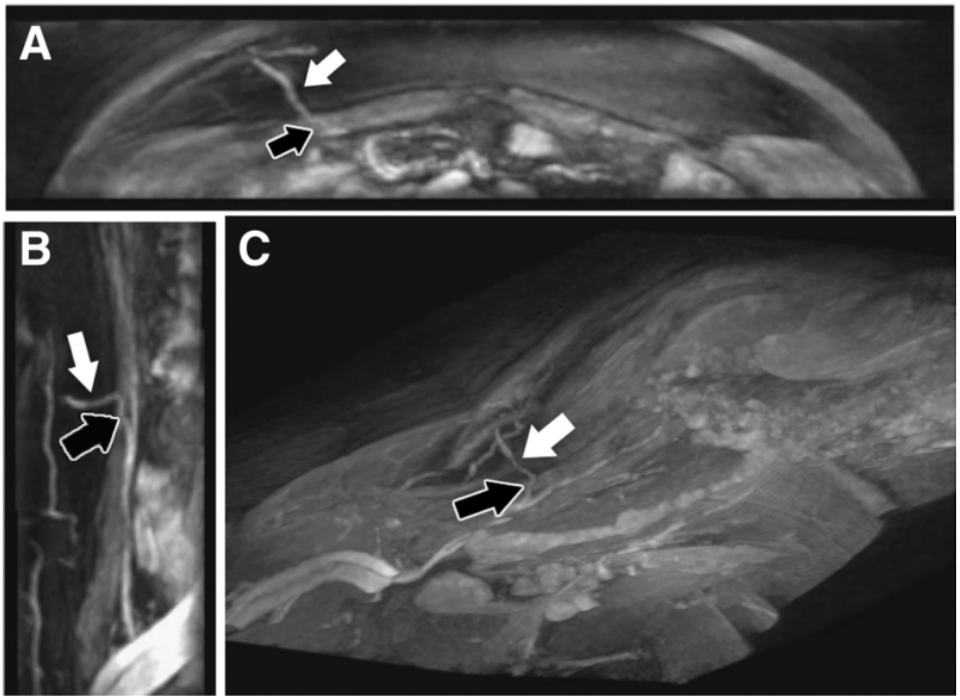

Figure 2.11: MRA of the abdominal wall vasculature. The black and white arrows point to the intramuscular and subcutaneous course of DIEA, respectively. A, B and C are the MIP 3D reconstructions in axial, sagittal and obliquely slices, respectively. Adapted from [13].

was the state-of-art imaging modality for creating the perforators map. Then, more accurate methods started to be proposed in order to improve the accuracy of the studies findings. Color Doppler US retrieves more accurate information but is a highly-user dependent technique. CTA improved even more the extracted information by giving better insight about the intramuscular course of the perforators, which is very relevant for the flap design procedure. The radiation exposure inherent to the CTA scan contributed to a big interest in performing preoperative studies through MRA. Even then, this imaging modality still has lower spatial resolution than CTA, and consequently the latter presents higher accuracy.

Chapter 3

Literature Review

To the best of our knowledge, there is no algorithm in the literature focusing the segmentation of the DIEA perforators. Still, vessel segmentation algorithms usually follow common principles and assumptions that stand true for different types of vessels, *e.g.*, segmenting tubular structures with circular shaped cross section.

Then, a brief description of the main approaches regarding Three-Dimensional (3D) vessel segmentation is made in this Chapter. The methods in the literature are usually a combination of assumptions and vessel extraction techniques, which motivates a specific description for each of these concepts. Following Lesage *et al*. [34], a description of proposed vascular models, image features and extraction schemes is made in this Chapter.

3.1 Vascular models

Vascular models represent the prior knowledge related to the structures of interest. Algorithms can make different assumptions on the target vessels, *e.g.* having circular cross section. These assumptions can be based on appearance and/or geometric properties, leading to three main classes: appearance, geometric and hybrid models.

3.1.1 Appearance models

Appearance models are related to the luminance of vessels and are highly dependent of the imaging modality. Besides, the intensity of vessels also varies according to the specific acquisition protocol, whose specificities can be used to know the theoretical intensity of target vessels [35, 36, 37]. However, achieving steady concentrations of contrast agent is not a trivial task, commonly leading to variable vessel intensities. In this context, the intensities can be modeled by a distribution, like the Gaussian distribution, as proposed by Florin *et al*. in [38].

Some studies model not only the vessels but also their neighborhood. The simplest assumption is to consider vessels brighter than the surroundings in contrasted-enhanced modalities such as CTA and MRA [38]. More complex models based on statistical mixtures were proposed in [39, 40]. These approaches rely on intensity differences between the vessels and the background, an

assumption that is innacurate when other hyper-intense structures surround the vessels. Instead of only considering the intensity, Schaap *et al.* [41] analyzed the homogeneity as well, and modeled vessels as more homogeneous structures than their neighborhood.

3.1.2 Geometric models

Geometric models are related to the shape of target vessels. Several works model directly the vessel surface, for instance, Frangi *et al.* [42, 43] exploited B-spline tensor surfaces and de Bruijne *et al.* [44] used active shape models to model vessel axis and cross section deformation independently, increasing the flexibility of shape generalization (Figure 3.1).

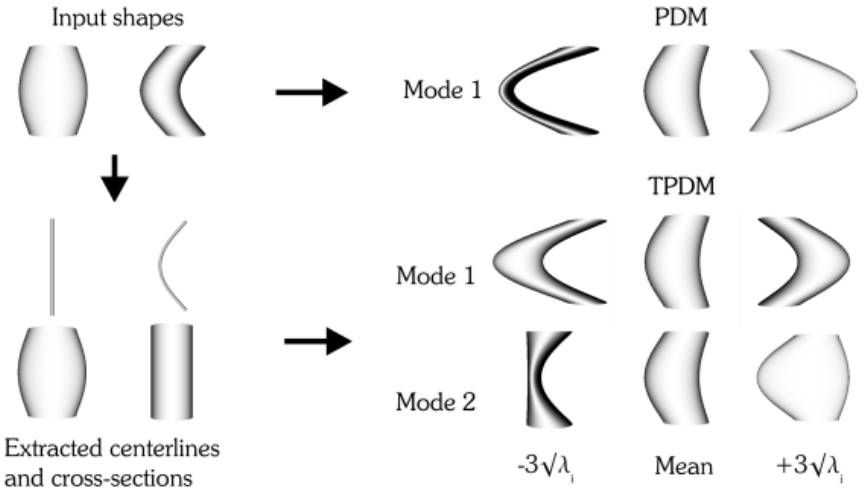

Figure 3.1: Modes of variation found by a single Point distribution model (PDM) and the combined model (TPDM) built from two illustrative input shapes. The latter is able to detect an additional mode of variation. Adapted from [44].

Other authors model the vessel centerline, commonly following the assumption that it presents limited curvature. Frangi *et al.* [42, 43] modeled the centerline as a One-Dimensional (1D) B-spline curve and Lacoste *et al.* [45] proposed an approximation by piece-wise linear curves.

3.1.3 Hybrid models

Hybrid models incorporate both appearance and geometric properties. For instance, Krissian *et al.* [46] used 3D Gaussian line profiles to model the vessel cross section. However, as vessel radius increases, the profile of the cross section starts to be more plateau-like (see the middle row of Figure 3.2). This behavior motivated the use of different models to represent the cross section of these vessels, such as bar-like profiles [47] and the 3D cylindrical intensity model proposed by Wörz and Rohr [48] (Figure 3.2). A different approach to model vessels was exploited by Aylward and Bullitt [49] and Fridman *et al.*[50], where the intensity of images is considered an additional dimension and vessels become local ridges of the image hyper-surface.

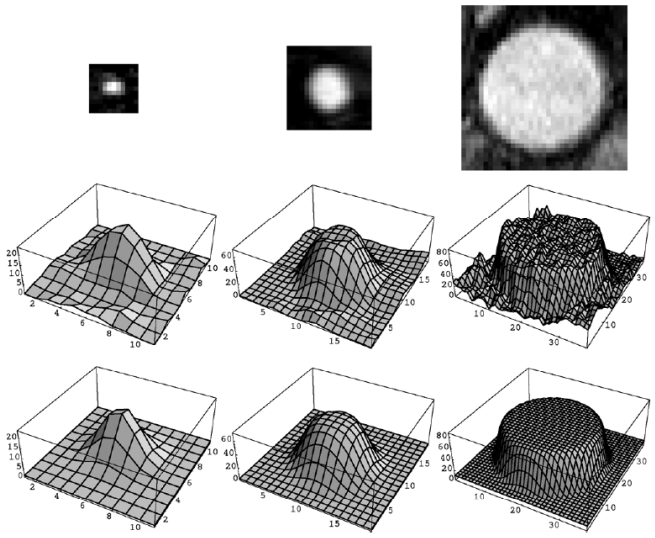

Figure 3.2: (Top row) Orthogonal 2D slices through vessels with different radius; (Middle row) Corresponding intensity plots; (Bottom row) Intensity plots of the cylindrical intensity model. Adapted from [48].

3.2 Image Features

Image features, *e.g.*, local intensity curvature, allow to evaluate the vessel likelihood of a certain voxel. This section describes some of the image-based features that have been proposed in the literature.

3.2.1 Local isotropic features

Local isotropic features measure vessel likelihood without exploring their directionality. Aylward *et al*. [51] implemented a multiscale ridge detector through multiscale Laplacians of Gaussians, assuming that vascular intensities were locally maximum. This approach was extended in other works where vessel direction was also considered [49, 52]. Vasilevskiy and Siddiqi [53] measured the gradient flux through the boundaries of multiscale spheres to detect vessels. The authors stated that it was possible to detect low contrast and narrow vessels.

3.2.2 3D local geometry features

3D local geometry features explore the hyper-intensity and tubular shape intrinsic to vessels. Several approaches use the second-order derivatives to characterize the local geometry. 3D vessels can be distinguished by a small-curvature along the vessel direction and a normal high-curvature plane (Figure 3.3). Multiscale approaches using Hessian-based filters were proposed in [54, 55]. Figure 3.4 shows an example result obtained with the framework proposed by Frangi *et al*. [54].

Deviations from a single vessel, such as bifurcations and aneurysms, commonly produce false negative responses to these filters. Besides, non-vessel hyper-intense structures might perturb vessel detection.

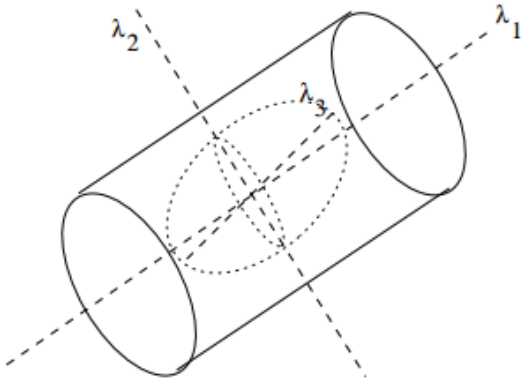

Figure 3.3: Second order ellipsoid describing the local principal directions of curvature. Adapted from [54].

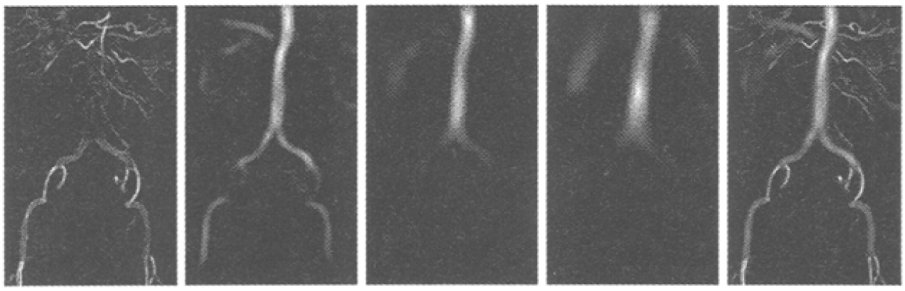

Figure 3.4: Vessel enhancement obtained at increasing scales (first four images) and the final result obtained after the scale selection. Adapted from [54].

Agam *et al.* [56] developed a different approach, considering the spatial covariance of image gradient vectors. This alternative allows to detect more than one principal direction making it capable of discriminating between single vessels, bifurcations and nodules (Figure 3.5). The authors reported smaller mean square localization errors and better behavior at bifurcations when comparing to the Hessian-based approach of Frangi *et al.* [54, 55].

Integrative features were also proposed, in order to increase the robustness to noise [47, 52]. However, filters do not enjoy from a well-defined scale-space theoretical framework. Usually, these algorithms are restricted to a single scale, although Hernandez-Hoyos *et al.* [57] proposed heuristics to adapt the scale value.

Fitting a vessel model into the image is another popular approach to measure vessel likelihood. Friman *et al.* [58] used Gaussian profiles to model the Two-Dimensional (2D) cross section of vessels. Worz and Rohr [48] considered a 3D cylindrical parametric intensity model instead. The

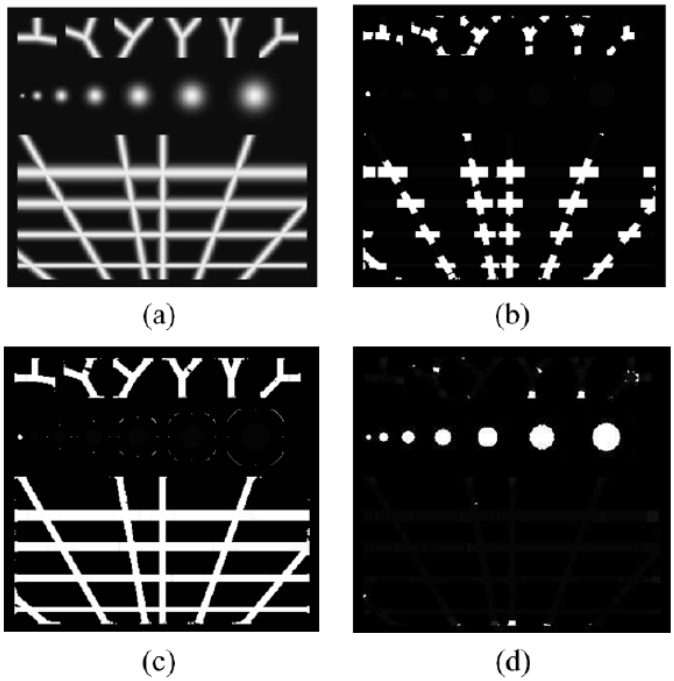

Figure 3.5: Specific structure enhancement by applying different filters. a) synthetic original image; b) enhanced junctions; c) enhanced junctions and vessels; d) enhanced nodules. Adapted from [56].

reasoning comes from the fact that 2D cross sections of medium and large vessels is plateau-like, as already mentioned.

3.2.3 2D cross section features

2D cross section features are commonly used in frameworks where vessel direction is estimated and serves as input. Behrens *et al.* [59] used a randomized 2D ellipse Hough Transform to detect 2D cross sections on edge maps. The approach is computationally efficient but is dependent on the edge detector which is usually very prone to noise and not suitable for low-contrast regions. Florin *et al.* [38] compared the intensity inside a 2D ellipse with its surroundings. The local maxima contrast feature is reached when the ellipse is aligned with the vessel cross section.

Ray-casting features were used for the characterization of 2D vessel cross sections [37, 60, 61]. Considering a point inside the vessel and its cross section, this technique aims at detecting the vessel wall by emitting rays from that point in an equi-angularly manner. Analysis of each ray was performed in several ways, for instance, Wesarg and Firle [37] used intensity thresholding while Wink *et al.* [61] used gradient thresholding (Figure 3.6).

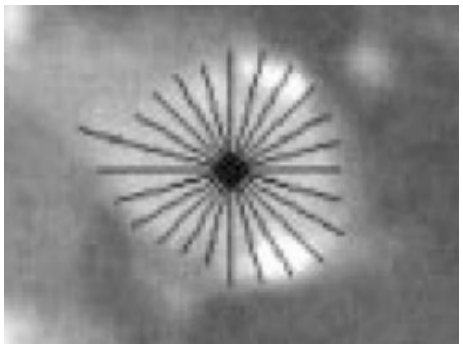

Figure 3.6: Vessel wall detection through gradient based ray-casting features. Gradient maximum is selected for each ray. Adapted from [61].

3.3 Extraction schemes

Extraction schemes use the considered vascular models and image features to perform the final vessel segmentation. This section covers different techniques that have been proposed for this task.

3.3.1 Region growing approaches

Region growing approaches segment a vessel from a starting point/region inside it, called seed point/region. Then, these methods iteratively join neighboring pixels to the seed, based on a specific criteria (Figure 3.7). The simplicity of these methods makes them computationally efficient, although they are dependent on the initial seed point location, which might be an important factor in many frameworks. To overcome the initialization problem, Wan *et al.* [62] proposed a symmetric region growing algorithm capable of extracting the same vessel tree for different starting seed points.

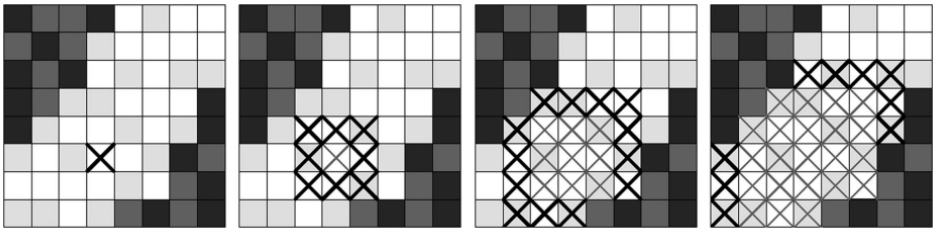

Figure 3.7: Segmentation using a region growing algorithm. From the left to the right, the algorithm starts with a seed point and iteratively adds neighbor voxels that satisfy a certain inclusion criteria. Adapted from [35].

Boskamp *et al.* [35] proposed a simple intensity-based region-growing, however, the approach becomes innacurate in noisy and heterogeneities-rich vessel segments. Metz *et al.* [63] proposed

a growth-limiting criteria to avoid leakage problems. Other authors focused on wave propagation techniques, as they assure spatially coherent propagation [64, 65]. Several wave speed functions have been proposed, such as, Uniform Euclidean speed and binary inclusion criterion [66], weighted geodesic speed [36] and dynamically adapted speed [39]. The connectivity of the propagating interface was exploited to detect bifurcations [36, 63, 66].

3.3.2 Active contour methods

Active contours evolve an interface based on internal and external forces. The former are related to the contour geometry and constraints while the latter are derived from the image.

Parametric active contours rely on explicit Lagrangian formulation of a contour evolution. Delingette and Montagnat [67] reviewed these techniques. Topology-adaptive snakes were introduced by McInerney and Terzopoulos [68] and allow to control the splitting and merging of contours. The authors claimed that these properties combined with a re-parameterization scheme allow to capture thin vessels and bifurcations (Figure 3.8). Eigen-snakes, presented by Toledo *et al.* [69], compute the principal component of the distribution of gradient vectors, in order to exploit vessel direction in the energetic formulation. Yim *et al.* [70] considered a deformable tubular surface and optimized it with respect to the centerline of the vessel. Frangi *et al.* [42] optimized the B-spline tensor surface using explicit control points.

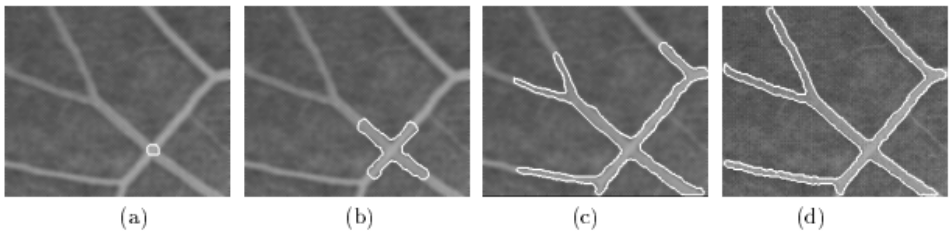

Figure 3.8: Segmentation based on topology-adaptive snakes. (a) to (d) shows the evolution of the snake. Adapted from [68].

Implicit active contours make use of level-set techniques, where the contour is the zero level of a higher dimension function. These methods avoid parameterization problems but also have higher computational costs. A detailed presentation of this topic is present in [71].

3.3.3 Centerline based approaches

The algorithms presented in the last sections focus on extracting the vessel surface. Centerline-based approaches aim at directly extracting the vessel centerline instead. Nevertheless, many frameworks apply methods to segment vessel lumen from its centerline.

Centerline-based methods usually require initialization by the user. Then, centerline points are commonly predicted through vessel direction estimation, which may be based on different image features described in section 5.2. To increase the robustness of these systems, past centerline

points can influence the current prediction, as considered in [43, 72]. A common approach is to use a Kalman filter for such task, as considered in Worz and Rohr [48].

Several frameworks correct the centerline position after analyzing local image features. Wesarg and Firle [37] considered the center mass of cross-sectional contour points detected along 1D rays as the new centerline position, while Friman *et al.* [58] used local optimization of 3D models instead.

Automatic bifurcation handling requires the segmentation of vessel lumen and the use of topological criteria. Aylward and Bullitt [49] and Fridman *et al.* [50] used ridge-based features to perform online branching detection.

Centerline-based methods become better defined when both start and end points are given. In this context, Frangi *et al.* [42, 43] started by optimizing the centerline of the vessel considering fixed boundary conditions. Minimum cost path techniques find the centerline path which minimizes a cost function. Lower costs are associated to voxels that are more likely to belong to the vessel centerline, based on extracted image features. These techniques differ according to the method they use for optimization. Wink *et al.* [73] implemented graph-based schemes, while Young *et al.* [74] used fast-marching schemes which are more accurate but have higher computational costs. The cumulative nature of the path cost leads to the common problem of shortcut paths being selected as the ideal solution. Li and Yezzi [75] represented the vessel as a Four-Dimensional (4D) curve, where each point represents a 3D sphere and the radius (Figure 3.9). The efficiency and capability of reaching global minima of minimal path techniques is combined with the ability of active surface techniques to represent a full 3D surface.

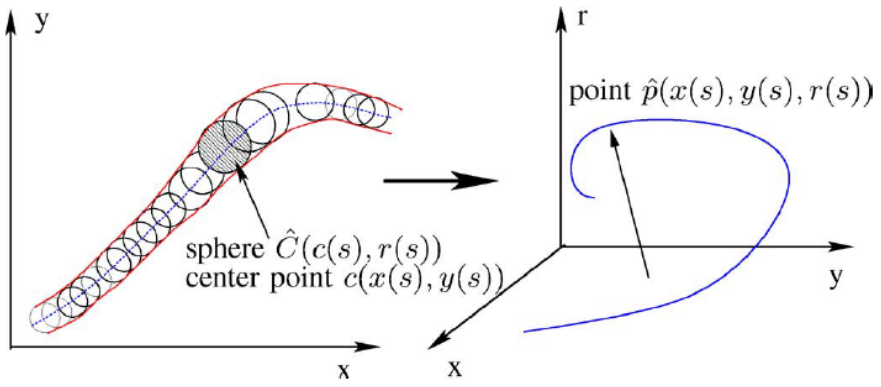

Figure 3.9: Representation of a tubular surface as the envelope of a family of spheres with changing center points and radius. Adapted from [75].

Some authors proposed termination criteria in order to remove the need of knowing the end points. Gulsun and Tek [60] used heuristic thresholds on image features and Wink *et al.* [73] propagated the waves of minimum cumulative costs, based on the response to an eigenvalue filter (Figure 3.10).

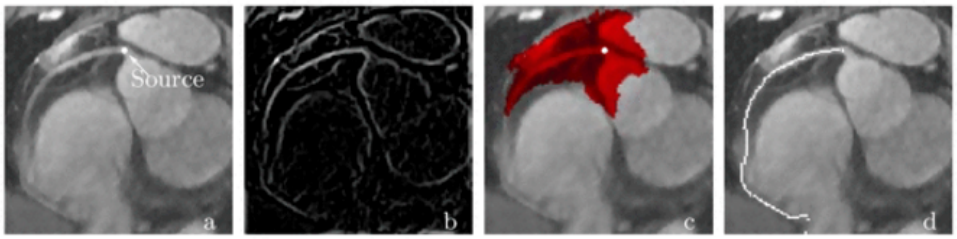

Figure 3.10: Vessel segmentation by propagation of waves of minimum cumulative costs. From left to right: (a) source point, (b) eigenvalue filter response, (c) wave of cumulative costs at a certain instant and (d) extracted vessel. Adapted from [73].

Yim *et al*. [76] addressed the characterization of small vessels in MRA. Vessel axis were determined through the ordered region growing (ORG) algorithm. Like common region growing approaches, this method starts from a user defined seed point/region. However, at each iteration, the voxel that is propagated is the one that belongs to the boundary of the current seed region and has the highest intensity value. This produces an acyclic graph as the one present in Figure 3.11. When the endpoints of the vessel tree are given, vessel segments can be obtained by tracing the path from each endpoint to the origin. Another option, is to remove all branches whose length is smaller than a specified length.

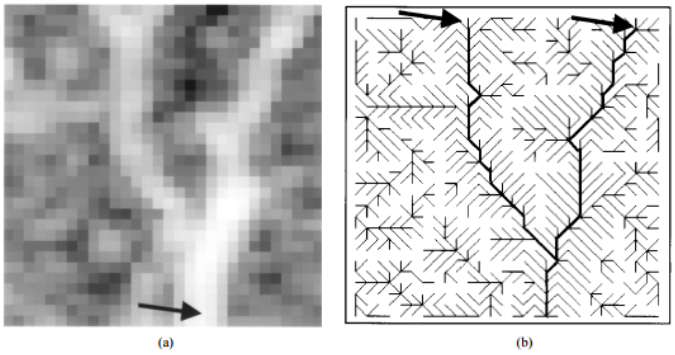

Figure 3.11: Vessel centerline extraction using ORG algorithm. (a) 2D image of a vessel where the arrow indicates the seed point. (b) Obtained ORG graph. Adapted from [76].

3.4 Summary

This chapter contains a brief description of some of the most representative works related to 3D vessel segmentation. The high number of methods proposed to solve this task shows that it is a crucial step for many medical image applications, such as facilitating visualization, measuring vessel features, surgery planning, between others.

Besides the high number of proposals, their nature is also highly variable. Even a single proposal is usually composed by a sequence of assumptions and techniques leading to the final segmentation. The design of a vessel segmentation algorithm is then dependent on the assumptions one can make according to the target structures and imaging modality. After choosing an appropriate vascular model, image-based features and extraction scheme should be selected keeping in mind the final requirements, for instance, computational cost, required user input and robustness to noise.

Image-based features using derivative operators are sensitive to noise and should be avoided when the target structures have low Signal-to-noise ratio (SNR). Integrative operators are more robust to noise but do not allow to easily apply multiscale approaches. Local model fitting is highly dependent of expressing an accurate model of the target vessel in a closed form.

Region-growing schemes are highly efficient but are very prone to leakage problems on heterogeneous environments. Parametric active contours are computationally efficient but their implementation becomes complex at 3D situations. Implicit active contours are not affected by parameterization problems but their computational cost is higher and convergence must be ensured. Centerline-based methods seek higher robustness to noise and artifacts but require the estimation of more parameters in each iteration. Besides, these methods do not provide directly a vessel lumen segmentation.

Chapter 4

Database and Region of Interest

This chapter describes the database provided by the Breast Cancer Unit of *Fundação Champalimaud*. Besides showing examples of the images contained in the database, the region of interest for our research purposes and the anatomical structures which exist there will be also focused. In the end, a characterization of the available *Ground Truth* annotations and how they were obtained is made.

4.1 CTA volumes

Fundação Champalimaud provided CTA volumes from 20 different patients. They are in Digital Imaging and Communications in Medicine (DICOM) format and contain several axial slices, which are perpendicular to the long axis of the body (see Figure 4.1).

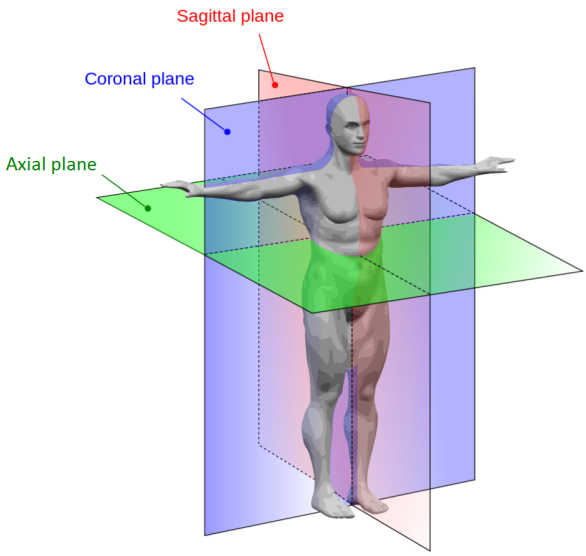

Figure 4.1: Anatomical planes of the body. Adapted from http://www.interactive-biology.com/.

The volumes differ in terms of number of axial slices and resolution. As represented in Figure 4.2, the spacing between consecutive slices is usually larger than the spacing between consecutive pixels of a slice. Figure 4.3 shows a sequence of slices (not adjacent) which demonstrates the type of images available in the database.

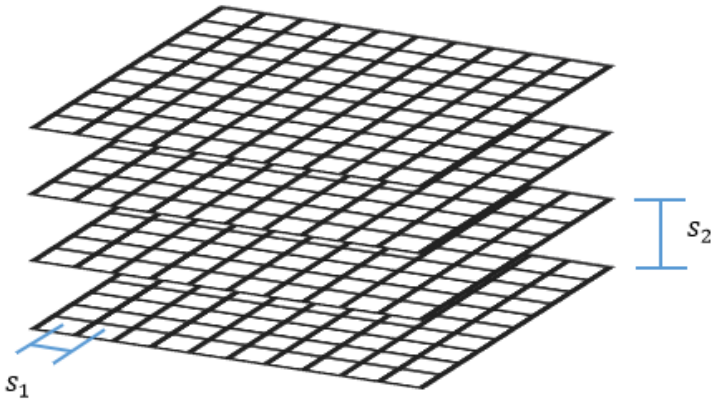

Figure 4.2: Representation of a pile of axial slices where s_1 is the spacing between adjacent pixels of a slice and s_2 is the spacing between consecutive slices.

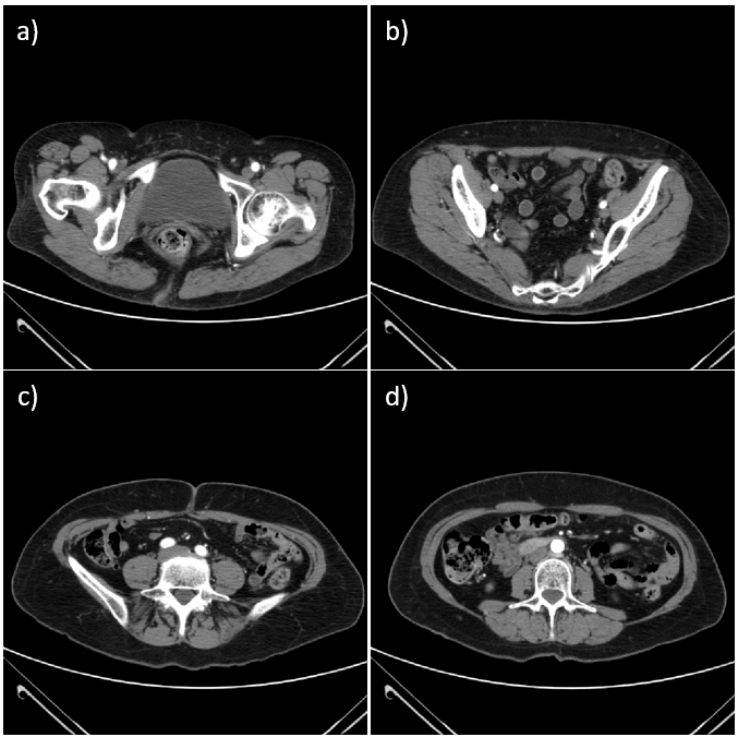

Figure 4.3: Sequence of slices (not adjacent) from the pelvic region (a) to above the umbilicus area (d).

4.2 Volume of interest

Although information from the entire abdominal region of the patients is available, this thesis focuses on the anterior abdominal wall region, since it is there that perforators arise. Figure 4.4 shows some examples of the region of interest along with labels of the existing structures. Usually, in terms of height, our volume of interest starts at the region where the DIEA's enter the posterior lamella of the *rectus abdominis* muscle sheath (see image b) of Figure 4.4) and ends a little above the umbilicus area (see image f) of Figure 4.4), since it is not expected to find DIEA perforators above this section.

4.3 *Ground truth* annotations

As the goal of this thesis is to develop a CAD algorithm which is able to extract the course and caliber of perforators, and the location where they leave the anterior *fascia* as well, *Ground Truth* annotations are required to posteriorly evaluate the performance of the developed approach.

For what concerns the perforator course (both subcutaneous and intramuscular), landmarks along its skeleton are enough to identify the correct path. In order to obtain these inputs from the radiologist, free software programs which allow to segment DICOM images were reviewed. Ease of use and the ability to export the required information were the characteristics considered to make the final choice. Fiji [77] , Mango [78], Seg3D [79] and MIPAV [80] were analyzed. Among these, Fiji was considered the most straightforward, so it was the final choice. In order to guide the radiologist along the segmentation process, a protocol was created (see Appendix A). Figure 4.5 contains examples of the annotations provided by the radiologist using the Fiji tool. Notice that the umbilicus position is the reference for retrieving the position where the perforators leave the *fascia*, hence that information is also required.

Regarding the caliber of perforators, *Fundação Champalimaud* provided a medical report of each patient, where a description of the found perforators is made. The caliber at the region where the perforator leaves the *fascia* is included.

4.4 Summary

Fundação Champalimaud provided CTA volumes from 20 different patients for our research purposes. These volumes are in DICOM format and contain information from the entire abdominal region. This thesis focuses on detecting the DIEA perforators which exist in the anterior abdominal wall, such that the volume of interest was described. Besides, examples of how the relevant structures appear in this volume were shown.

Perforator *Ground Truth* annotations were performed by a radiologist using the Fiji software and a Protocol we have created. The caliber of the perforators and the location where they leave the *fascia* relatively to the umbilicus position are available in medical reports of *Fundação Champalimaud*.

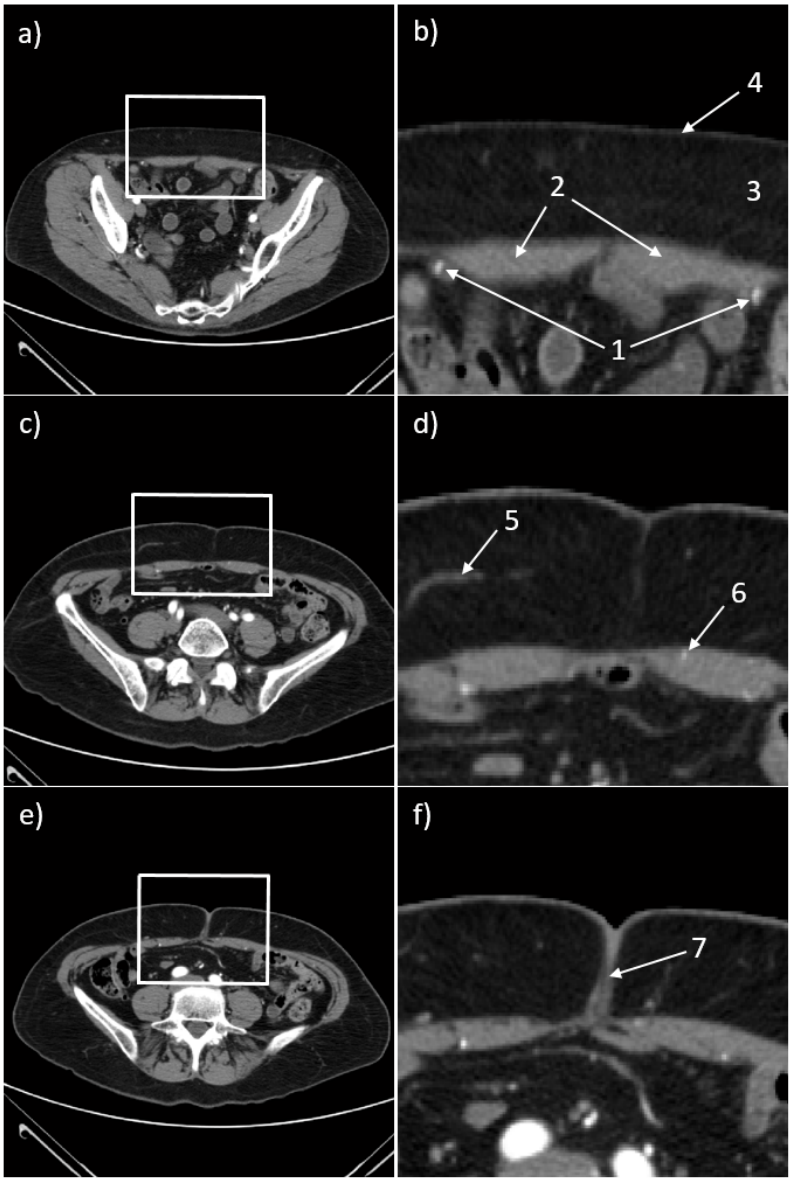

Figure 4.4: a,c,e) sequence of slices (not adjacent) showing our region of interest inside the white boxes; b,d,f) corresponding regions of interest where important structures or areas are labelled: 1 - right and left DIEA, 2 - *rectus abdominis* muscle, 3 - subcutaneous region, 4 - skin tissue, 5 - subcutaneous portion of a perforator, 6 - intramuscular portion of a perforator, 7 - umbilicus scar tissue.

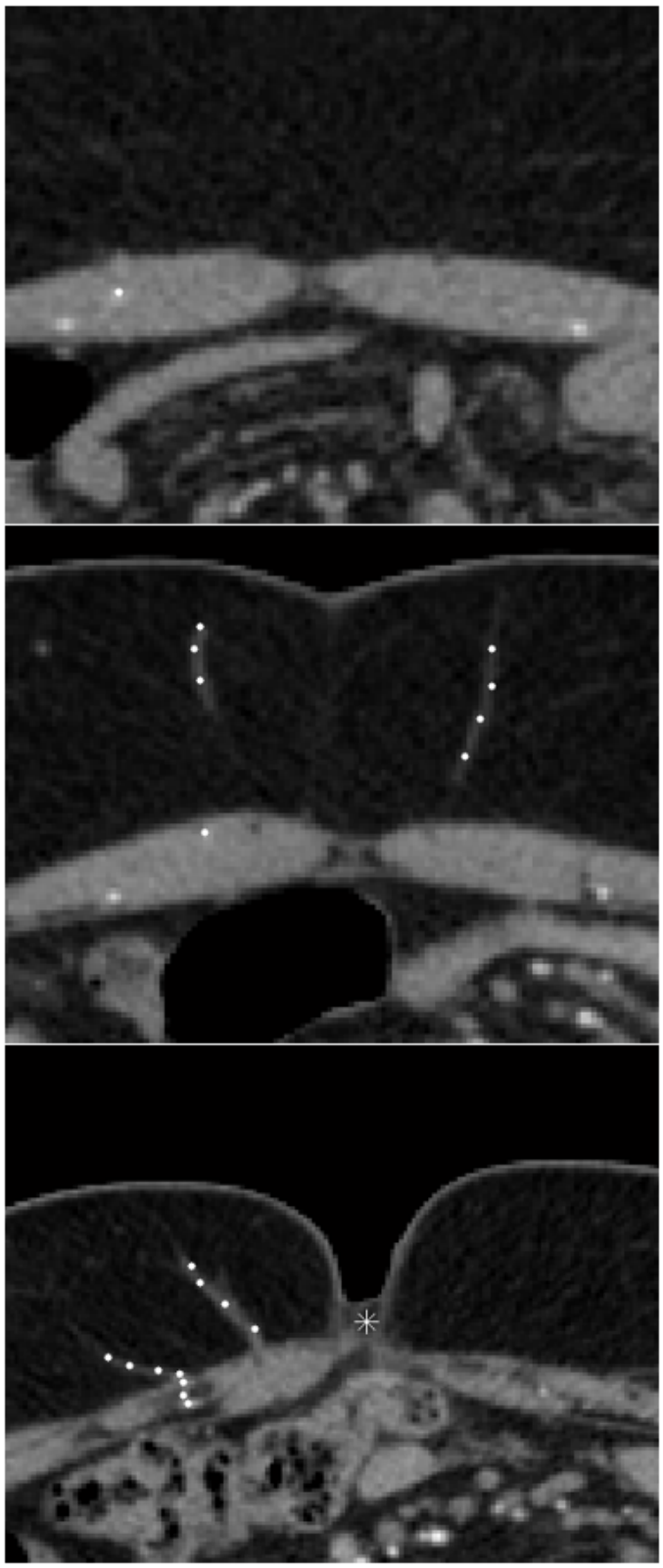

Figure 4.5: Slices with example perforator annotations shown as white circles and umbilicus position marked with a white asterisk.

Chapter 5

Computer Aided Detection of Abdominal Perforators

This Chapter describes the methodology employed to detect the DIEA perforators. By detection, one should consider the extraction of both subcutaneous and intramuscular course of the perforators, as well as the location where they enter the anterior *fascia* and the caliber at that region, since this is the information required for surgery planning. The flowchart present in Figure 5.1 contains a high-level description of the proposed framework. The first part is user dependent and requires the manual selection of the end of the subcutaneous region of perforators and the DIEA sources. These landmarks are used to define the volume of interest (see Chapter 4) and will also be requested along the algorithm execution. The characterization of the blocks of the second part is made along the different sections of this Chapter. Section 5.1 covers the segmentation of the *fascia*, the layer which is the interface between the subcutaneous region and the muscle. This layer is used to divide the detection problem in two. Section 5.2 presents a tracking procedure which is started at the end of the subcutaneous region of a perforator and stops when it reaches the *fascia*. Finally, Section 5.3 proposes the use of a minimum cost path approach to detect the intramuscular course of a perforator.

5.1 Segmentation of the Anterior Abdominal Wall Fascia

The anterior abdominal wall *fascia* separates the muscle from the subcutaneous region. The segmentation of this layer is useful due to two reasons: first, the framework should detect the location where a perforator leaves the *fascia*; second, it allows to use a sequential algorithm to extract the subcutaneous and intramuscular portions of a perforator. Since the characteristics of both regions differ significantly, this allows to apply a different method for each of them.

In terms of image intensities, the *fascia* cannot be distinguished from the *rectus abdominis* muscle. Hence, it is considered to be the boundary between this muscle and the subcutaneous region. This section focuses on the description of the method developed to segment the anterior abdominal wall *fascia*.

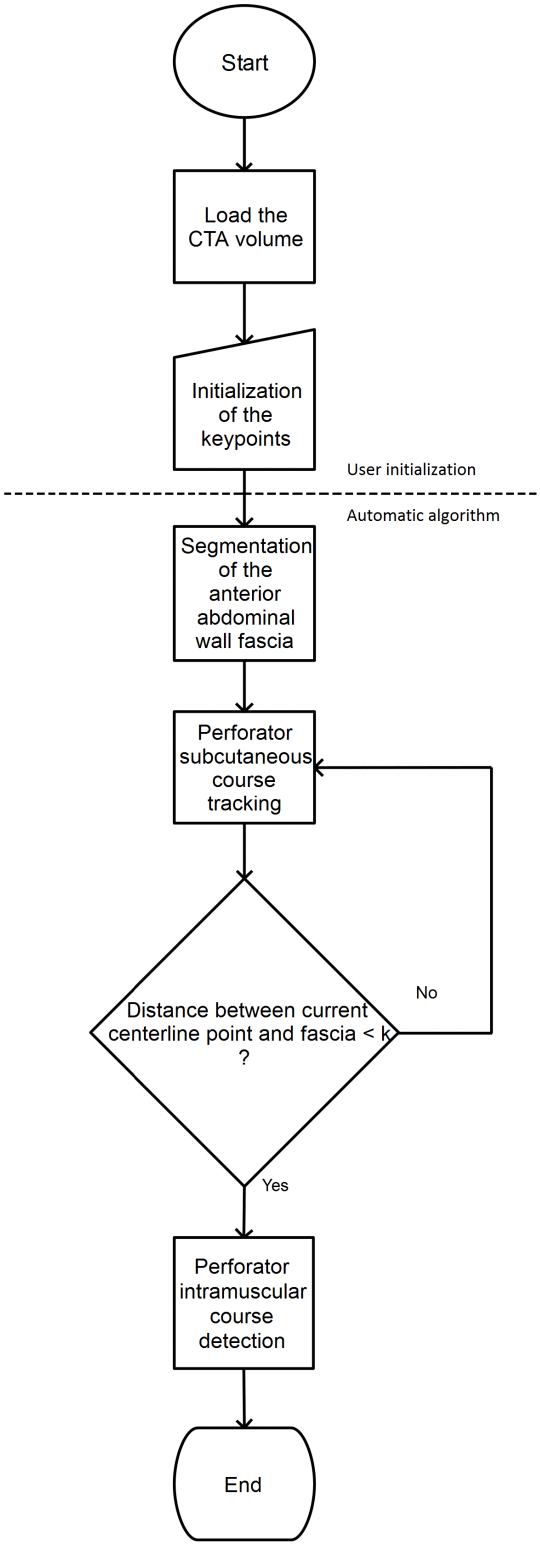

Figure 5.1: Flowchart of the proposed framework. The first part is performed by the user and the second is automatic.

5.1.1 Manual annotations of the Fascia

For each CTA volume comprising the database, the volume of interest is obtained by keeping the volume which contains the manual initialization landmarks plus a margin to deal with the tortuosity of vessels. These landmarks, as already stated, include the end of the subcutaneous portion of the perforators and the locations where the DIEA enters the posterior lamella of the *rectus* sheath (see Figure 5.2).

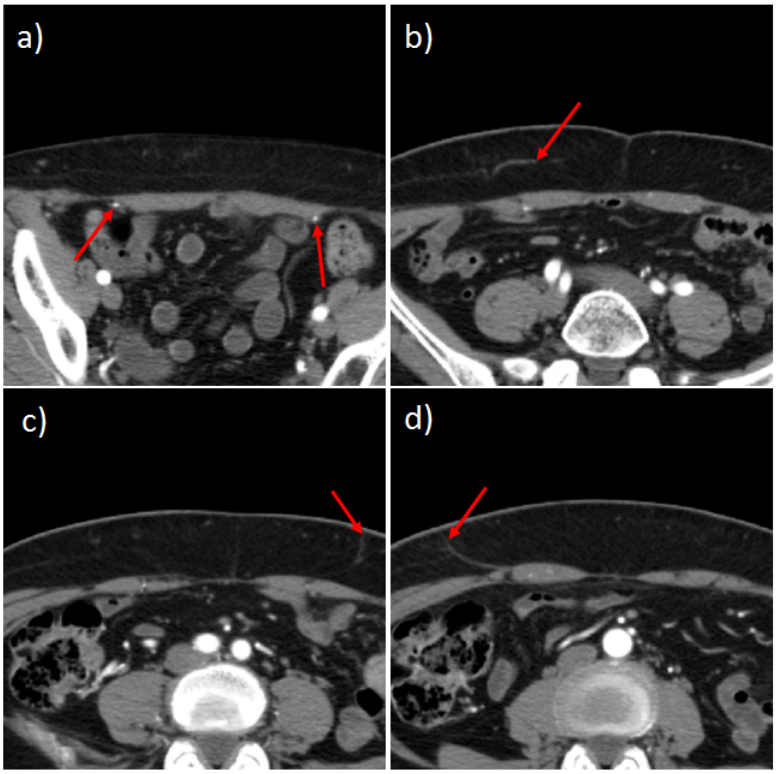

Figure 5.2: Axial slices of the volume of interest. a) Slice at a lower region of the volume, where red arrows indicate the DIEA sources; b-d) slices located above the first one, where red arrows localize the end of the subcutaneous region of example perforators.

Then, for each axial slice of those volumes of interest, a manual annotation of the anterior *fascia* was made, in order to posteriorly evaluate the performance of the developed algorithm. Several points along the *fascia* were collected and a linear interpolation was used to obtain the complete annotation for each axial slice. Some examples of these annotations are present in Figure 5.3.

5.1.2 Proposed methodology

A careful analysis of Figure 5.3 allows to conclude that the region of interest is a transition from pixels with low intensity (subcutaneous region) to pixels with higher intensity (muscle), which

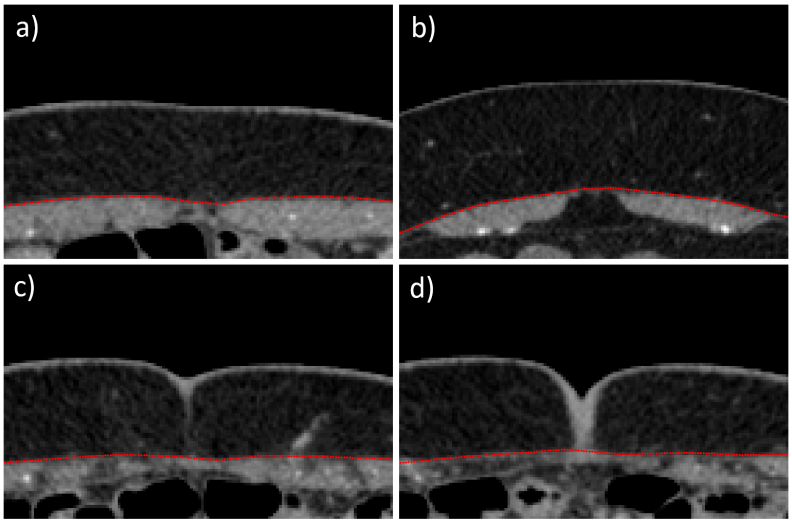

Figure 5.3: Example axial slices with annotations of the anterior fascia in red.

spawns over all the columns of the image. Thus, the Otsu's method [81] was apllied to the axial slices, with the goal of distinguishing the muscle from the subcutaneous region. Figure 5.4 contains the results obtained for the images used as example in Figure 5.3.

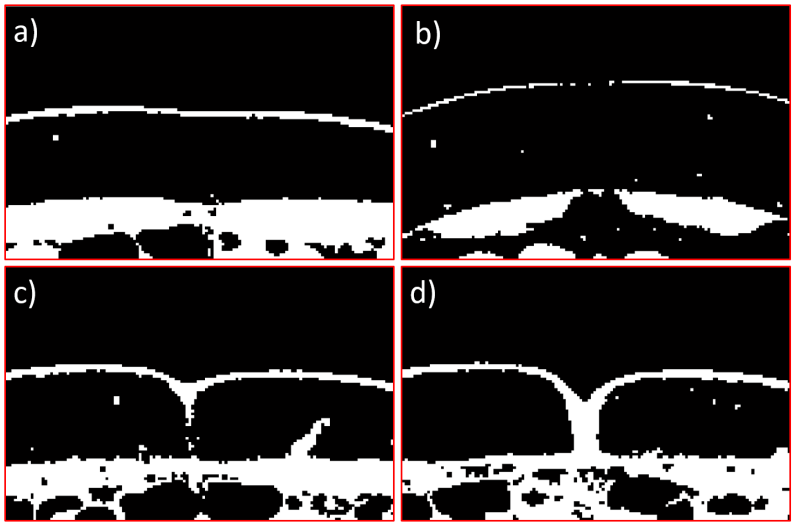

Figure 5.4: Segmentations obtained using the threshold given by Otsu's method [81] in the images of Figure 5.3.

The threshold given by Otsu's method proved to be efficient at separating the muscle from the subcutaneous region. However, as vessels, skin and other structures also have bright intensities, the muscle object might include regions which should be avoided. Two main problems arise at this moment:

- In slices where vessels are leaving the muscle, the segmentation will naturally join both in a single object (see image c) of Figure 5.4);
- Usually, at the level of the umbilicus, the muscle does not appear as a connected region, instead it is connected to the more bright intensity skin tissue (see image d) of Figure 5.4);

The first point is actually more crucial because it interferes directly with the purpose of this algorithm, which is to know the location at which the perforator leaves the *fascia*. Then, it is necessary to neglect the presence of vessels and detect the smooth *fascia* layer. The second point does not have such a direct interference because the perforators do not leave the *fascia* at that region. Nonetheless, it puts at risk the assumption that the *fascia* spawns over all columns, and the connection with the skin object also poses a dilemma.

To solve these problems, a two-phase algorithm is proposed. The first phase consists in a series of post-processing steps which assures that skin and muscle objects are not connected, and results in a raw *fascia* segmentation. The second phase involves local linear regression in the sagittal anatomical plane as a way to avoid the influence of vessels and reach a smoother and complete version of the *fascia* segmentation. This method relies in the fact that, in sagittal slices, the boundary between the muscle and the subcutaneous region is usually very smooth.

5.1.2.1 First phase: post-processing

The first phase of the proposed algorithm is composed by the following steps:

1. Creation of a mask of the region outside the patient body, by keeping the biggest connected component with intensities equal to zero of the original image. Its dilated version is used to remove the skin object present in the Otsu's segmentation image (see Figure 5.5);

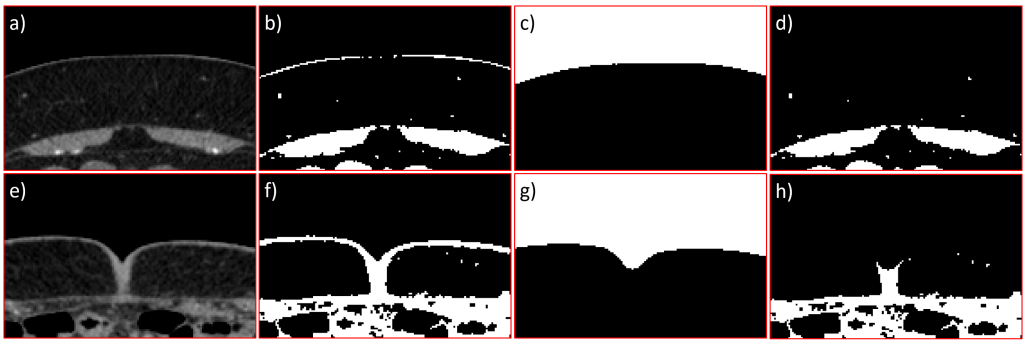

Figure 5.5: Illustration of the steps performed in stage 1, using images b,d) of Figure 5.3 as example. a,e) initial images; b,f) segmentation using Otsu's threshold; c,g) dilated mask of the region outside the patient body; d,h) segmentations after removing the skin object.

2. If the biggest connected component of the resulting image does not spawn over all the columns, the threshold level given by Otsu's method is decreased until that occurs (see Figure 5.6). Notice that the skin response must be removed every time the process is repeated, since it could lead to the test being skipped;

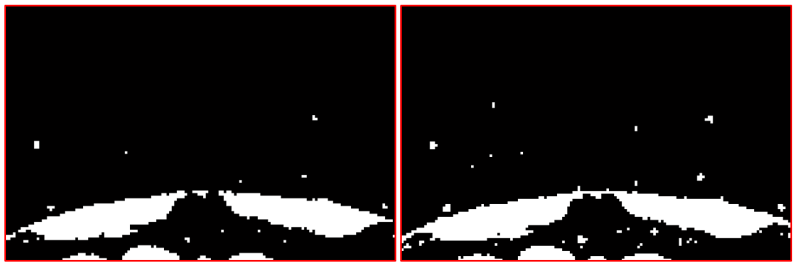

Figure 5.6: Illustration of the step performed in stage 2, using image b) of Figure 5.3 as example. (left) Segmentation after stage 1; (right) stage 2 result, where the threshold was decreased until the biggest connected component spawned over all columns.

3. Regions that lie below the biggest connected component are filled (see figure 5.7);

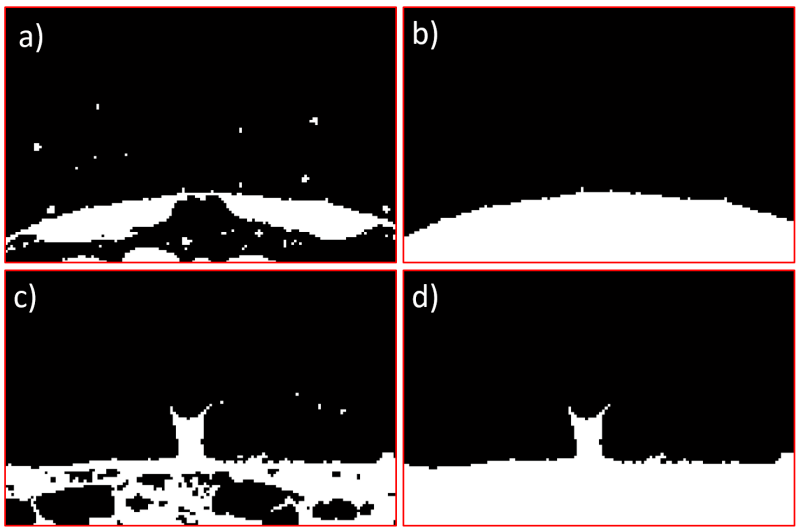

Figure 5.7: Illustration of the step performed in stage 3, using images b,d) of Figure 5.3 as example. a,c) segmentations after stage 2; b,d) segmentation results after filling the regions below the biggest connected and rejecting other objects.

4. If the skin object was connected to the muscle one (this is true when the biggest connected component after the OR operation between the skin object and the result after stage 3 has larger area than before - see Figure 5.8), the horizontal derivatives are obtained through the Sobel operator, which produces high responses at the bridge linking those objects. From those detections, a rectangular mask is created and used to remove the connection between the skin and the muscle (see Figure 5.9);

5. A simple horizontal kernel of size 3 is used to perform an opening of the image, in order to smooth the upper region of the muscle; The size of the kernel is small since the goal is to remove the little noise presence without disturbing the overall shape of the *fascia* layer.

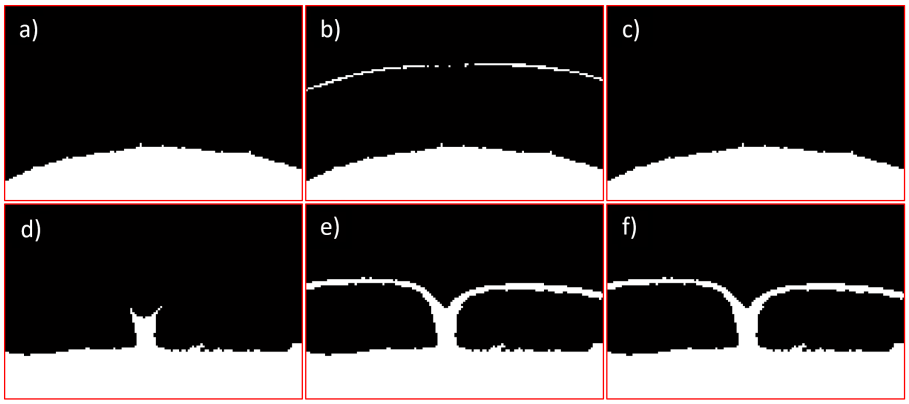

Figure 5.8: Illustration of the test performed to check if the skin and muscle objects were initially connected, using images b,d) of Figure 5.3 as example. a,d) segmentations after stage 3; b,e) OR between those segmentations and the skin object; c,f) biggest connected component after the OR operation.

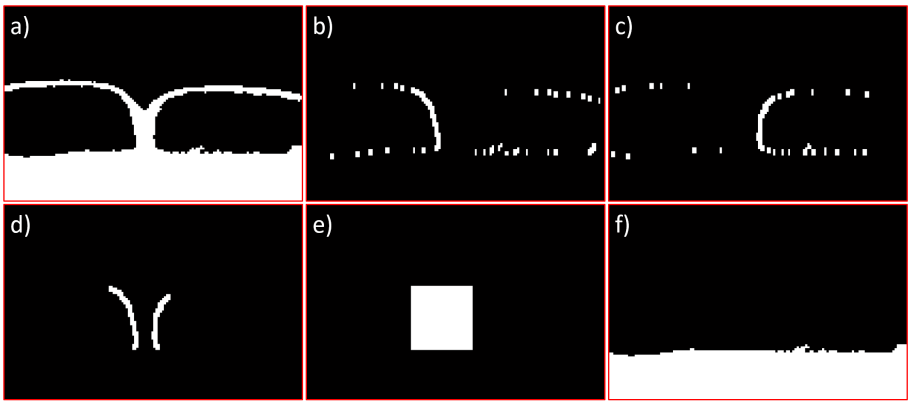

Figure 5.9: Illustration of the steps performed in stage 4, using image d) of Figure 5.3 as example. a) OR between the processed image at the end of stage 3 and the skin object; b,c) Sobel derivative responses; d) OR between biggest connected components of b) and c); e) rectangular mask containing the objects in d); f) segmentation result after removing object e) and the skin object.

6. A border detection is obtained for each column. In the end, only contours which are larger than 11 pixels, considering 8-neighborhood, are retained (see Figure 5.10). This allows to remove some detections in more vertical oriented objects, such as vessels. The value was empirically determined, although using other similar ones would not bring a significant change. Notice that the raw segmentation does not enforce that, in the end, a border detection exists for every column. However, as already stated, the second phase method will estimate the missing *fascia* detections, besides smoothing the existing ones.

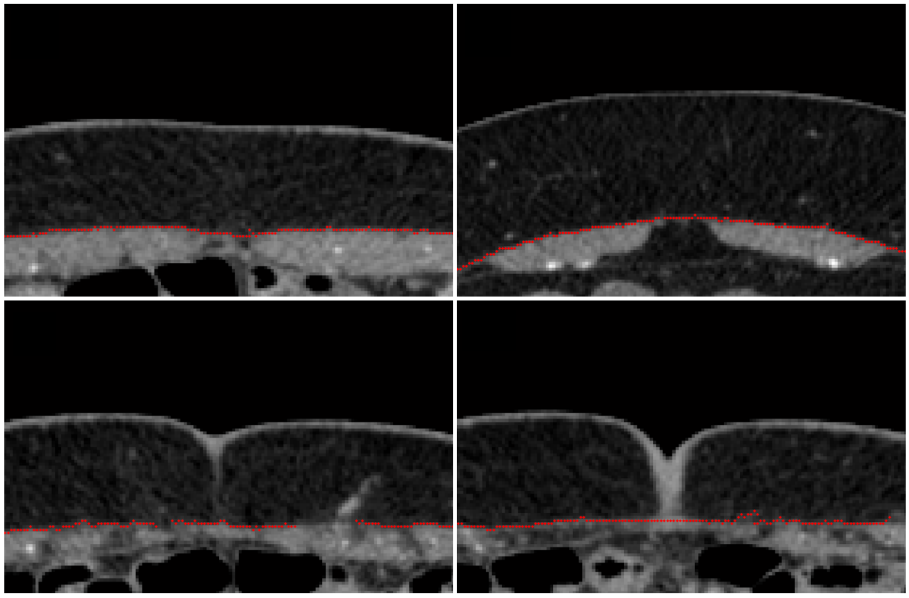

Figure 5.10: Raw fascia segmentation of the example images of Figure 5.3.

5.1.2.2 Second-phase: Local linear regression

After obtaining a raw segmentation of the *fascia* for each axial slice, a local least-squares linear regression along the sagittal anatomical plane is proposed, in order to return a *fascia* segmentation which is smoother, complete and less prone to vessel influence. Images a,c,e) of Figure 5.11 show sagittal slices along with the raw *fascia* segmentations obtained after phase 1. It is clear that the boundary between the *Rectus* muscle and the subcutaneous region is very smooth in this anatomical plane.

For each row of each sagittal slice of our volume of interest, a new *fascia* point will be estimated, by performing a local least-squares linear regression using the neighbor sagittal raw segmentation points. The number of neighbor points which influence the regression controls the smoothness factor. The higher this number, the smoother the final *fascia* segmentation will be. Basically, it controls the compromise between the amount of structure influence which can be neglected (like vessels) and the underlying curvature of the muscle that can be modeled. Let r be the index of the row at which the *fascia* point will be estimated and n the number of neighbor *fascia* raw points which will be used in the regression, such that the *fascia* point estimation is influenced by the raw *fascia* points that exist in the $[r-n \quad r+n]$ interval. The following expression was considerd to calculate n:

$$n = k \cdot m/s \tag{5.1}$$

where s is the distance in *mm* between consecutive pixels, characteristic of the volume (same in every direction of the volume after interpolation of data), m is the size of the biggest structures to be neglected, also in *mm* (for example, vessel caliber), and k is a constant. This last parameter

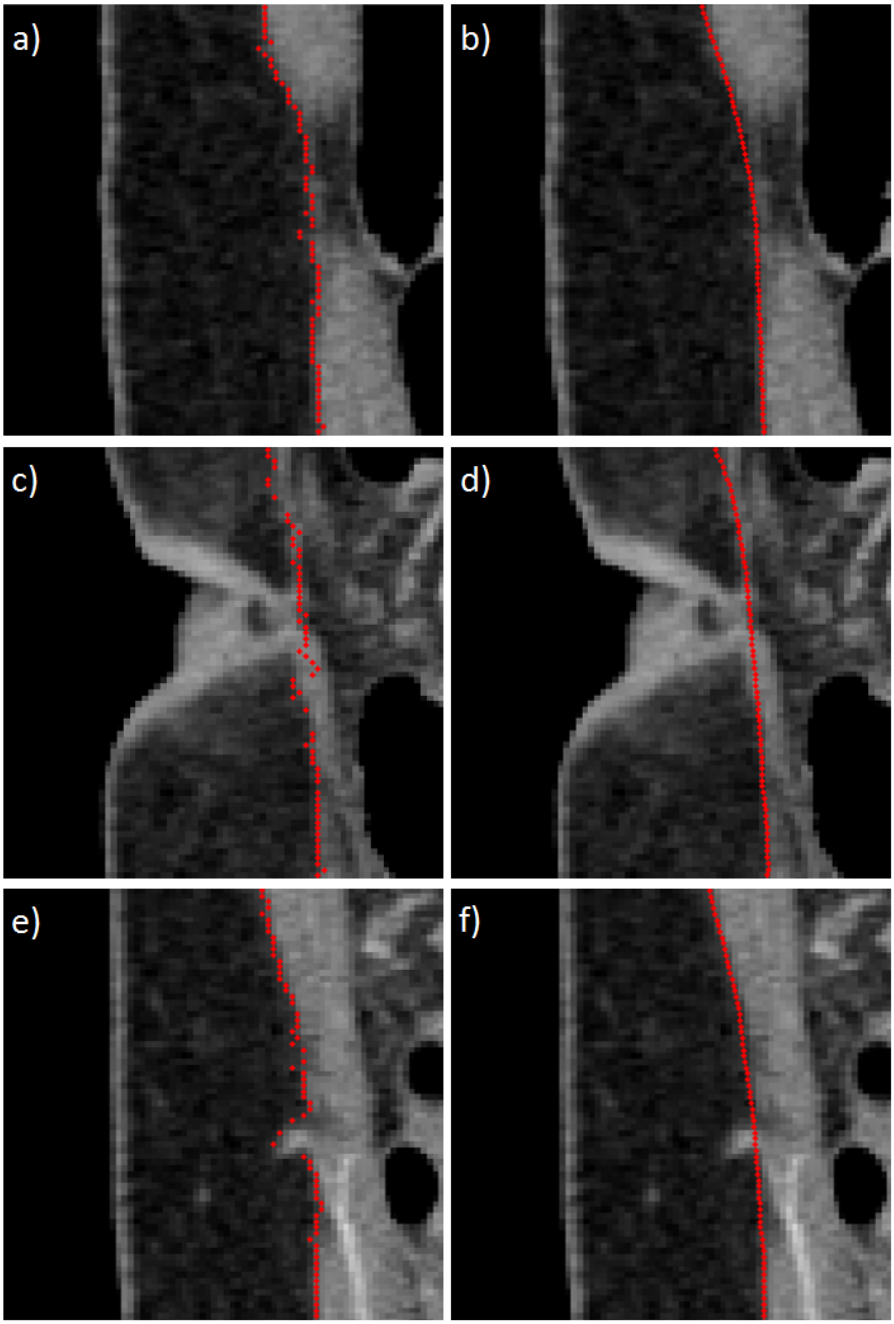

Figure 5.11: Example sagittal slices of the volume of interest with the fascia segmentations in red. a,c,e) raw segmentation obtained after phase 1; b,d,f) segmentation after phase 2 is employed.

can be seen as the amount of data which has to be considered to remove the influence of a certain structure. In this thesis, $m = 5$ was considered, and $k = 5$ was empirically obtained.

The effectiveness of this approach can be visualized in images b,d,f) of Figure 5.11, where example *fascia* segmentations are present.

As expected, the local regression framework allows to, not only smooth the initial result, but

also remove the undesired vessel detections. A clear example of this is present in image f) of Figure 5.11. Returning to the example axial slices which are being used along this section, the final segmentation can be seen in Figure 5.12.

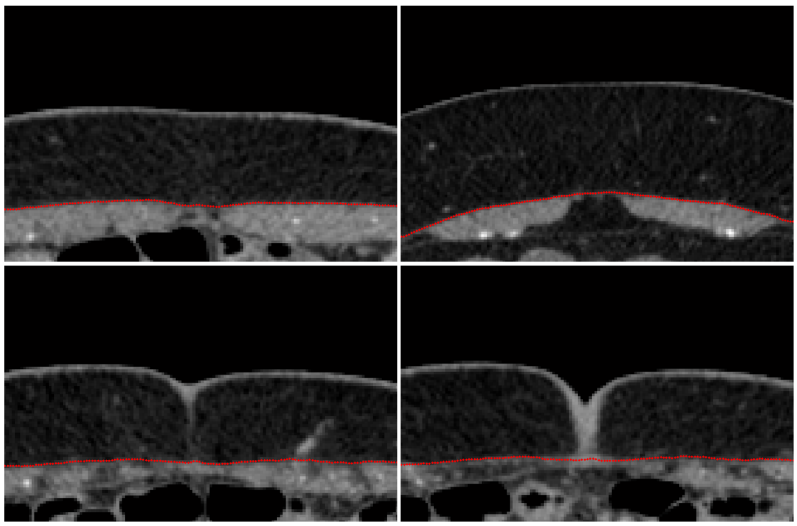

Figure 5.12: Fascia segmentation after the second phase of the proposed algorithm.

Nonetheless, there were rare cases where some of the post-processing steps used in the first phase of the algorithm failed. Between those cases, the most common problem occurred when the muscle was not a coherent object, but it spawned over all the columns because other bright structures made this possible (see Figure 5.13).

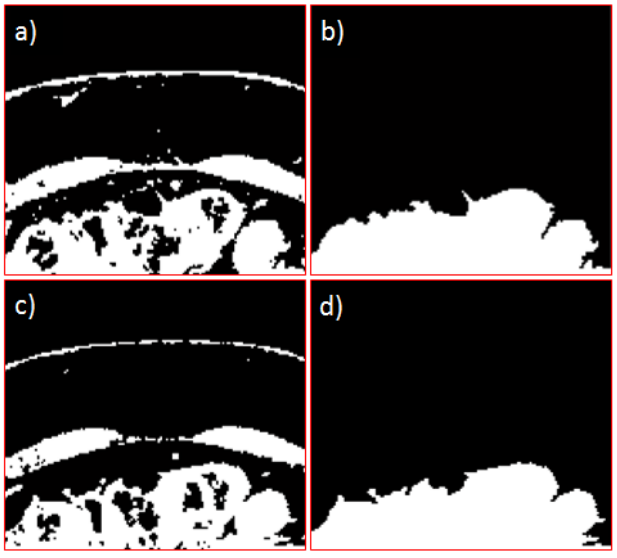

Figure 5.13: Example slices where the biggest connected component is not the muscle object. a,c) Segmentations using the threshold given by Otsu's method; b,d) filled object after keeping the biggest connected component.

This will incorporate in the raw *fascia* segmentation several points which can be considered outliers (see images a,d) of Figure 5.14). Under these conditions, the least-squares linear regression is not able to provide a good fit, since the outliers can be seen as non-Gaussian error distribution and have a large influence on the regression because squaring the residuals magnifies the effects of these extreme data points (see images b,e) of Figure 5.14). To solve this, a robust least-squares regression which uses a bisquare objective function to weight each data point according to its distance to the regression line, was used. This property seeks the line which fits better the majority of the data, reducing the influence of outliers. Images c,f) of Figure 5.14 show that this robust regression was able to improve the results under these conditions.

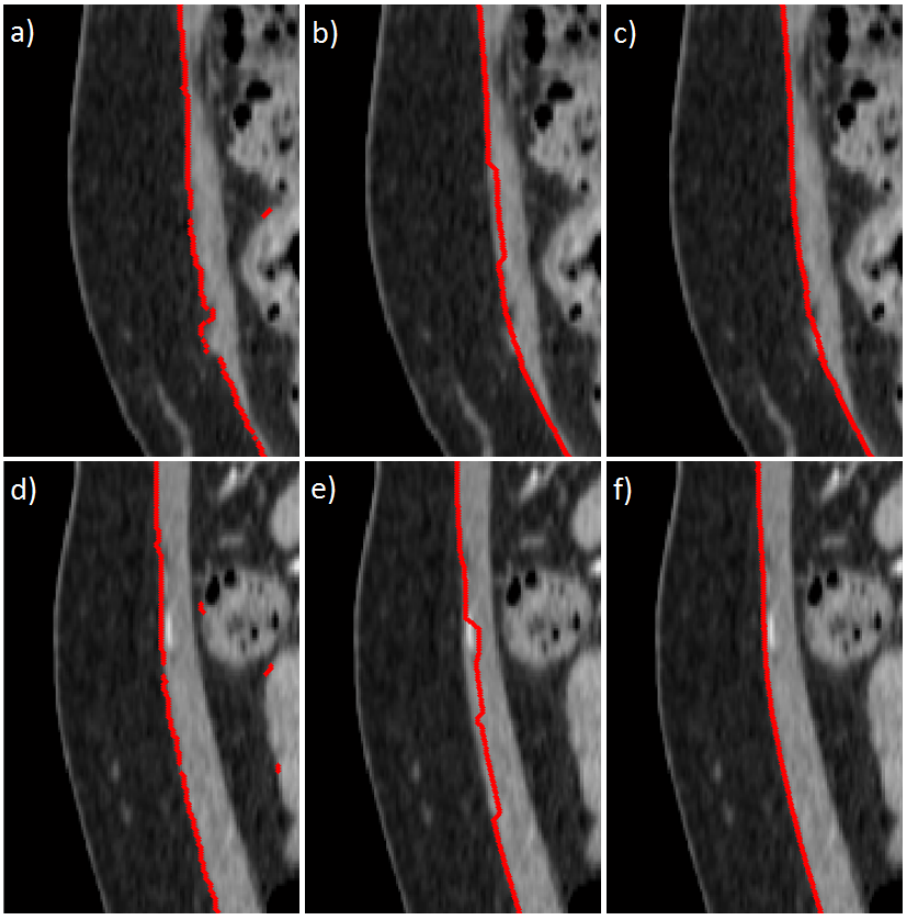

Figure 5.14: Comparison between the raw segmentation after phase 1 (a,d), the segmentation after phase 2 using the least-squares local linear regression (b,e) and using the robust local linear regression (c,f).

5.1.3 Results

For each volume of the database, a manual annotation of the anterior *fascia* layer was made, as already described, and compared to the segmentation obtained with both regression frameworks.

The mean Euclidean and Hausdorff distances were calculated and the results obtained are summarized in Table 5.1. The results obtained for each volume are present in Appendix B.

Table 5.1: Results obtained by the proposed *fascia* segmentation method. The mean Euclidean and Hausdorff distances between the segmentations and the manual annotations, and the average execution time, are shown for each regression method.

Regression method	**Euclidean Distance (mm)**		**Hausdorff Distance (mm)**		**Mean time (s)**
	GT → Seg	**Seg → GT**	**GT → Seg**	**Seg → GT**	
normal	0.62 ± 0.36	0.64 ± 0.42	1.77 ± 0.81	1.87 ± 1.11	30.01 ± 8.07
robust	0.49 ± 0.33	0.51 ± 0.40	1.52 ± 0.76	1.63 ± 1.15	636.21 ± 167.63

The voxel spacing differs between the volumes of the database, but in the majority of the cases it lies between 0.7 and 0.9 *mm*. This shows that both regression methods were able to provide segmentations whose mean distance to the manual annotations was lower than the spacing between consecutive voxels. As expected, the bilinear regression lead to a better performance. Nevertheless, that comes at an increased computational cost. Using an Intel Core i7-4500U CPU 1.80@2.40GHz, the average run time was 636 *s*, significantly higher than the average 30 *s* which took to perform the least-squares regression. There was a case (Patient 4321) where the resulting segmentations in a region of the volume were erroneous (see Figure 5.15). This occurred because in that region, the raw segmentation contained a high number of outliers, and neither of the regression methods was able to provide an accurate result.

5.1.4 Summary

The developed framework should be able to detect the location where the perforators leave the *fascia* layer, not only because it is needed to create the map of the perforators, but also because it allows to distinguish the subcutaneous region from the muscle one, making possible the division of the perforator detection problem in two.

This section focused on the segmentation of the anterior *fascia* in each slice of the target CTA volume. To achieve such task, an initial Otsu-based segmentation was made, being followed by a two-phase method which returns the anterior *fascia* contour for each slice of the volume. The first phase employs a series of post-processing operations in order to keep the interface between the subcutaneous area and the *rectus abdominis* muscle. The second phase smooths the raw segmentations and removes distortions caused by vessels by means of local linear regressions on the sagittal anatomical plane.

The Euclidean and Hausdorff distances between the results achieved with the proposed algorithm and the manual segmentations were calculated. With the exception of one patient volume, a mean Euclidean distance equivalent to one pixel spacing or lower was reached. The volume for which the algorithm produced worse results had several slices where the bright regions below the muscle lead to the malfunction of the first phase of the algorithm, such that the regression phase was not able to provide good results in certain regions.

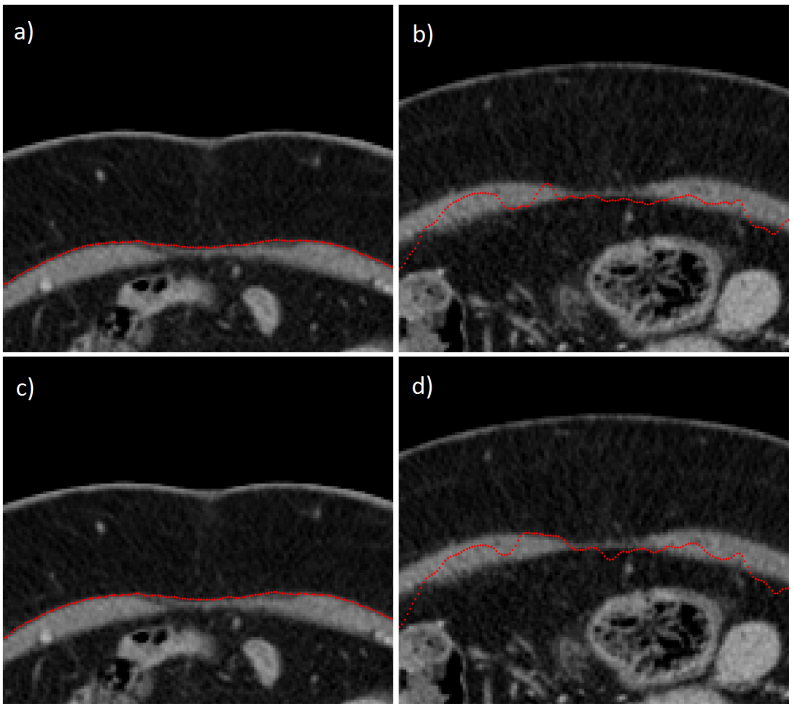

Figure 5.15: Two axial slices of different regions of patient 4321 with fascia segmentations in red. a,b) segmentations obtained with the least-squares regression; c,d) segmentations obtained with the robust regression.

5.2 Perforator Subcutaneous Course Tracking

This section focuses on the detection of the subcutaneous region of the perforators, which is the first region extracted by the proposed method. To accomplish such task, a tracking framework that estimates new centerline points from an initially given point was developed. This type of algorithm can be divided in three main steps: initialization, method used to estimate new points and ending criteria. Next, each of these steps is characterized according to the developed framework.

5.2.1 Initialization

As stated in the introduction of this Chapter, the locations where each perforator ends were manually given by the user. Then, at this stage, the tracking procedure of a perforator starts at the corresponding available landmark. Figure 5.16 shows some examples of this initialization step.

5.2.2 Tracking procedure

Tracking methods employ local measures to estimate consecutive points along the object of interest. Here, the structures of relevance are the DIEA perforators, which have a tubular shape and are brighter than their neighborhood. Thus, the proposed method estimates new centerline points

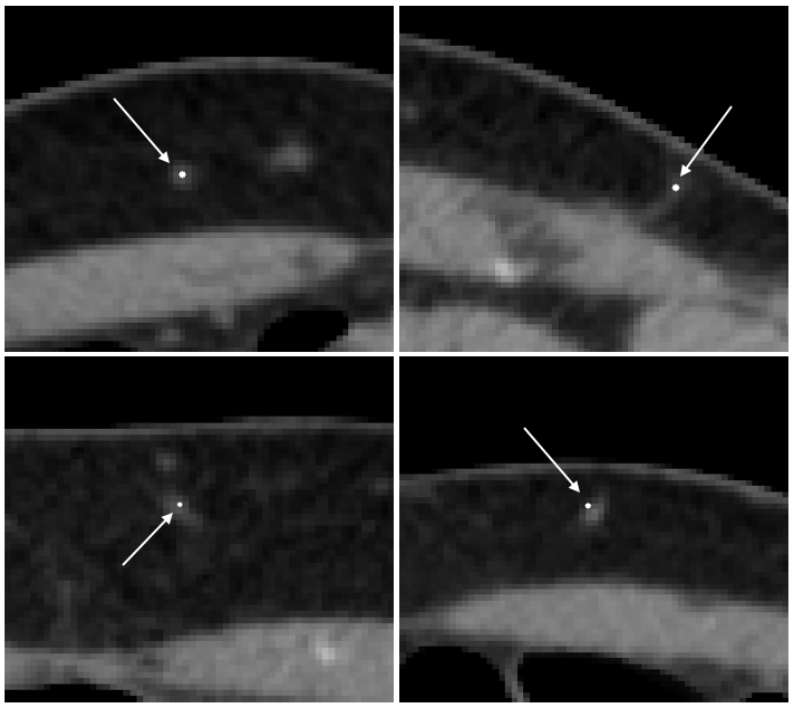

Figure 5.16: Slices showing example manual initializations (white) near the end of the subcutaneous portion of perforators.

along the perforator until the ending criteria is reached (subsection 5.2.4). The points are predicted according to the local vessel direction:

$$CP_{t+1} = CP_t + s \cdot \hat{\boldsymbol{v}} \tag{5.2}$$

where CP_t is the centerline point estimated at iteration t, s is a scalar which controls the step given between consecutive centerline points and $\hat{\boldsymbol{v}}$ is the unit vector pointing towards the local vessel direction. The latter is estimated through the analysis of the local gradient vectors, based on Agam *et al.* [56]. The idea behind the method becomes more clear by first imagining a cylinder brighter than its neighborhood. The local gradient vectors are expected to be normal to the cylinder surface (see Figure 5.17).

The direction of the cylinder is the direction which is orthogonal to those gradient vectors. Considering now the perforators, whose signal is contaminated with noise, the local gradient vectors will diverge from the ideal example situation. Nonetheless, in theory, the vessel direction $\boldsymbol{v}$ is the one which minimizes the squared projection of the local gradient vectors into $\boldsymbol{v}$:

$$E(\boldsymbol{v}) = \frac{1}{n}\sum_{i=1}^{n}((\boldsymbol{g}_i)^T\boldsymbol{v})^2 = \boldsymbol{v}^T(\frac{1}{n}\sum_{i=1}^{n}(\boldsymbol{g}_i)(\boldsymbol{g}_i)^T)\boldsymbol{v} \tag{5.3}$$

where n is the number of local gradient vectors and $\boldsymbol{g}_i$ is the ith gradient vector. By denoting $G \equiv (1/\sqrt{n})[\boldsymbol{g}_i,\ldots,\boldsymbol{g}_n]$, the previous expression becomes $E(\boldsymbol{v}) \equiv \boldsymbol{v}^T GG^T\boldsymbol{v}$, where GG^T is a 3x3

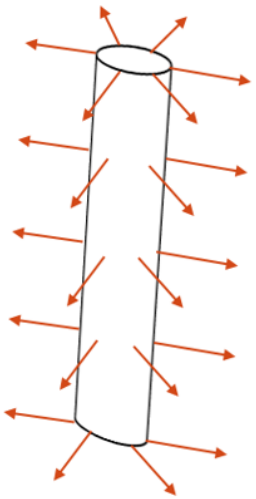

Figure 5.17: Tubular structure which is brighter than the background and corresponding gradient vectors, represented by red arrows.

correlation matrix. As proven by Agam *et al.* [56], the minimum of $E(\boldsymbol{v})$ is obtained by the eigenvector of GG^T belonging to its smallest eigenvalue.

Then, to estimate CP_{t+1}, the gradient vectors contained in the neighborhood of CP_t are used. This neighborhood is given by a $p \times p \times p$ window. Figure 5.18 shows this relation.

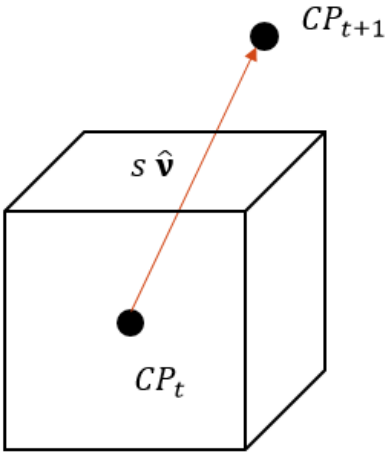

Figure 5.18: Representation of an iteration of the tracking procedure.

Although this allows to find the local direction of a vessel which goes through the window, notice that it does not guarantee that the estimated centerline point is near the center of the vessel. By analyzing the situations presented in Figure 5.19, it becomes clear that, if CP_t is not near the center of the vessel, CP_{t+1} estimation will also be erroneous, this is, the algorithm is not able to naturally correct offsets which might appear due to noise, the presence of other structures or even

abrupt direction changes.

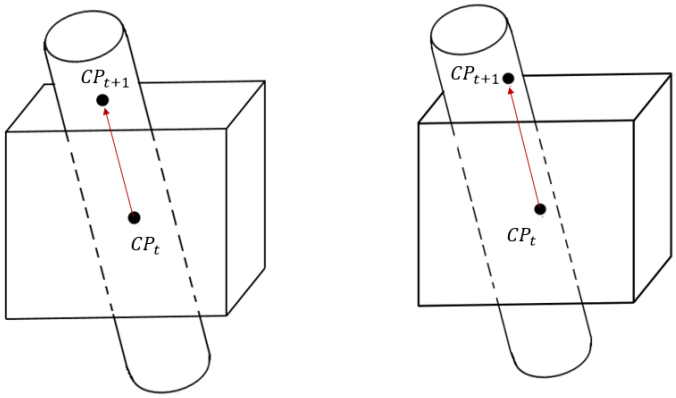

Figure 5.19: Iteration of the tracking procedure without and with the presence of an offset, respectively.

As shown in Figure 5.20, this situation tends to become more evident with the increasing number of iterations.

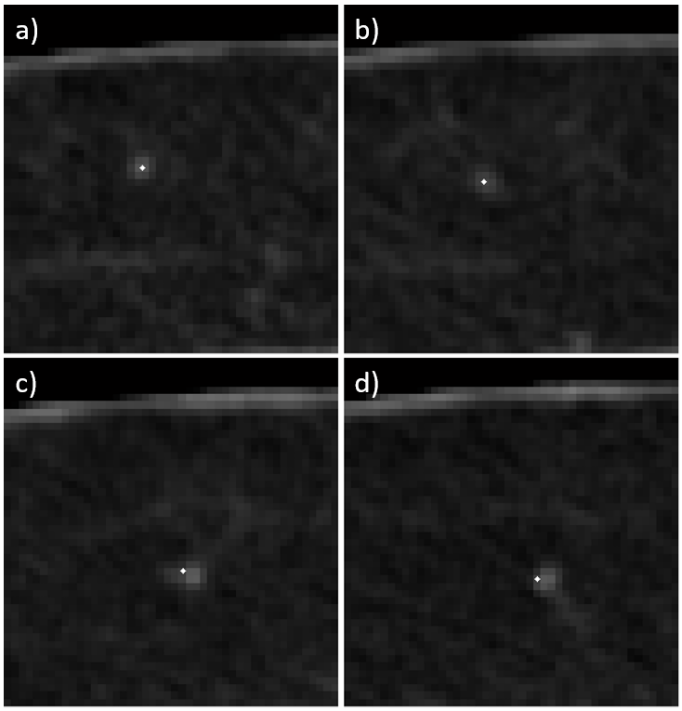

Figure 5.20: Example of the propagating offset error during the tracking procedure.

To correct this problem, an additional measure is used, which is incorporated in the framework through a Kalman filter [82]. It relies on the assumption that voxels on the center of the vessel have higher intensity and that it decreases as the distance to the center increases. In a 2D image of

the cross section of a vessel, it is then expected that the center location can be found by analyzing the divergence of the gradient vector field.

After predicting the position of the new centerline point $\widehat{CP}_{t+1|t}$, using the local gradient vectors information, the plane which contains that point and is orthogonal to the vessel direction $\boldsymbol{v}$ is obtained (see Figure 5.21). It is expected that this plane includes a roughly circular brighter region which is the 2D cross section of the vessel. Figure 5.22 shows some examples of the images obtained this way.

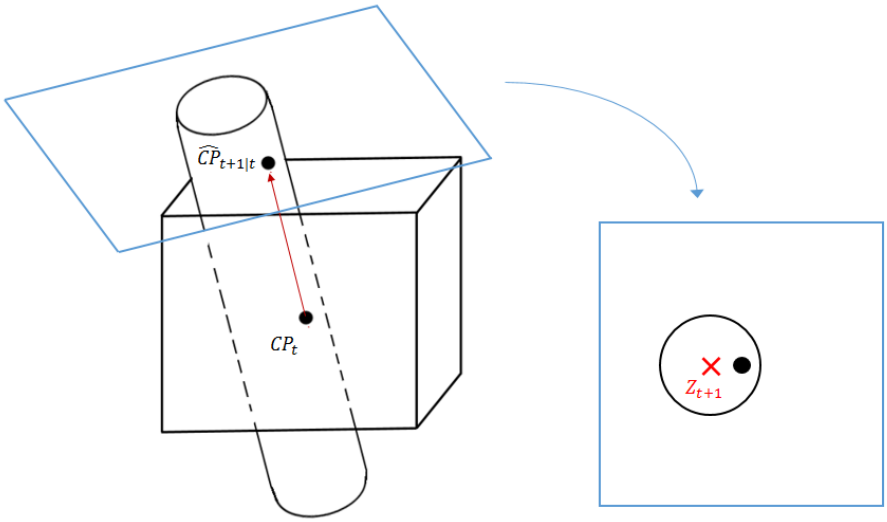

Figure 5.21: Diagram representing the prediction obtained by analyzing the local gradients, $\widehat{CP}_{t+1|t}$, and the correction measure, Z_{t+1}. The final estimate CP_{t+1} is given by a Kalman filter which fuses the information.

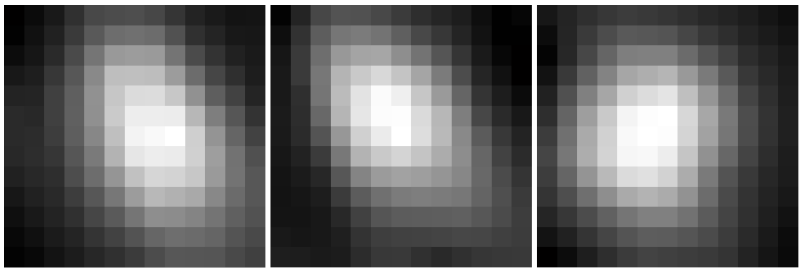

Figure 5.22: Cross section planes obtained with the proposed method.

As can be concluded, for smaller vessels, there is a tendency to occur a deviation from a circle to an ellipsoid. This probably happens due to three reasons: first, a smaller vessel is able to change more rapidly of direction, such that the estimated cross section plane will not be orthogonal to the vessel longitudinal axis; second, the SNR of small vessels is lower and the estimated local vessel direction is more prone to be erroneous; finally, the intensity information of small vessels is

much more sparse and the interpolation required to obtain the intensities of an oblique plane will commonly fail to produce the expected results.

Even so, it is still possible to find the center, by means of the gradient vector field divergence analysis, and perform the correction. To achieve such task, the 2D cross section image gradient vector field is obtained [83]. Consider the template represented in Figure 5.23, whose similarity to the gradient vector field is assessed through cross-correlation:

$$(\boldsymbol{f} * \boldsymbol{g})[n] \stackrel{\text{def}}{=} \sum_{m} \boldsymbol{f}^{*}[m]\boldsymbol{g}[n+m] \tag{5.4}$$

where $\boldsymbol{f}$ and $\boldsymbol{g}$ represent the gradient orientation vector field and template vector field, respectively, and $\boldsymbol{f}^{*}$ is the complex conjugate of $\boldsymbol{f}$. The center location estimation corresponds to the maximum response location (see Figure 5.24).

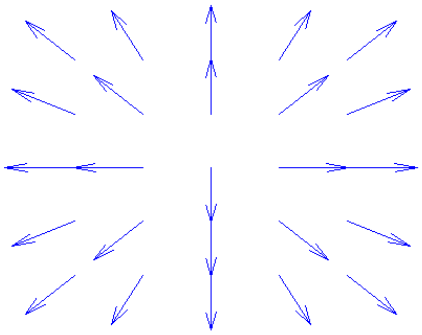

Figure 5.23: Template for locating the ridge point.

As already stated, this measure is introduced in the framework by means of a Kalman filter. As it aims to correct the offset which might appear throughout the tracking procedure, it is only taken every k iterations. For iterations where it is available, the estimation of CP_{t+1} is given by:

$$CP_{t+1} = \widehat{CP}_{t+1|t} + K_t(Z_{t+1} - H_t\widehat{CP}_{t+1|t}) \tag{5.5}$$

where $\widehat{CP}_{t+1|t}$ is the prediction based on CP_t and local vessel direction $\boldsymbol{v}$, Z_{t+1} is the correction measure (see Figure 5.21), K_t is the Kalman gain, and H_t is the matrix that maps the correction measure referential to the reference one. Basically, the final estimation will be somewhere between the prediction and the correction measure, according to the Kalman gain, which takes into account the uncertainty of the information coming from each of them. For iterations where the correction measure is not available, $CP_{t+1} = \widehat{CP}_{t+1|t}$.

5.2.3 Caliber estimation

As already discussed, the caliber of perforators is one of the parameters that the medical personnel registers while performing the study, usually reported at the region where the perforators leave the *fascia*. The presence of the muscle makes the task difficult in terms of image processing. Hence,

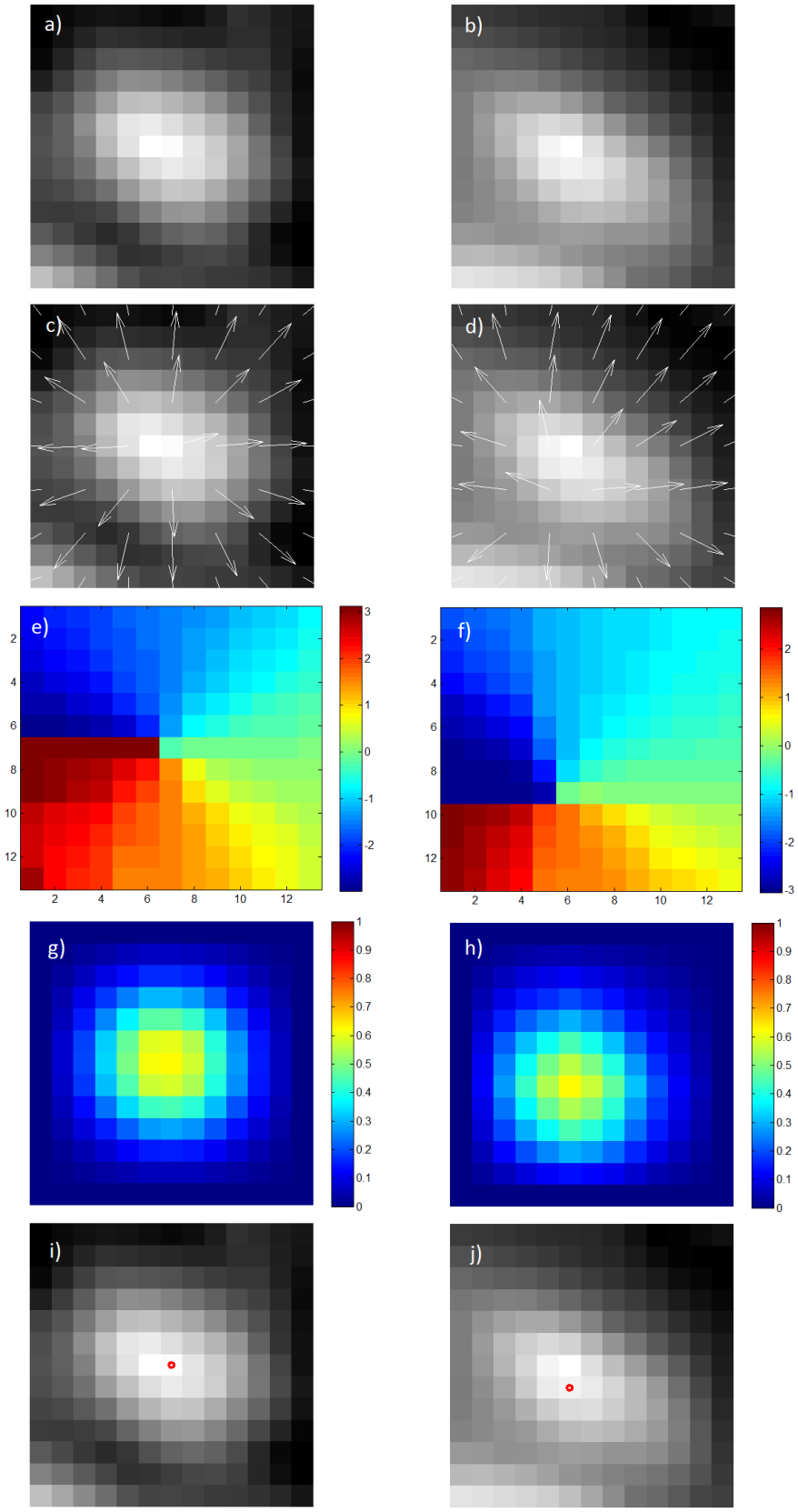

Figure 5.24: Centerline point correction measure. a,b) initial cross section images; c,d) gradient vector fields; e,f) gradient orientation images (values in radians); g,h) inner product responses; i,j) center estimations.

the proposed method takes a caliber measure at each tracking iteration, and combines them after the procedure ends, in order to have a global caliber estimation.

The tracking procedure uses the local vessel direction $\boldsymbol{v}$ at CP_t in order to estimate $\widehat{CP}_{t+1|t}$. The projection of $\boldsymbol{v}$ on the axial plane which contains CP_t can be used to extract the line which is orthogonal to it and belongs to that plane (see Figure 5.25). This line cuts through the cross section of the perforator at the axial plane.

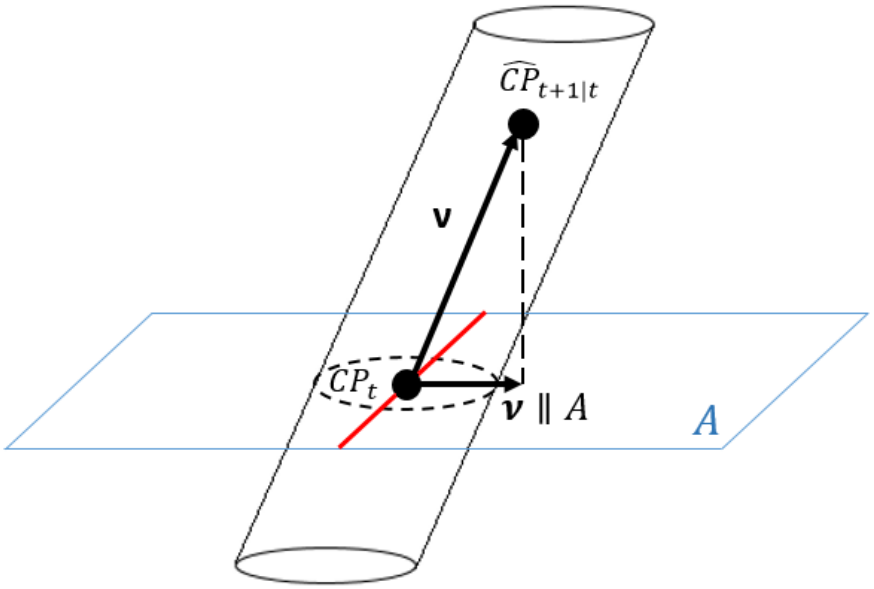

Figure 5.25: Representation of the process to obtain the line (red) which goes along the axial cross-section of the vessel. $\boldsymbol{v}\|A$ is the projection of $\boldsymbol{v}$ into the plane A.

As the perforators usually have low SNR, the intensities along these cross section lines are extracted after the data is filtered by a phase preserving denoising algorithm proposed by Kovesi [84]. The method uses log-Gabor wavelets to extract local phase and amplitude information of the signal and automatically determines the wavelet shrinkage thresholds. Figure 5.26 shows examples of the post-processed images.

After the denoising filter is applied, the intensities across the lines follow more precisely a Gaussian profile (see Figure 5.27). To measure the caliber, first, a Gaussian is fitted to the intensities in a least-squares fashion (see Figure 5.28). Afterwards, its value is set to the width in *mm* covered by the 85% confidence interval. This value was emprirically regarded as the best for the data contained in the database. If the returned value is larger than 4 *mm*, it is rejected, since there are no perforators with such large caliber in the database and we assume the fitting process was compromised by a neighbor structure. To produce a single caliber estimation after the tracking procedure ends, the mean of the measures was considered. The results are presented and discussed in subsection 5.2.5.

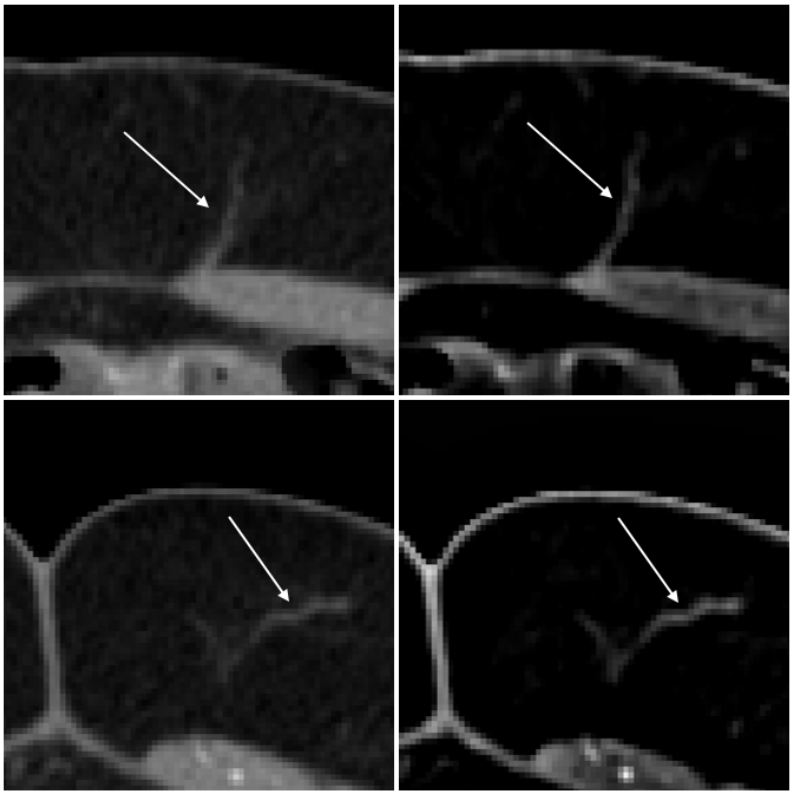

Figure 5.26: Two examples of axial slices before and after the Kovesi [84] denoising.

5.2.4 Ending criteria

The tracking procedure is stopped when the distance to the *fascia* mask (see Section 5.1) is lower than a certain threshold. In our experiments, this threshold was set to 0.5 *mm*. The last centerline point is considered the location where the perforator leaves the *fascia*.

5.2.5 Results

Across the volumes of the database, 74 subcutaneous perforator pathways were tested. For each of those vessels, the tracking procedure was initialized at the annotation which was closer to the end of the perforator. The final experiments used $p = 7$ for the $p \times p \times p$ window, $s = 1$ for the step scalar, took the correction measure at every k=5 iterations, and the Kalman gain considered the correction measure 10 times more reliable than the prediction one. These values were empirically determined. After the tracking procedure ended, the Euclidean and Hausdorff distances from the *Ground Truth* annotations to the extracted paths were calculated, since the first are more sparse than the latter (see Figure 5.29). Besides, the estimations of the caliber and the location where the perforator leaves the anterior *fascia*, were also compared to the *Ground Truth*. Note that, in order to create the map of perforators (see Figure 5.30), only the width and height of the location where the perforator leaves the *fascia* matters. Hence, the error was independently evaluated for both. The computational cost analysis of this method is not relevant, since tracking along a perforator

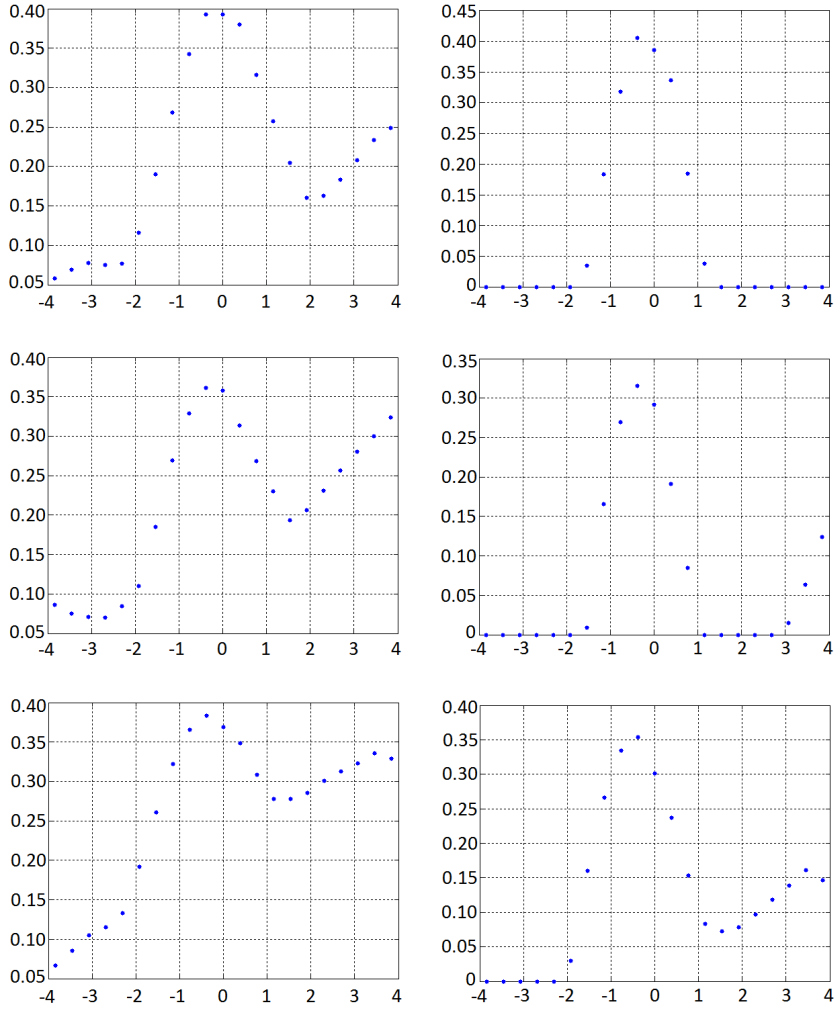

Figure 5.27: Intensities along axial cross section lines before (left column) and after (right column) the Kovesi [84] denoising process. The x-axis represents the position in *mm* relative to the line center and the y-axis the intensity.

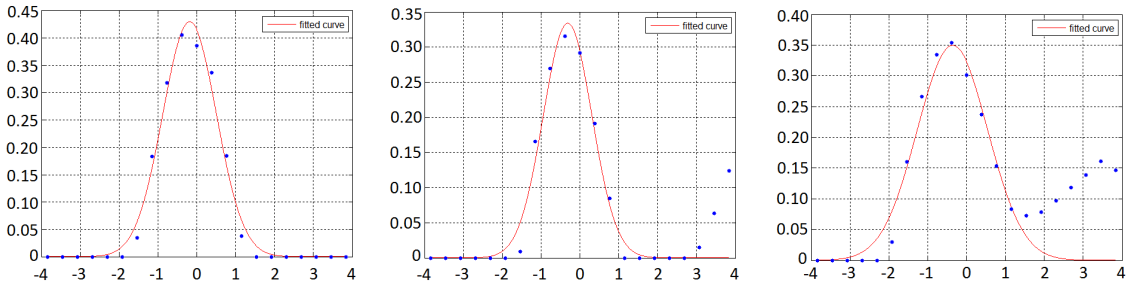

Figure 5.28: Gaussian fitting of the line intensity profiles considered as example in the right column of Figure 5.27. The x-axis represents the position in *mm* relative to the line center and the y-axis the intensity.

usually took just a couple of seconds. Table 5.2 summarizes the results obtained. The complete results are shown in Appendix C.

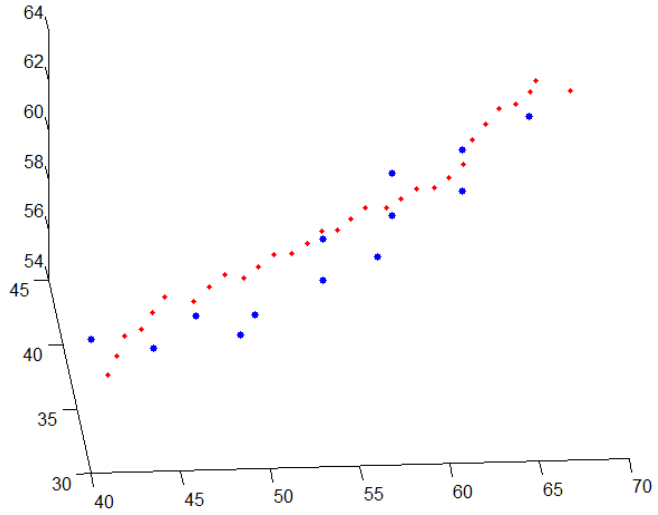

Figure 5.29: 3D comparison between a tracked path (red) and *Ground Truth* annotations (blue). The latter are more sparse than the first.

Figure 5.30: Perforator mapping. Adapted from [85].

Table 5.2: Results obtained by using the proposed tracking framework to detect the subcutaneous region of the perforators.

Path error (mm)		**Caliber error**		**Location error (mm)**	
Euclidean distance	**Hausdorff distance**	**Relative**	**Absolute (mm)**	**height**	**width**
1.35 ± 0.46	2.98 ± 1.46	15.4%	0.35 ± 0.27	1.40 ± 1.39	1.72 ± 1.49

A mean Euclidean distance error of 1.35 *mm*, considering that the spacing between voxels is around 0.7-0.9 *mm*, means that in average, the distance between a *Ground Truth* annotation and an estimated centerline point is almost two pixels long. As exemplified in Figures 5.31, 5.32 and 5.33, the proposed tracking procedure is able to successfully extract a perforator subcutaneous course. We believe that two reasons explain this error. First, the annotation provided by the radiologist is not in the form of a skeleton of the perforator, while our result is. This means that, even if our retrieved path is a perfect skeleton of the vessel, the provided *Ground Truth* annotations will lead to a significant error when performing the comparison (notice the first two cases of Figure 5.34). Second, the algorithm was not able to correctly track regions of the perforator where it gets adjacent to the muscle area and moves along it (see Figure 5.31 which shows that the tracking finished earlier due to this). Although it does not occur very commonly, it also explains the increased error. It is also the reason why the mean Hausdorff distance reached a relatively high value, 2.98 *mm*.

The caliber estimation method reached a mean error which corresponds to less than half of the spacing between consecutive voxels. Note that the caliber *Ground Truth* available comes from reports which were produced by different medical personnel, increasing the subjectivity behind the process. Thus, more conclusive results could be produced if the different individuals annotated the same data, such that the inter-operator variability could be measured.

Finally, in terms of stopping the tracking procedure at the correct location, one can notice that the error was higher in terms of width offset than height one. This happens because, the already explained behavior where perforators ocasionally move along the muscle, tends to occur through the axial plane. Then, stopping the tracking earlier due to the contamination of local gradient vectors by the presence of the muscle, commonly leads to a higher offset in width estimate then height.

5.2.6 Summary

This section described the proposed method for detecting the subcutaneous region of a perforator. Given a starting point at the end of the perforator, a tracking procedure based in the local gradient vectors information was used to estimate new centerline points along the vessel. Besides, a 2D cross section center detection feature was used to periodically assure that the tracking procedure was not impaired by the appearance of offsets. The process was stopped when the distance to the previously segmented anterior fascia became lower than a threshold. As the caliber of a perforator is also required to plan the surgery, at each iteration of the tracking procedure, a Gaussian is fitted to the intensity profile of the line which goes along the cross section of the perforator at the axial plane.

The results showed that the framework is able to correctly track along the perforators. Even though, it was not able to correctly determine the location where the perforator leaves the anterior *fascia* for cases where a significant course along that structure exists. Besides, the caliber estimation was able to achieve a mean error of around half a voxel spacing.

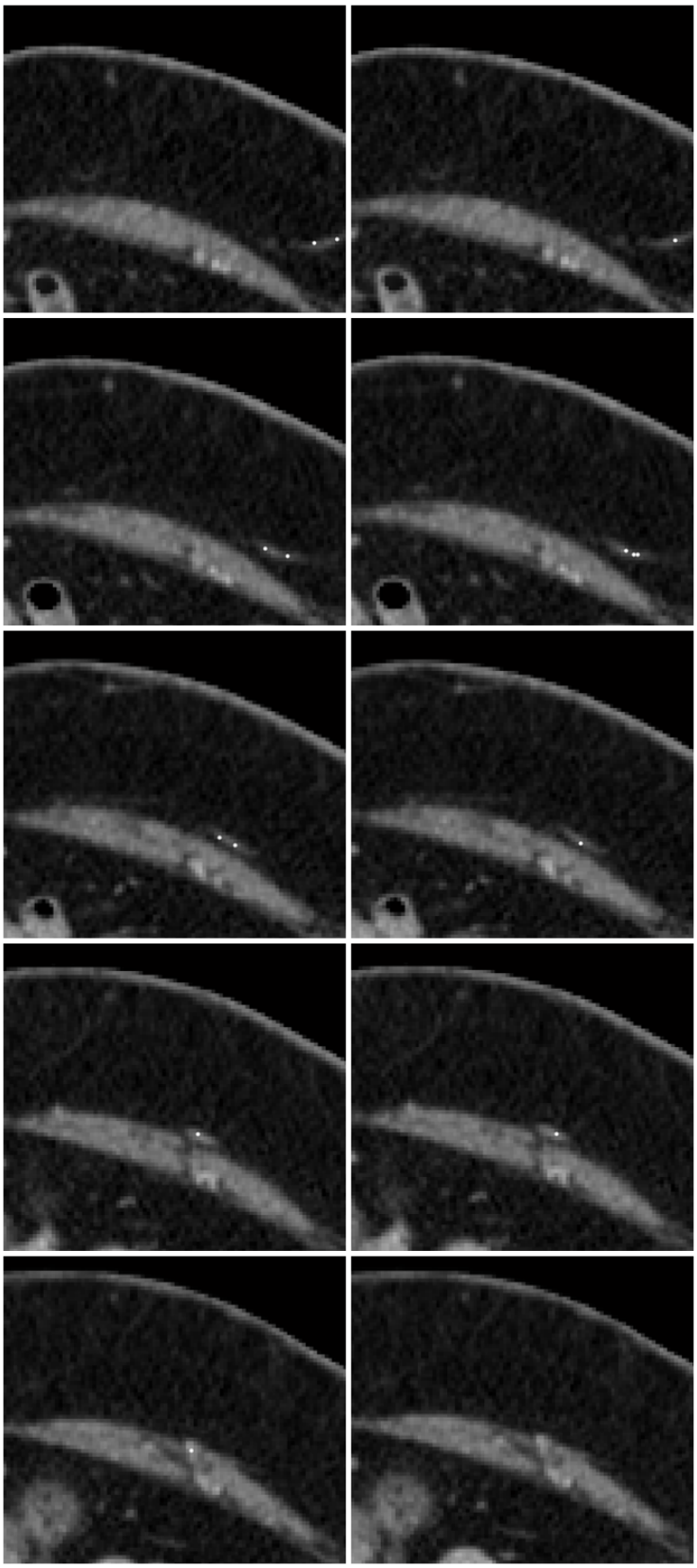

Figure 5.31: Slices of example case 1. Comparison between the *Ground Truth* (left column) and the tracked path (right column).

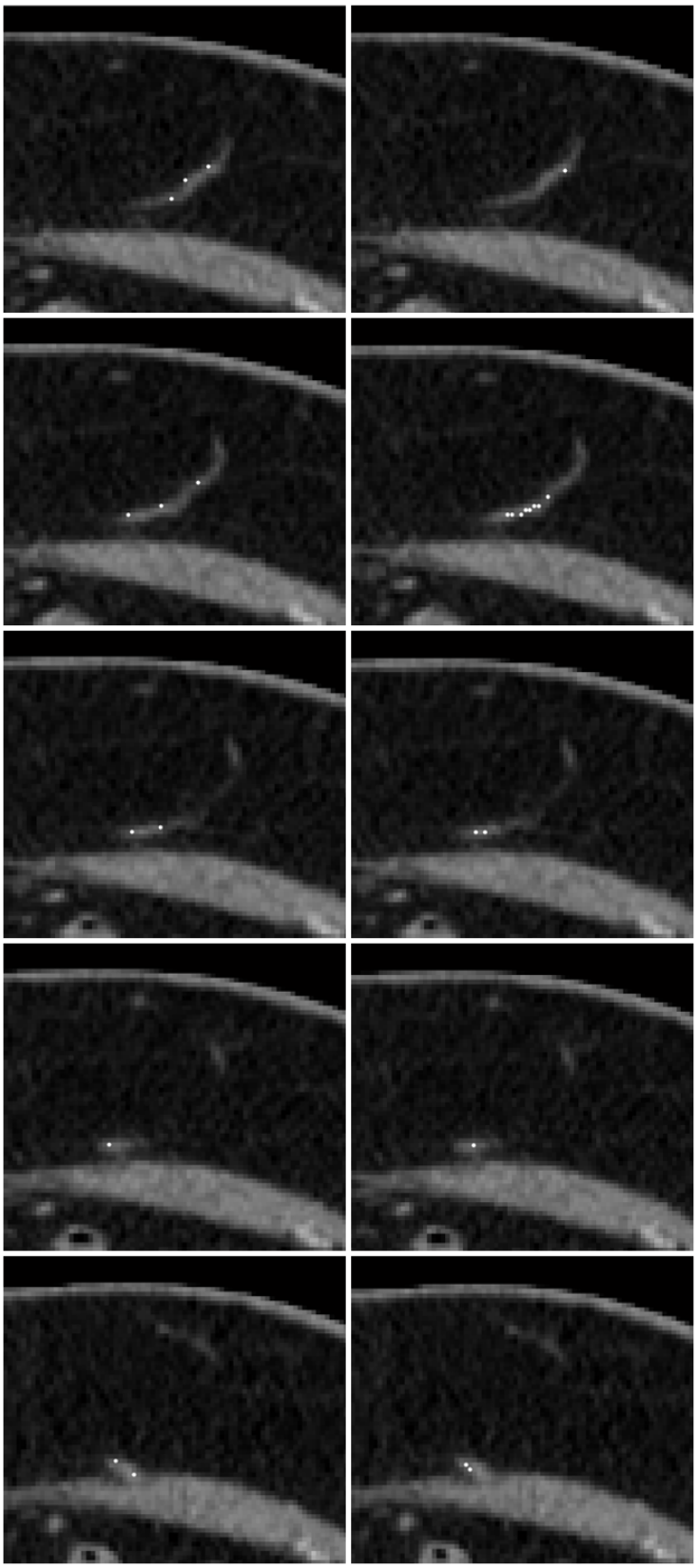

Figure 5.32: Slices of example case 2. Comparison between the *Ground Truth* (left column) and the tracked path (right column).

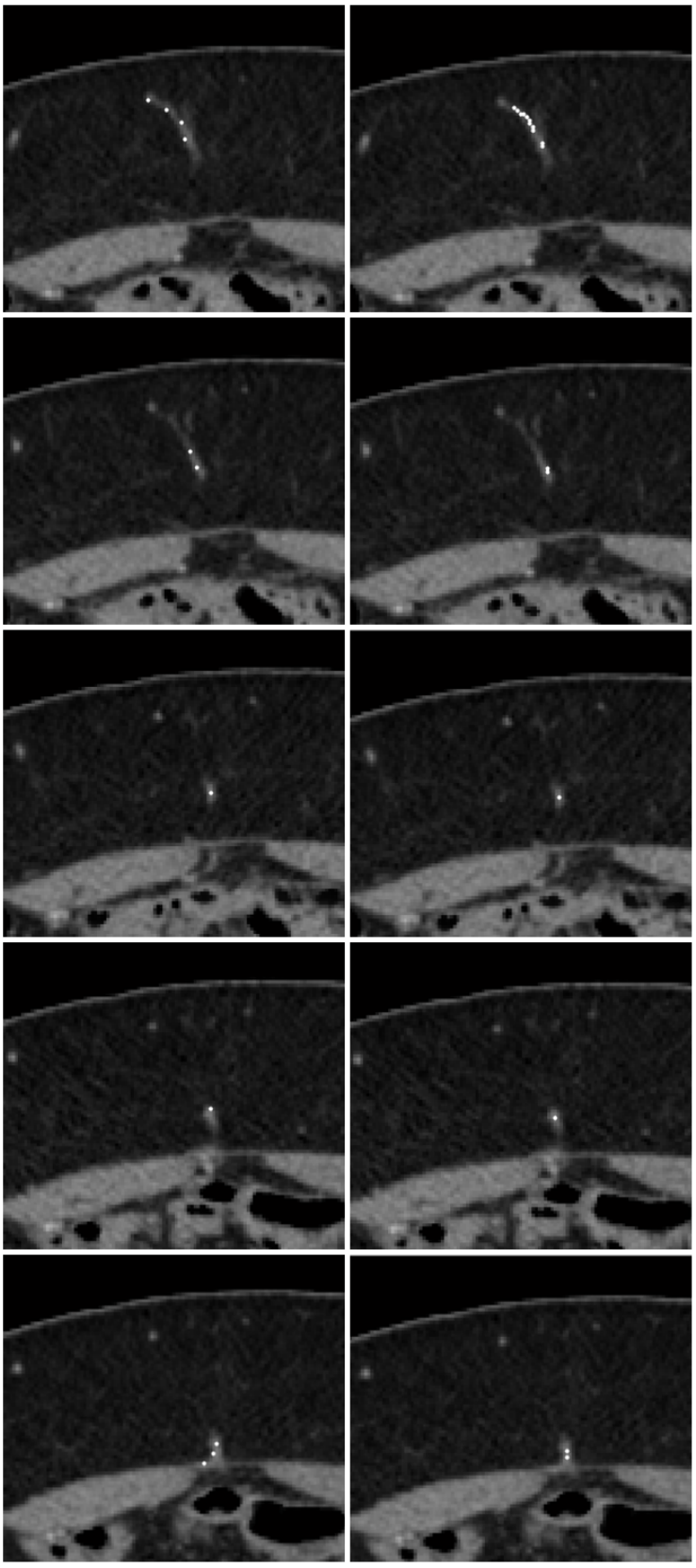

Figure 5.33: Slices of example case 3. Comparison between the *Ground Truth* (left column) and the tracked path (right column).

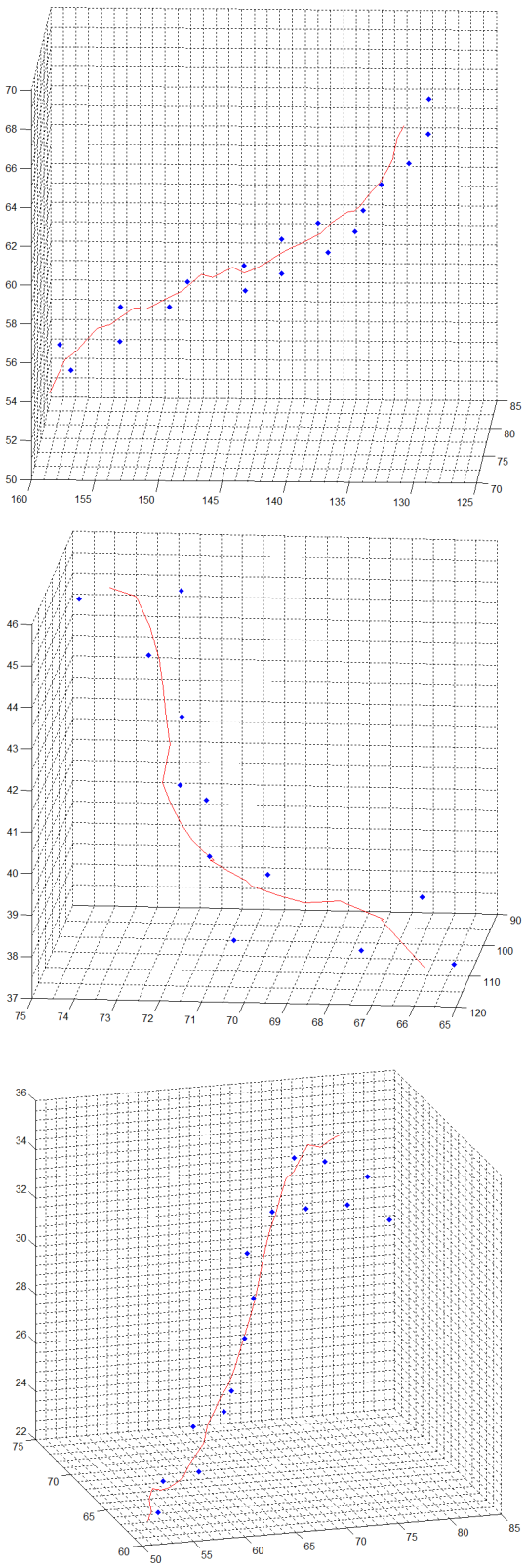

Figure 5.34: 3D comparison of the subcutaneous tracked paths (red) and *Ground Truth* (blue) of the examples used in Figures 5.31, 5.32 and 5.33, respectively.

5.3 Perforator Intramuscular Course Detection

After tracking the subcutaneous portion of the perforators and detecting the locations where they reach the anterior *fascia*, as already described, it is still necessary to find the intramuscular course of those perforators, since their length and tortuosity are key parameters for planning the surgery. Vessels with short and direct courses are easier to extract, reducing the complexity of the medical act.

The intramuscular course of the perforators commonly presents very low SNR, mainly in the proximity of the anterior fascia, as shown in Figure 5.35. This makes the general tracking procedures not adequate for this task, since they have bad performace when local regions of the vessel pathway are absent and the signal is lost. Hence, this section presents a minimum cost path based approach to retrieve the intramuscular perforator pathways, which is more robust under the described conditions.

5.3.1 A* search algorithm

Minimum cost path approaches are able to surpass local signal losses, as long as it is strong enough in other regions. As the goal is to find the vessel pathways in a 3D volume, attention to the computational cost must be taken, since this approach easily becomes unfeasible when many voxels are visited (each voxel of the volume is a node under the syntax of minimum cost path methods). Since both the initial voxel (location where the subcutaneous tracking stopped) and the target one (manually given DIEA source) are known, the problem is already constrained to finding a path that connects two voxels, which leads to a decrease in the computational effort required. Even then, using a plain Dijkstra search method for such task might lead to visiting a high number of voxels. Thus, the use of the A* algorithm [86] is proposed, as it includes a heuristic to improve the search performance. This heuristic is problem related and the only requirement is that it must not overestimate the real cost to reach the target node, in order to guarantee that the shortest path is found. At each iteration, the A* search algorithm expands the path which minimizes the following expression:

$$f(n) = g(n) + h(n) \tag{5.6}$$

where n is the last node on the path, $g(n)$ is the cost of the path from the start node to n, and $h(n)$ is the heuristic that estimates the cost of the cheapest path from n to the goal. In this thesis, the Euclidean distance between n and the target voxel is used as the heuristic function. Notice that the Dijkstra search is a special case of the A* algorithm (when the heuristic $h(n)$ is 0).

5.3.2 Terrain costs

Usually, pathfinding related problems focus on searching the best path between two nodes of a grid map, where each grid location contains an obstacle or not. However, to find a perforator intramuscular course, different costs must be given to each voxel. This can be seen as if different

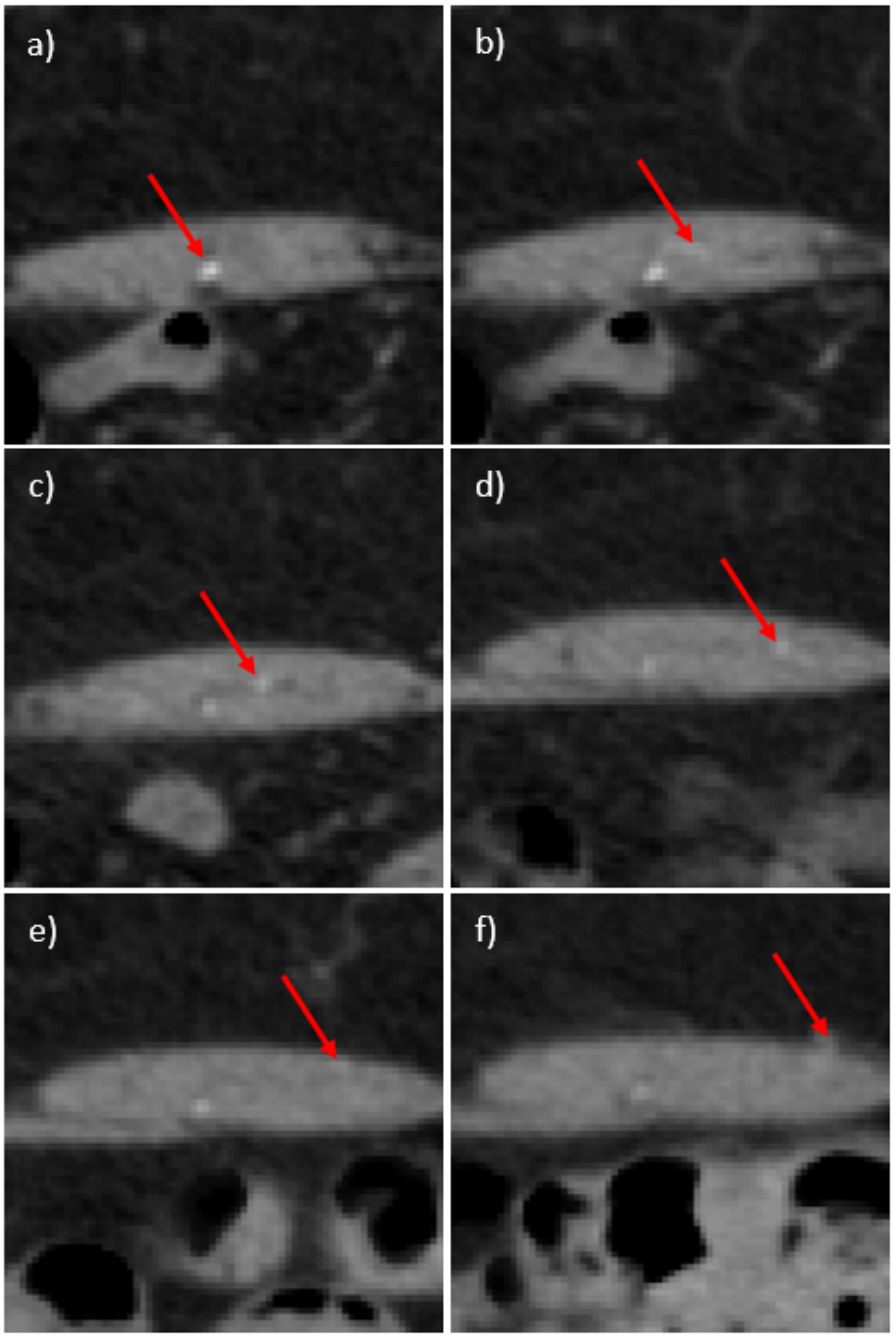

Figure 5.35: Slices showing the low SNR of an intramuscular perforator pathway, from its origin in the DIEA (a) to the location where it leaves the muscle (f).

terrains exist and is easier to travel along some of them. Instead of following the general formulation where the cost of going to a neighbor node is simply given by the distance between that node and the current one, the proposed method also takes into account the cost of the neighbor node.

Then, the cost of travelling from one node to another is given by the following expression:

$$c_{n,n+1} = d_{n,n+1} \cdot C(n+1) \tag{5.7}$$

where n is the current node, $n+1$ is the neighbor node, $d_{n,n+1}$ is the distance between those nodes (the Euclidean distance was considered in this thesis), and $C(n+1)$ is the terrain cost of the neighbor node.

The proposed algorithm must regard vessel voxels as easier to cross than non-vessel ones. The Frangi vesselness filter [54] is a state-of-art method for enhancing both 2D and 3D tubular structures, such as vessels. Although it is usually avoided for segmenting small and/or low SNR vessels, as it relies on the local second order partial derivatives, it might provide an useful input since minimum cost path methods should be able to find the correct path even if the signal is lost/weak in some regions. By applying the Frangi vesselness filter to the volume, the probabilities of each voxel being a vessel are obtained. After normalizing the resulting volume, F, to the range $[0\ 1]$, the cost volume, C, is given by:

$$C(n) = \begin{cases} 2 - F(n) & \text{if } F(n) > 0 \\ 10 & \text{if } F(n) = 0 \end{cases}$$

Voxels where $F(n) = 0$ are considered non-vessel and a relatively high cost is given to them (the value 10 was empirically determined). The remainder of the voxels have costs in the range $[1\ 2[$. Notice that, in order to keep the heuristic admissible (does not overestimate the cost of reaching the target node), the minimum cost of travelling from one node to another cannot be less than 1. This is the reason behind the transform applied to obtain the cost volume C.

Figure 5.36 shows slices that belong to one of the volumes from our database, and the corresponding costs obtained. The red arrows point to the intramuscular vessels that should be enhanced in order to be possible to correctly extract the vessel pathways of interest. It is possible to conclude that the structures of interest are being differentiated, but this also happens with vessels outside the muscle (which is expected) and some structured noise areas. This might put the correct extraction at risk because other potential minimum paths may exist.

5.3.3 Performance Optimization

Finding the intramuscular pathway of a perforator might imply analyzing grids with over 350000 nodes. The behavior of A* is closely related to the heuristic it uses, since it controls the compromise between performance and accuracy. The ideal heuristic is the one which is equal to the exact cost of moving from n to the goal node, which is impossible to determine in the considered problem. In fact, the Euclidean distance commonly underestimates in a significant amount the real cost of reaching the goal node, since perforators intramuscular course is frequently quite tortuous. This leads to the expansion of many nodes, making the algorithm very slow in some cases. To overcome this, an experiment which restricts the number of nodes in the open list was performed. As the A* algorithm executes, the number of nodes to expand increase and they are stored in the

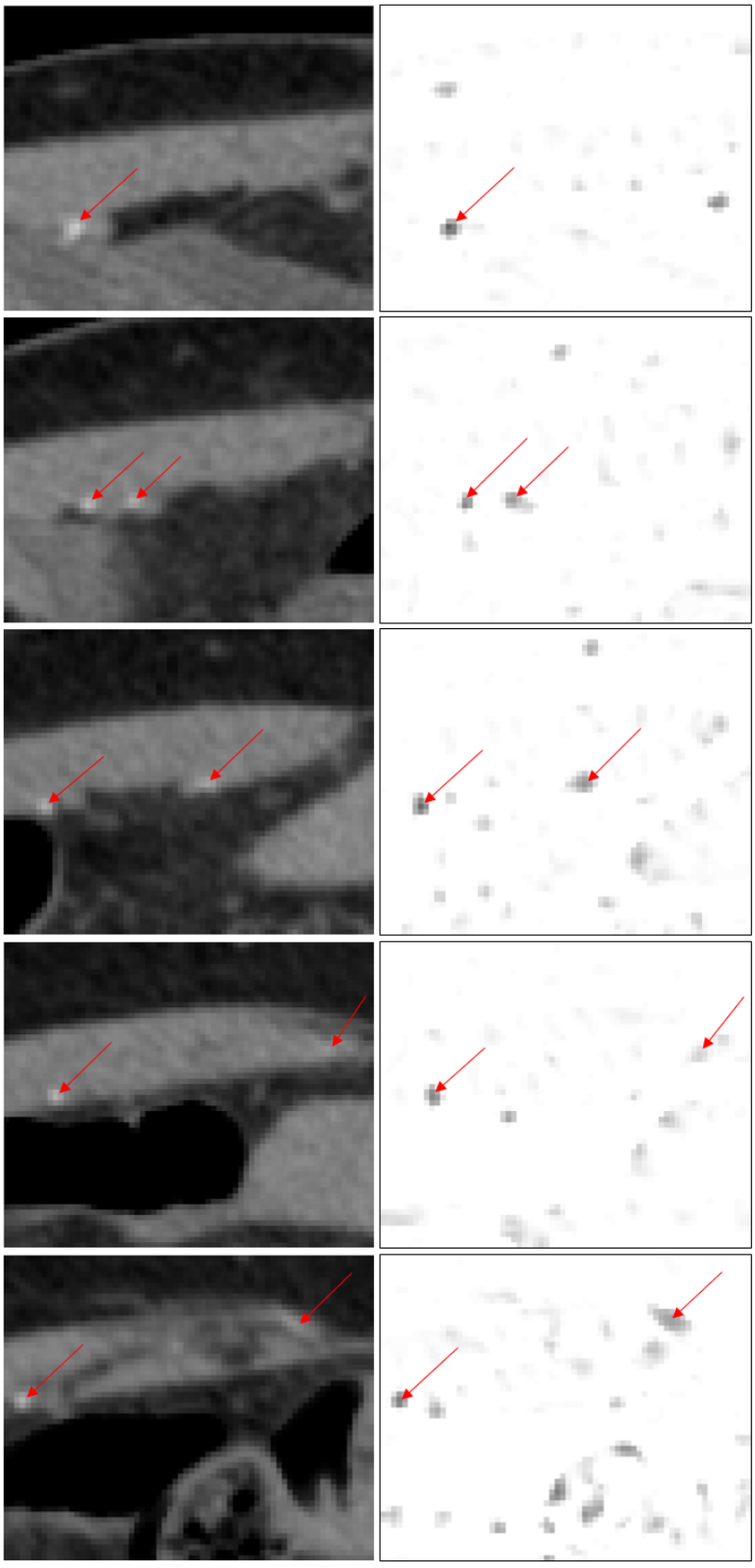

Figure 5.36: Different slices of a patient volume (left column) and corresponding costs obtained by applying the transform to the Frangi vessel probabilities (right column). Red arrows locate intramuscular vessels.

open list. The experiment restricts the maximum number of nodes in the open list to m, and when that happens, the k most promising nodes are kept and the rest goes to the closed list, where nodes that were already expanded lie. The criteria is the distance to the target node, this is, nodes which are closer to the target are favored. Although it cannot be assured anymore that the result is the shortest path, depending on the m and k values, the probability can still be very high. Furthermore, it is also a question of understanding if the shortest path is really required or a similar one is enough.

5.3.4 Results

The results here presented were obtained by setting $m = 1000$ and $k = 500$. Across the volumes of the database, there are 28 intramuscular perforator pathways whose *Ground Truth* annotations are, at least, partially available. For those cases, the start voxel was initialized at the location where the perforator leaves the *fascia* and the target voxel at the DIEA before the origin of the perforator. After the minimum paths were found, the Euclidean and Hausdorff distances from the *Ground Truth* annotations to the minimum cost path were calculated, since the first are more sparse than the 26-neighbor connected paths (see Figure 5.37). Table 5.3 summarizes the results achieved with the described method. Appendix D contains the complete results.

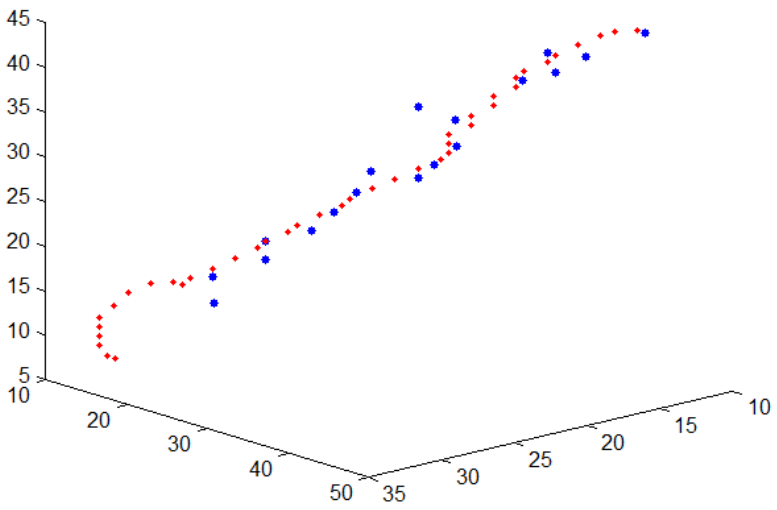

Figure 5.37: 3D comparison between an extracted path (red) and *Ground Truth* annotations (blue). The latter are more sparse than the first.

The retrieved Euclidean distance shows that, on average, the distance between the *Ground Truth* annotations and the estimated paths is 1.06 *mm*, a little more than one voxel spacing. It is believed that this error is being increased by the offset which commonly exists between the annotations and the true vessel locations. Figure 5.38 shows cases where the estimated path was correctly

Table 5.3: Results of the method proposed for the extraction of the intramuscular course of perforators.

Euclidean distance (mm)	**Hausdorff distance (mm)**	**Mean time (s)**
1.06 ± 0.32	2.44 ± 0.92	15.00 ± 14.76

passing through the vessel center, but even then, errors in the order of the voxel spacing would exist due to the described offset. Based on these findings, using the A* method with the proposed cost volume lead to the successful extraction of the intramuscular course of the perforators.

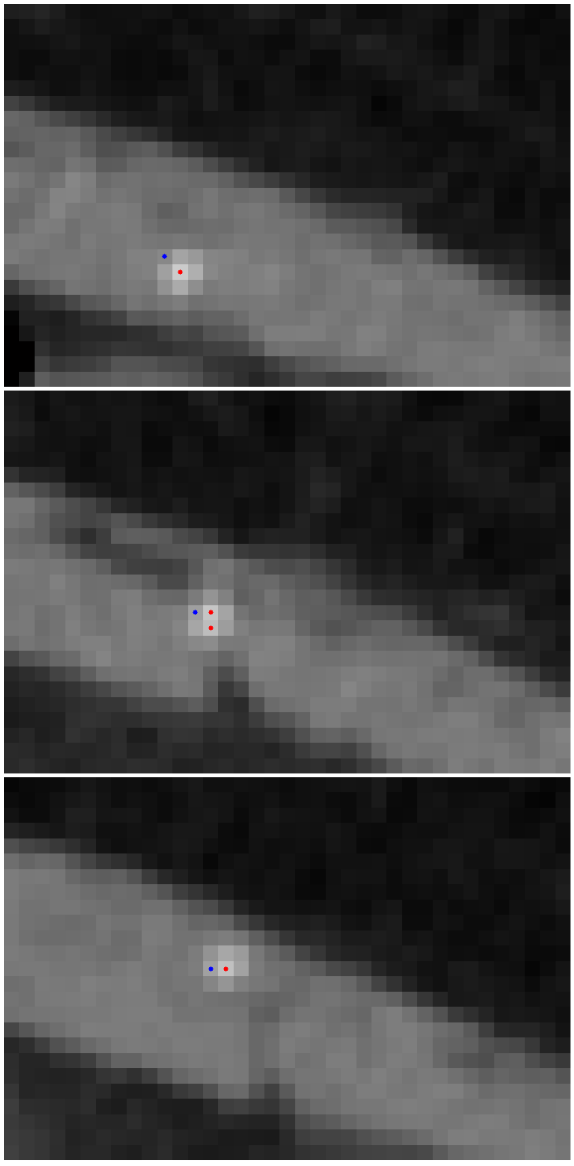

Figure 5.38: Examples of the existing offset in some cases of the *Ground Truth* annotation. Red points show the calculated path and blue ones the *Ground Truth* locations.

The solution which was proposed to increase the peformance of the A* algorithm did not compromise the results, although it cannot be assured anymore that they are the shortest paths, given their corresponding cost volumes. Using an Intel Core i7-4500U CPU 1.80@2.40GHz, the average run time was 15s. The most time consuming case took 52.7s.

Figures 5.39, 5.40 and 5.41 are examples of the retrieved paths. Figure 5.42 contains their 3D course along with the respective *Ground Truth*.

5.3.5 Summary

The intramuscular course of perforators is characterized by a low SNR and occasionally, it is invisible due to the imaging acquisition conditions. This poses high barriers for tracking based approaches, whose general formulation is not able to deal with such task effectively. Motivated by such problem, a minimum cost path approach was proposed. Different terrain costs were obtained by using the Frangi vesselness method to distinguish vessel from non-vessel voxels. As finding optimal paths in a 3D volume might pose high computational costs, the A* search method was used as well as a restriction to the maximum number of nodes allowed in the list of nodes to expand. The proposed framework successfully extracted the intramuscular course of the perforators, achieving a mean Euclidean distance error of 1.06mm, when comparing to the *Ground Truth* annotations. The average time required to find a path was 15s, using a Intel(R) Core(TM) i7-4500U CPU @1.80GHz 2.40GHz.

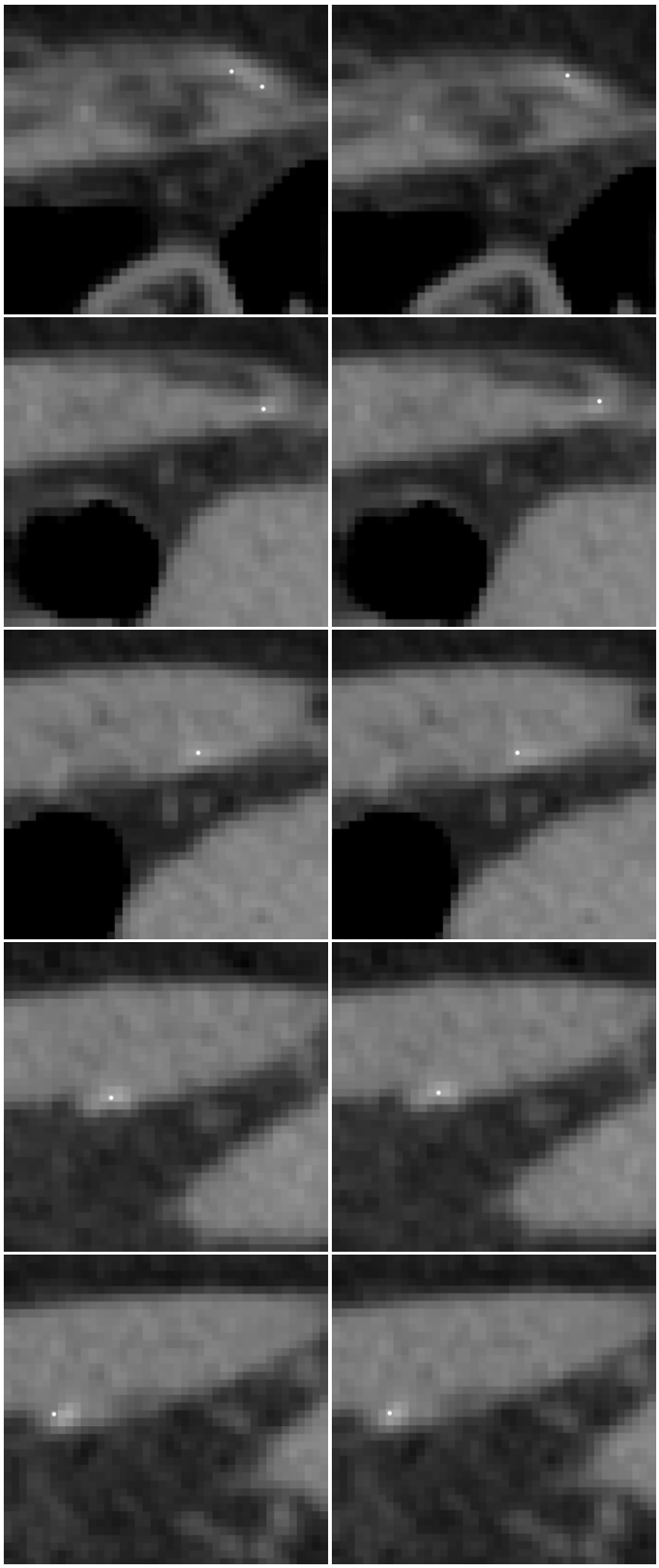

Figure 5.39: Slices of example case 1. Comparison between the *Ground Truth* (left column) and the extracted path (right column).

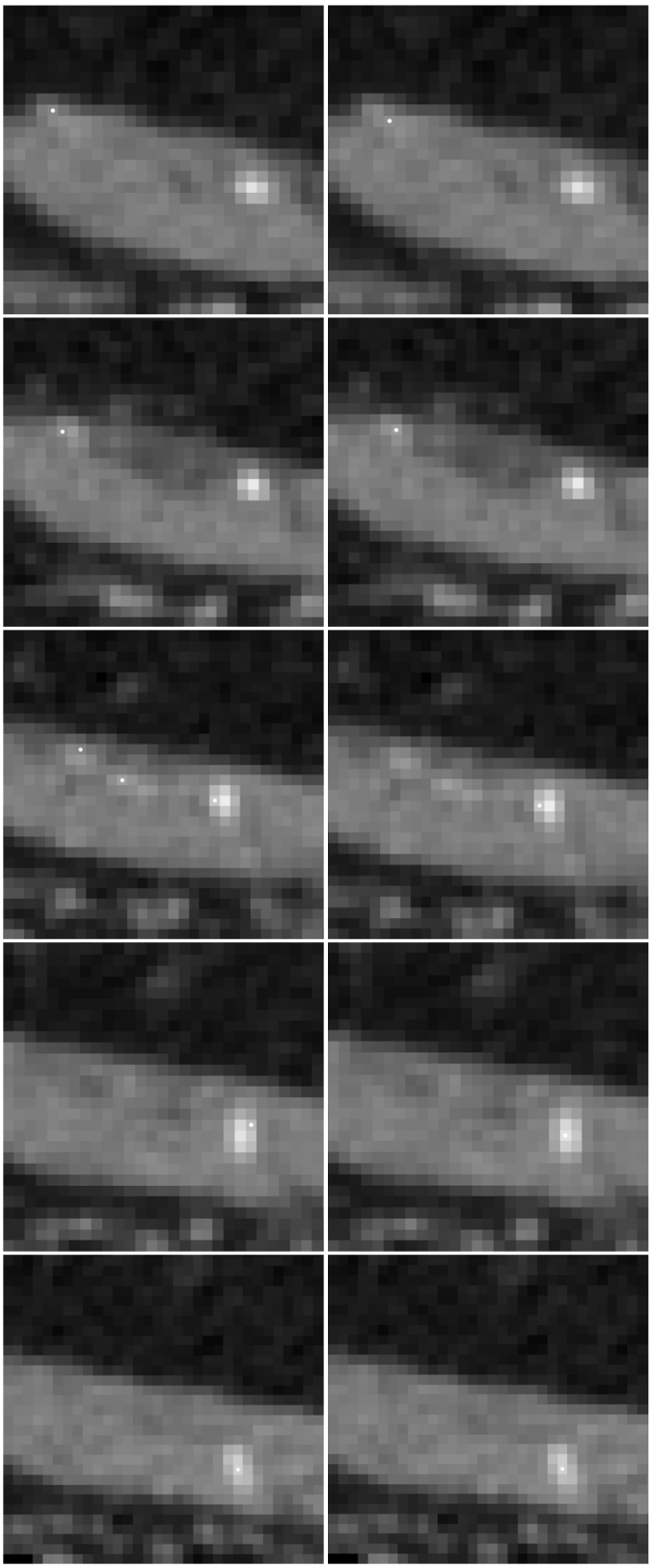

Figure 5.40: Slices of example case 2. Comparison between the *Ground Truth* (left column) and the extracted path (right column).

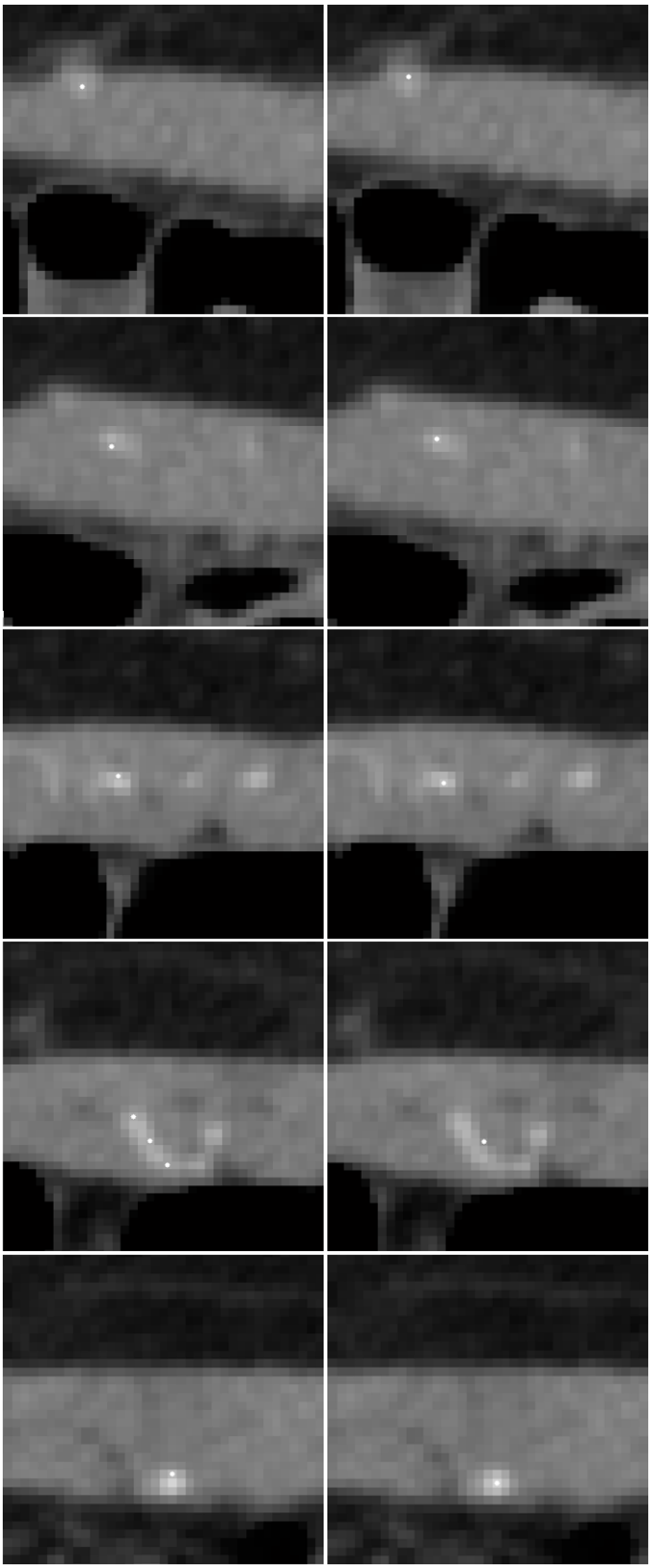

Figure 5.41: Slices of example case 3. Comparison between the *Ground Truth* (left column) and the extracted path (right column).

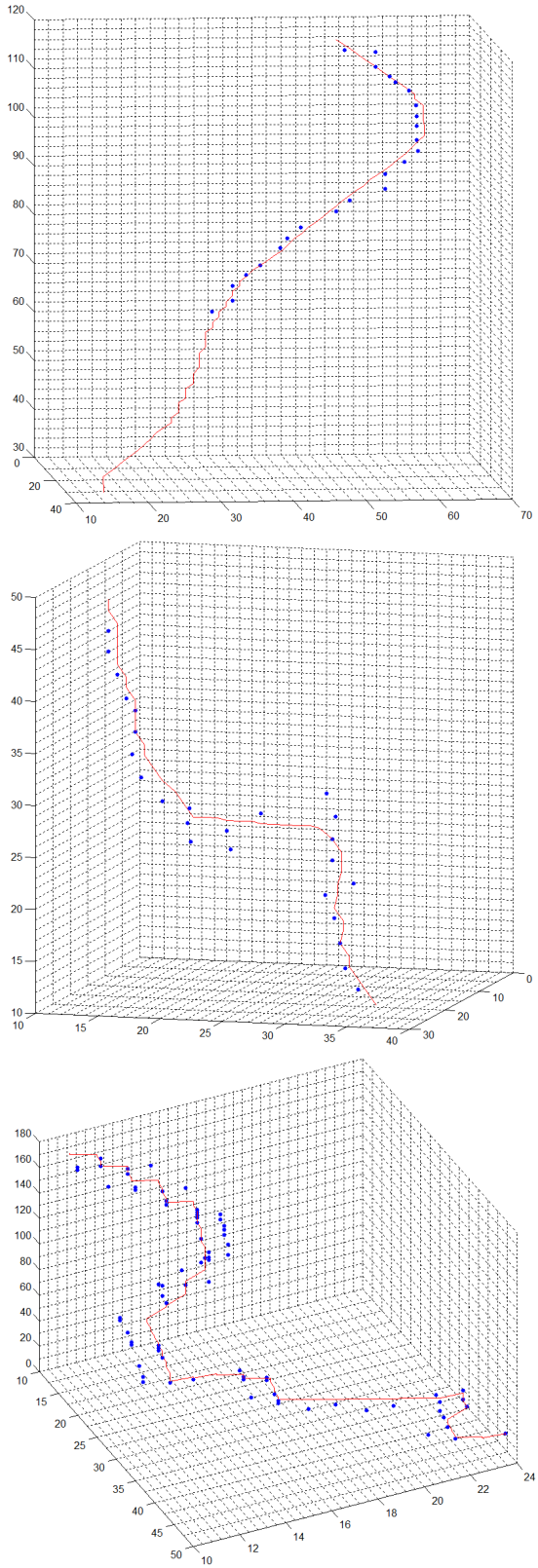

Figure 5.42: 3D comparison of the extracted perforator pathways (red) and *Ground Truth* (blue) of the examples used in Figures 5.39, 5.40 and 5.41, respectively.

Chapter 6

Conclusion

Breast reconstruction procedures have been providing women who removed breast(s) an opportunity to get closer to their normal lives. The different reconstruction options available are dependent of the specific patient condition and also of their preferences. Autologous tissue reconstructions allow to reshape the breast in a natural way and avoid foreign body reactions. DIEP flap is commonly regarded as the state-of-art method for autologous reconstruction, due to the higher preservation of abdominal capacity. As it involves microsurgery, it beneficiates from preoperative surgery planning based on imaging findings. Different imaging modalities have been used to perform those preoperative studies. Over the time, the state-of-art method has changed due to the evolution and proposal of new imaging modalities and new requirements brought with microsurgery evolution. CTA is widely recognized as the current state-of-art method for pre-operative analysis of the abdominal wall. Although preoperative imaging studies allow to visualize the target vessels, the evaluation of vessel course and diameter is still a subjective and non accurate procedure. The goal of this thesis was to make that analysis more objective, with the development of a CAD system which segments the target vessels and extracts the desired features in an objective manner.

The developed algorithm successfully detected the anterior *fascia*, which separates the subcutaneous region from the *rectus abdominis* muscle. This interface allowed to divide the detection of the perforators into two independent problems: detection of the subcutaneous and intramuscular courses. The first was correctly extracted by the Kalman filter, which fuses the local gradient vectors information with the 2D cross section vessel center estimation, in order to iteratively extract new centerline points. A mean error of 1.35 *mm* was achieved. Still, some perforators present a significant subcutaneous portion along the fascia, leading to a corruption of the local gradient vectors and, consequently, to the earlier end of the tracking procedure. The caliber estimation, in general, followed the findings contained in the reports. Even then, it has to be remembered that the space between consecutive voxels is usually around 0.7 - 0.9 *mm*, meaning that measuring calibers in the range of 2-3 *mm* is not a trivial task. Hence, measuring the interoperator variability would be very important to take more conclusions about the performance of the proposed caliber estimation. Finally, despite the low SNR of the intramuscular course of the perforators, the minimum cost path approach effectively extracted those pathways, achieving a mean error of 1.06 *mm*.

6.0.1 Future Work

The proposed methodology was able to surpass most of the challenges involved in the detection of the DIEA perforators. Nonetheless, some topics deserve attention in the future. Starting by the segmentation of the *fascia*, an effort to improve the robustness and accuracy of the first raw segmentation should be made. That would avoid the strong outliers that occasionally affected the raw results and lead to the use of a robust regression which has a higher computational cost than the general least-squares regression.

Considering now the subcutaneous tracking procedure, attention should be given to the perforators which present a significant course along the *fascia*. This makes the tracking method unstable at that region due to the corrupted local gradient vectors and it commonly stops earlier than it should, not retrieving the real coordinates of the region where the perforator leaves the fascia. Hence, a module which corrects this behavior or a different algorithm should be considered.

In terms of caliber estimation, different radiologists should provide the respective *Ground Truth*, in order to measure the interoperator variability and compare with the results achieved by the developed framework. Given the high subjectivity inherent to the caliber estimations, this is a very important point.

Finally, a software that renders the detected vessels and displays them with the volume data should be developed in the future.

Appendix A

Ground Truth annotation protocol

1. Download Fiji in http://fiji.sc/Downloads . There is an installation guide for Windows users in http://fiji.sc/Install_Fiji_on_Windows and Mac users in http://fiji.sc/Install_Fiji_on_MacOSX .

2. Open Fiji, then open the images (File -> Import -> Image Sequence).

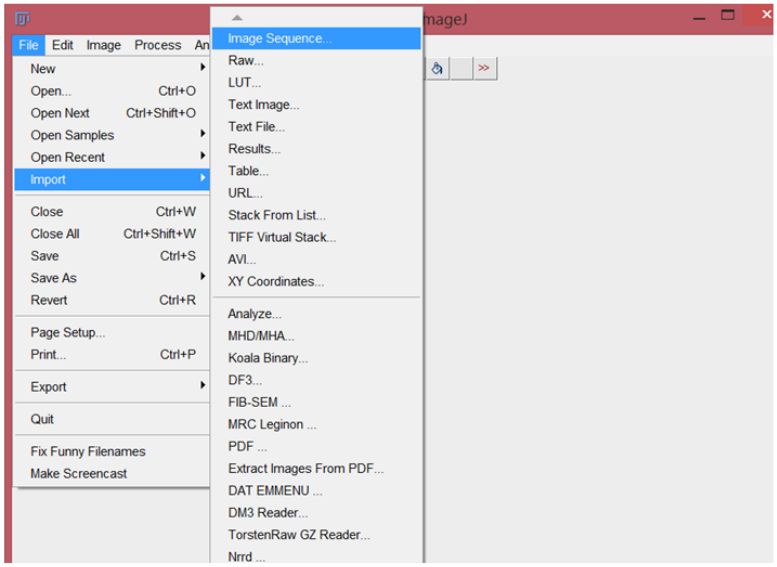

3. Select the folder that contains the images, select the first one and open it.

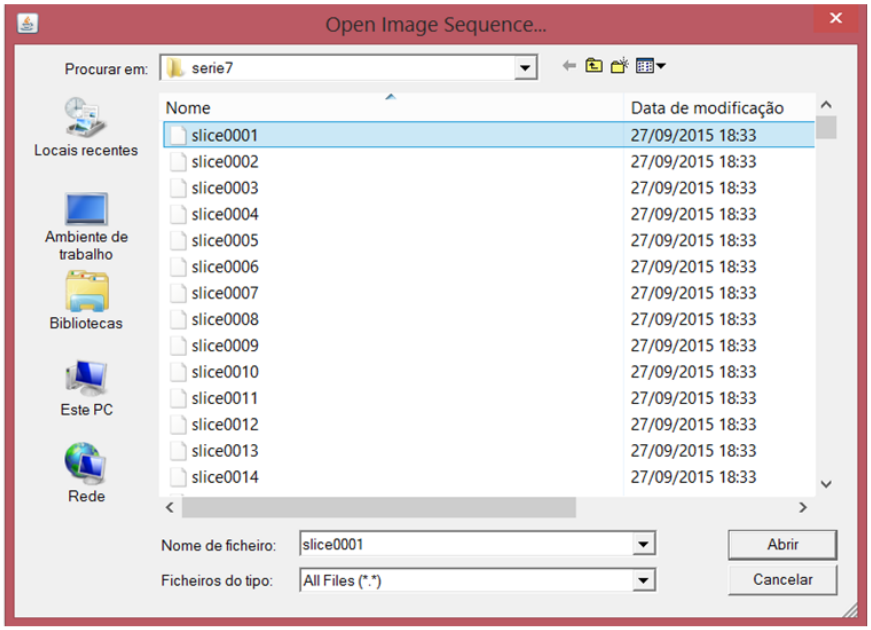

4. Click OK on the window that pops up.

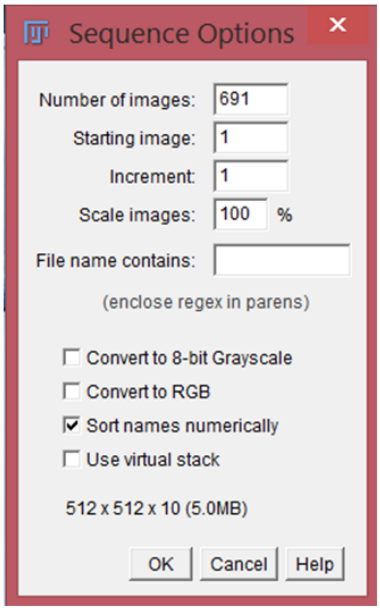

5. After opening the images, click on Plugins -> Analyze -> Cell counter.

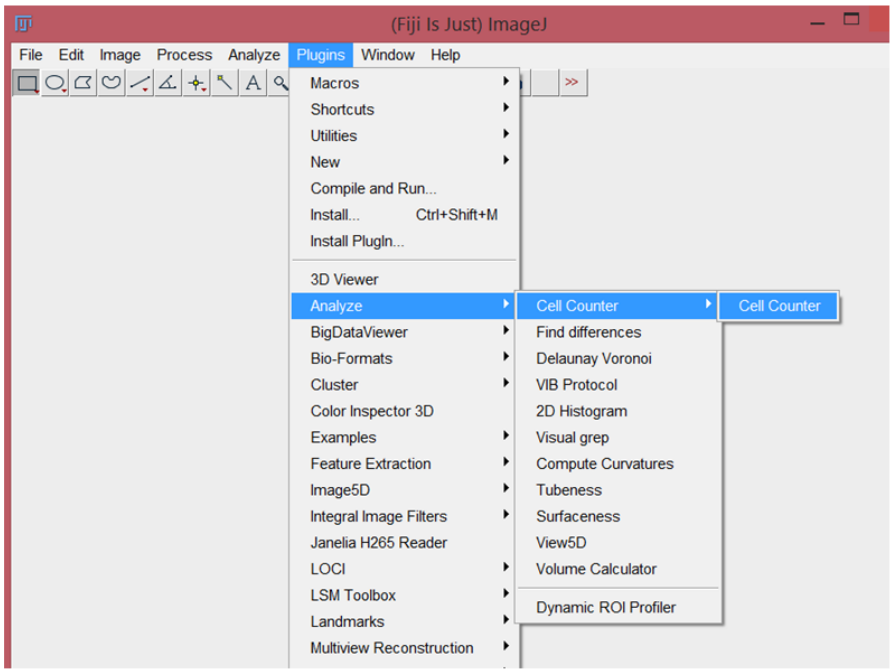

6. Click in Initialize and select Type 1 counter.

7. Uncheck the *Show numbers* box in order to only see the markers.

8. Start segmenting the images, as displayed below.

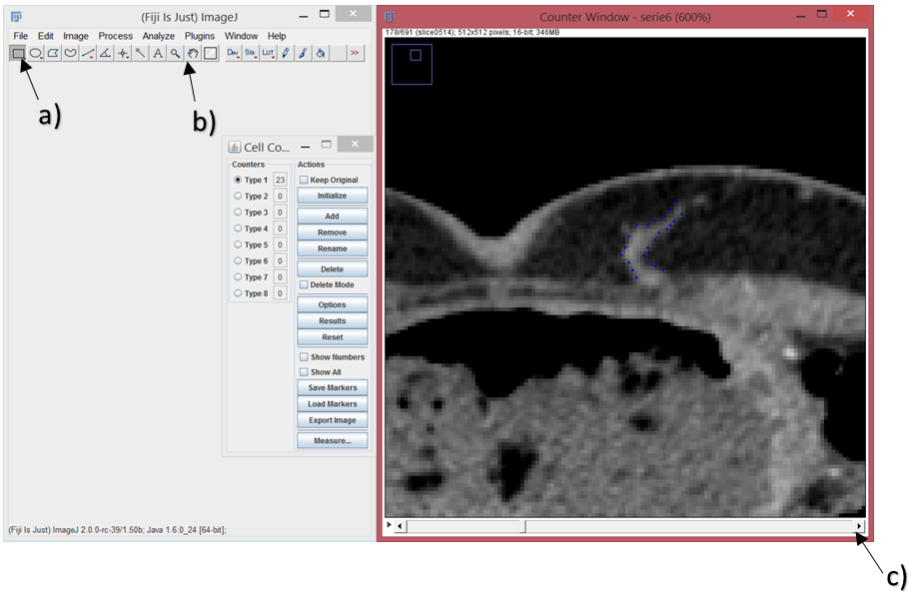

a. Marking tool (left or right click to leave annotations);
b. Zooming tool (left click to zoom in and right click to zoom out); If the zooming tool is not selected, you can perform a general zoom in with the '+' key and a zoom out with the '-' key.
c. Images navigation tool (mouse scroll can also be used).

9. In case you want to delete a marker, check the *Delete Mode* box to allow the marker closest to the mouse to be deleted when clicked on.

10. After segmenting the vasculature, switch to Type 7 counter and mark the umbilicus location.

11. After segmenting all the occurrences, click in *Measure*, and a new box with the position of the markers will appear. Click in *File -> Save as*, and save the XLS file as "XYZ_annotation.xls" where XYZ is the patient ID.

12. Save the markers in xml format as "XYZ_markers.xml", by clicking on the button *Save Markers* in the cell counter window. XYZ is once again the patient ID.

13. Close the program.

Later on, if you wish to make changes, follow the next instructions:

Repeat steps 2-6;
On the counter window, click on *Load Markers* and select the xml file containing the previous markers;
Make the desired changes;
Redo steps 9-11.

Appendix B

Fascia segmentation results

Table B.1: *Fascia* segmentation results for each of the individual volumes.

Patient	Method	Euclidean Distance (mm)		Hausdorff Distance (mm)		Time (s)
		GT → Seg	Seg → GT	GT → Seg	Seg → GT	
30335	normal	0.40	0.40	1.07	1.07	31.17
	robust	0.38	0.38	1.04	1.04	547.27
30905	normal	0.52	0.53	1.44	1.44	40.98
	robust	0.52	0.52	1.46	1.45	740.35
32398	normal	0.52	0.52	1.32	1.31	22.86
	robust	0.50	0.50	1.29	1.28	268.47
37758	normal	0.85	0.86	2.22	2.32	52.29
	robust	0.29	0.29	1.08	1.07	931.80
40108	normal	0.35	0.35	1.27	1.28	31.91
	robust	0.31	0.31	1.13	1.15	699.61
26049	normal	0.66	0.67	1.31	1.32	39.23
	robust	0.31	0.31	0.91	0.92	916.35
30243	normal	0.32	0.32	1.24	1.21	30.22
	robust	0.31	0.31	1.25	1.21	684.29
33422	normal	0.28	0.28	0.79	0.79	21.38
	robust	0.28	0.28	0.79	0.79	505.19
26645	normal	0.55	0.55	1.73	1.77	23.30
	robust	0.41	0.41	1.66	1.70	546.74
31347	normal	0.42	0.42	1.46	1.43	23.50
	robust	0.38	0.38	1.41	1.37	544.52
39245	normal	0.89	0.91	2.85	2.83	36.37
	robust	0.57	0.58	2.20	2.26	906.07
40335	normal	0.46	0.46	1.80	1.80	28.85
	robust	0.39	0.39	1.68	1.71	677.05
40651	normal	0.32	0.32	1.06	1.06	21.08
	robust	0.30	0.30	1.00	1.00	496.78

Patient	**Method**	**Euclidean Distance (mm)**		**Hausdorff Distance (mm)**		**Time (s)**
		GT → Seg	**Seg → GT**	**GT → Seg**	**Seg → GT**	
6722	normal	0.70	0.70	1.70	1.72	31.52
	robust	0.63	0.64	1.31	1.32	705.05
8964	normal	0.44	0.45	1.38	1.38	25.43
	robust	0.34	0.34	1.08	1.08	587.82
16338	normal	0.84	0.87	2.64	2.77	33.58
	robust	0.57	0.58	2.26	2.44	536.28
3149	normal	0.68	0.68	1.88	1.88	33.41
	robust	0.51	0.51	1.64	1.67	775.08
4321	normal	1.92	2.22	4.20	5.85	25.80
	robust	1.78	2.15	4.25	6.13	581.09
7335	normal	0.88	0.90	2.77	2.77	28.69
	robust	0.67	0.68	1.93	2.02	640.25
12775	normal	0.42	0.42	1.32	1.34	18.64
	robust	0.38	0.38	1.03	1.03	434.14

Appendix C

Perforator subcutaneous region tracking results

Table C.1: Results obtained using the proposed tracking framework to detect the subcutaneous region of each perforator. For some cases, the caliber was not available at the report, such that the error could not be measured.

Case	Path error (mm)		Caliber error		Location error (mm)	
	Euclidean distance	Hausdorff distance	Relative	Absolute (mm)	height	width
4321-P1	0.96	1.30	5.2%	0.12	2.30	3.07
4321-P2	1.39	3.48	17.8%	0.32	1.54	0
4321-P3	0.85	1.77	8.9%	0.16	0.77	2.30
4321-P4	1.24	2.45	15.1%	0.32	0	1.54
6722-P1	2.74	8.98	-	-	1.40	4.20
6722-P2	0.99	2.54	9.5%	0.19	2.10	0.70
6722-P3	1.01	2.35	7.3%	0.22	0.70	0
7335-P1	1.35	2.44	-	-	0.98	0.98
7335-P2	0.94	1.36	11.5%	0.23	0	3.91
7335-P3	1.14	3.82	52.5%	1.05	1.95	0.98
7335-P4	1.17	1.91	37.0%	0.74	0.98	0
7335-P5	1.57	2.86	-	-	1.95	0
8964-P1	1.27	2.25	13.6%	0.34	0.85	1.70
8964-P2	1.53	3.13	6.4%	0.16	2.55	0.85
8964-P3	3.44	6.74	7.5%	0.15	4.25	4.25
8964-P4	1.01	1.68	9.2%	0.22	0.85	0
16338-P1	1.70	5.05	18.9%	0.53	0	0.8
16338-P2	1.04	1.47	1.5%	0.03	1.60	6.42
16338-P3	1.09	2.06	10.5%	0.21	0.80	0.80

Case	Path error (mm)		Caliber error		Location error (mm)	
	Euclidean distance	Hausdorff distance	Relative	Absolute (mm)	height	width
16338-P4	1.18	1.62	10.0%	0.30	0.80	1.60
16338-P5	1.91	5.66	7.3%	0.16	3.21	4.82
31347-P1	0.97	1.39	3.5%	0.09	0.45	0.76
31347-P2	1.20	1.78	10.0%	0.22	0.83	0
31347-P3	1.18	2.17	0.9%	0.02	2.49	1.66
31347-P4	1.90	3.68	12.4%	0.21	0.83	0.83
31347-P5	2.30	4.90	12.7%	0.28	0.83	3.23
31347-P6	2.22	7.55	11.0%	0.21	0.83	5.81
39245-P1	1.66	4.25	13.3%	0.32	1.71	3.88
39245-P2	1.13	2.88	8.9%	0.24	0	0
39245-P3	1.58	3.19	6.9%	0.20	0	0.83
39245-P4	2.41	4.51	16.2%	0.47	0.83	0.83
40335-P1	1.15	2.51	9.5%	0.19	0.81	0.81
40335-P2	1.22	3.12	25.7%	0.77	0	1.62
40335-P3	1.03	2.79	15.0%	0.45	0.81	0.81
40335-P4	1.08	3.01	6.4%	0.16	2.44	1.62
40335-P5	1.29	2.65	14.0%	0.35	2.04	1.22
26049-P1	1.39	3.33	20.8%	0.50	2.94	1.54
26049-P5	1.79	4.16	22.0%	0.44	1.07	3.21
26049-P6	1.26	1.97	14.7%	0.28	5.65	0.40
26049-P7	2.07	4.72	28.8%	0.72	7.76	2.26
30243-P1	1.28	5.06	4.6%	0.11	4.93	0.75
30243-P2	1.13	3.19	0.4%	0.01	1.79	2.40
30243-P4	1.11	3.19	1.5%	0.03	3.71	3.59
30243-P6	1.19	2.40	-	-	0.57	2.18
30335-P1	1.64	3.67	8.6%	0.18	0.15	3.66
30335-P2	1.03	1.86	66.2%	0.86	0.71	1.95
30335-P3	1.04	1.87	2.4%	0.05	0.97	0.91
30335-P4	0.94	2.21	6.3%	0.17	0.58	0.60
30335-P5	1.57	3.97	25.6%	0.64	0.05	3.97
30905-P1	1.15	2.65	63.9%	1.15	0.08	2.34
30905-P2	1.08	2.10	32.8%	0.92	0.38	1.52
30905-P3	1.41	3.51	7.7%	0.17	0.53	3.35
30905-P4	1.19	1.86	5.8%	0.11	0.68	0.20
33422-P1	1.80	4.28	5.8%	0.14	1.04	4.08
33422-P2	1.32	2.30	18.4%	0.46	1.84	1.07
33422-P3	1.02	1.56	20.8%	0.54	2.34	0.02
33422-P4	1.05	1.98	17.0%	0.39	0.29	1.78
33422-P5	1.72	2.20	26.7%	0.48	0.93	1.59
35735-P1	1.22	2.29	18.0%	0.36	2.30	1.66
37758-P1	1.09	2.28	4.0%	0.08	0.07	1.08
37758-P2	1.21	2.14	18.4%	0.46	0.49	1.31
37758-P3	1.22	1.91	27.4%	0.63	0.24	0.45
37758-P5	1.83	3.41	30.6%	0.95	2.83	1.06

Case	Path error (mm)		Caliber error		Location error (mm)	
	Euclidean distance	**Hausdorff distance**	**Relative**	**Absolute (mm)**	**height**	**width**
40108-P1	1.44	4.33	7.7%	0.20	0.33	1.05
40108-P2	1.02	2.76	11.5%	0.31	1.42	0.86
40108-P3	1.65	5.06	27.6%	0.94	1.65	4.75
40108-P4	0.94	1.64	16.2%	0.42	0.92	0.98
40108-P5	1.20	2.15	14.6%	0.38	0.04	0.68
40108-P6	0.73	1.00	14.5%	0.48	2.24	0.80
40108-P7	0.76	1.26	13.8%	0.33	2.15	1.07
40651-P1	0.87	2.02	8.3%	0.19	2.78	0.57
40651-P2	1.20	3.00	9.0%	0.19	1.03	0.96
40651-P6	1.20	2.55	0.8%	0.02	0.60	0.66
40651-P7	1.47	3.57	36.7%	0.66	0.77	3.35

Appendix D

Perforator intramuscular course detection results

Table D.1: Results of the method proposed for the extraction of the intramuscular course of perforators.

Case	Euclidean distance (mm)	Hausdorff distance (mm)	Time (s)
1	0.89	2.59	31.75
2	1.25	2.90	5.09
3	0.99	2.43	16.90
4	1.64	2.18	3.28
5	1.95	4.88	1.14
6	0.82	2.08	2.12
7	1.15	4.25	48.84
8	0.82	1.47	20.25
9	1.08	3.50	8.73
10	0.94	2.27	1.38
11	0.77	2.54	19.76
12	1.18	2.41	13.03
13	0.79	1.66	28.69
14	0.57	1.17	24.23
15	1.02	3.02	12.97
16	0.70	1.42	22.06
17	0.75	1.42	6.04
18	0.70	2.13	52.70
19	0.89	1.66	14.67
20	0.91	1.44	12.58
21	0.95	1.50	1.14
22	0.91	1.44	7.47
23	1.08	2.61	1.48

Case	**Euclidean distance (mm)**	**Hausdorff distance (mm)**	**Time (s)**
24	1.03	2.49	9.32
25	1.00	2.66	50.79
26	1.08	2.51	8.40
27	1.62	2.95	2.76
28	1.37	3.20	1.56
29	0.97	1.78	24.85
30	1.67	4.38	4.81
31	1.44	2.57	6.06

References

[1] R. Siegel, K. Miller, and A. Jemal. Global cancer statistics. *A Cancer Journal for Clinicians*, 65(1):5–29, 2015.

[2] J. Ferlay, I. Soerjomataram, M. Ervik, R. Dikshit, S. Eser, C. Mathers, M. Rebelo, D. Parkin, D. Forman, and F. Bray. *GLOBOCAN 2012 v1.0, Cancer Incidence and Mortality Worldwide: IARC CancerBase No. 11*. Lyon, France: International Agency for Research on Cancer, 2013. Available: `http://globocan.iarc.fr`, Accessed: 2016 January.

[3] M. Hewitt, R. Herdman, and J. Holland. *Meeting psychosocial needs of women with breast cancer*. The National Academies Press, 2004.

[4] A. Lichter, M. Lippman, D. Danforth, T. Angelo, S. Steinberg, E. deMoss, H. MacDonald, C. Reichert, M. Merino, S. Swain, K. Cowan, L. Gerber, J. Bader, P. Findlay, W. Schain, C. Gorrell, K. Straus, S. Rosenberg, and E. Glatstein. Mastectomy versus breast-conserving therapy in the treatment of stage I and II carcinoma of the breast: a randomized trial at the National Cancer Institute. *Journal of Clinical Oncology*, 10(6):976–983, 1992.

[5] K. P. McGuire, A. A. Santillan, P. Kaur, T. Meade, J. Parbhoo, M. Mathias, C. Shamehdi, M. Davis, D. Ramos, and C. E. Cox. Are Mastectomies on the Rise? A 13-Year Trend Analysis of the Selection of Mastectomy Versus Breast Conservation Therapy in 5865 Patients. *Annals of Surgical Oncology*, 16(10):2682–2690, 2009.

[6] A. E. Dragun, B. Huang, T. C. Tucker, and W. J. Spanos. Increasing mastectomy rates among all age groups for early stage breast cancer: A 10-year study of surgical choice. *Breast Journal*, 18(4):318–325, 2012.

[7] U. Mahmood, A. L. Hanlon, M. Koshy, R. Buras, S. Chumsri, K. H. Tkaczuk, S. B. Cheston, W. F. Regine, and S. J. Feigenberg. Increasing national mastectomy rates for the treatment of early stage breast cancer. *Annals of surgical oncology*, 20(5):1436–43, 2013.

[8] B. Wexelman, J. A. Schwartz, D. Lee, A. Estabrook, and A. M. Ma. Socioeconomic and Geographic Differences in Immediate Reconstruction after Mastectomy in the United States. *The Breast Journal*, 20(4):339–346, 2014.

[9] A. Cina, M. Salgarello, L. Barone-Adesi, P. Rinaldi, and L. Bonomo. Planning breast reconstruction with deep inferior epigastric artery perforating vessels: multidetector CT angiography versus Color Doppler US. *Radiology*, 255(3):979–987, 2010.

[10] T. J. Phillips, D. L. Stella, W. M. Rozen, M. Ashton, and G. I. Taylor. Abdominal wall CT angiography: a detailed account of a newly established preoperative imaging technique. *Radiology*, 249:32–44, 2008.

[11] F. M. Pinel-Giroux, M. M. El Khoury, I. Trop, C. Bernier, J. David, and L. Lalonde. Breast Reconstruction: Review of Surgical Methods and Spectrum of Imaging Findings. *Radiographics*, 33:435–453, 2013.

[12] N. Blondeel, G. G. Vanderstraeten, S. J. Monstrey, K. Van Landuyt, P. Tonnard, R. Lysens, W. D. Boeckx, and G. Matton. The donor site morbidity of free DIEP flaps and free TRAM flaps for breast reconstruction. *British Journal of Plastic Surgery*, 50(5):322–330, 1997.

[13] G. F. Pratt, W. M. Rozen, D. Chubb, M. W. Ashton, A. Alonso-Burgos, and I. S. Whitaker. Preoperative imaging for perforator flaps in reconstructive surgery: a systematic review of the evidence for current techniques. *Annals of Plastic Surgery*, 69(1):1–7, 2012.

[14] J. Masia, J. Larrañaga, J. A. Clavero, L. Vives, G. Pons, and J. M. Pons. The value of the multidetector row computed tomography for the preoperative planning of deep inferior epigastric artery perforator flap: our experience in 162 cases. *Annals of plastic surgery*, 60(1):29–36, 2008.

[15] R. L. Drake, A. W. Vogl, and A. W. M. Mitchell. *Gray's Anatomy for Students*. Elsevier Health Sciences, 2nd edition, 2009.

[16] H. Gray. *Anatomy of the human body*. Philadelphia: Lea & Febiger, 1918; Bartleby.com, 2000, 2000.

[17] `http://www.breastcancer.org/`, Accessed: 2015-11-19.

[18] A. K. Bajaj, P. M. Chevray, and D. W. Chang. Comparison of donor-site complicantion and functional outcomes in free muscle-sparing TRAM flap and free DIEP flap breast reconstruction. *Plastic and Reconstructive Surgery*, 117, 2006.

[19] C. M. Futter, M. H. Webster, S. Hagen, and S. L. Mitchell. A retrospective comparison of abdominal muscle strength following breast reconstruction with a free TRAM or DIEP flap. *British journal of plastic surgery*, 53(7):578–583, 2000.

[20] W. M. Rozen, K. P. Palmer, H. Suami, W. R. Pan, M. W. Ashton, R. J. Corlett, and G. I. Taylor. The DIEA branching pattern and its relationship to perforators: the importance of preoperative computed tomographic angiography for DIEA perforator flaps. *Plastic and reconstructive surgery*, 121(2):367–73, 2008.

[21] G. I. Taylor, M. Doyle, and G. McCarten. The Doppler probe for planning flaps: anatomical study and clinical applications. *British Journal of Plastic Surgery*, 43(1):1–16, 1990.

[22] R. E. Giunta, A. Geisweid, and A. M. Feller. The Value of Preoperative Doppler Sonography for Planning Free Perforator Flaps. *Plastic & Reconstructive Surgery*, 105(7):2381–2386, 2000.

[23] P. N. Blondeel, G. Beyens, R. Verhaeghe, K. Van Landuyt, P. Tonnard, S. J. Monstrey, and G. Matton. Doppler flowmetry in the planning of perforator flaps. *British Journal of Plastic Surgery*, 51(3):202–209, 1998.

[24] A. Tsukino, K. Kurachi, T. Inamiya, and T. Tanigaki. Preoperative Color Doppler assessment in planning of anterolateral thigh flaps. *Plastic and Reconstructive Surgery*, 113(1):241–246, 2004.

[25] J. Masia, J. A. Clavero, J. R. Larrañaga, X. Alomar, G. Pons, and P. Serret. Multidetector-row computed tomography in the planning of abdominal perforator flaps. *Journal of Plastic, Reconstructive and Aesthetic Surgery*, 59(6):594–599, 2006.

[26] T. J. Phillips, D. L. Stella, W. M. Rozen, M. Ashton, and G. I. Taylor. Abdominal wall CT angiography: a detailed account of a newly established preoperative imaging technique. *Radiology*, 249(1):32–44, 2008.

[27] R. J. Shaw, M. D. Batstone, T. K. Blackburn, and J. S. Brown. Preoperative Doppler assessment of perforator anatomy in the anterolateral thigh flap. *British Journal of Oral and Maxillofacial Surgery*, 48(6):419–422, 2010.

[28] U. D. Khan and J. G. Miller. Reliability of handheld Doppler in planning local perforator-based flaps for extremities. *Aesthetic Plastic Surgery*, 31(5):521–525, 2007.

[29] W. M. Rozen, T. J. Phillips, M. W. Ashton, D. L. Stella, R. N. Gibson, and G. I. Taylor. Preoperative imaging for DIEA perforator flaps: a comparative study of computed tomographic angiography and Doppler ultrasound. *Plastic and reconstructive surgery*, 121(1):9–16, 2008.

[30] W. Rozen, H. Anavekar, M. Ashton, D. Stella, D. Grinsell, R. Bloom, and G. Taylor. Does the preoperative imaging of perforators with CT angiography improve operative outcomes in breast reconstruction? *Microsurgery*, 28(7):516–523, 2008.

[31] J. M. Smit, A. Dimopoulou, A. G. Liss, C. J. Zeebregts, M. Kildal, I. S. Whitaker, A. Magnusson, and R. Acosta. Preoperative CT angiography reduces surgery time in perforator flap reconstruction. *Journal of Plastic, Reconstructive & Aesthetic Surgery*, 62(9):1112–1117, 2009.

[32] W. M. Rozen, D. Ribuffo, M. Atzeni, D. L. Stella, L. Saba, M. Guerra, D. Grinsell, and M. W. Ashton. Current state of the art in perforator flap imaging with computed tomographic angiography. *Surgical and Radiologic Anatomy*, 31(8):631–639, 2009.

[33] W. Rozen, D. Stella, and J. Bowden. Advances in the pre-operative planning of deep inferior epigastric artery perforator flaps: magnetic resonance angiography. *Microsurgery*, 29:119–123, 2009.

[34] D. Lesage, E. D. Angelini, I. Bloch, and G. Funka-Lea. A review of 3D vessel lumen segmentation techniques: Models, features and extraction schemes. *Medical Image Analysis*, 13(6):819–845, 2009.

[35] T. Boskamp, D. Rinck, F. Link, B. Kümmerlen, G. Stamm, and P. Mildenberger. New vessel analysis tool for morphometric quantification and visualization of vessels in CT and MR imaging data sets. *Radiographics : a review publication of the Radiological Society of North America, Inc*, 24:287–297, 2004.

[36] R. Sebbe, E. Coche, B. Gosselin, and B. Macq. Pulmonary Arteries Segmentation and Feature Extraction through Slice Marching. *Proc. ProRISC 2003, 14th Annual Workshop on Circuits, Systems, and Signal Processing*, pages 233–242, 2003.

[37] S. Wesarg and E. A. Firle. Segmentation of Vessels : The Corkscrew Algorithm. *Proceedings of SPIE*, pages 1–12, 2004.

[38] C. Florin, N. Paragios, and J. Williams. Particle filters, a quasi-monte-carlo-solution for segmentation of coronaries. *Lecture Notes in Computer Science (including subseries Lecture Notes in Artificial Intelligence and Lecture Notes in Bioinformatics)*, 3749 LNCS:246–253, 2005.

[39] R. Manniesing and W. Niessen. Local speed functions in level set based vessel segmentation. *Medical Image Computing and Computer Assisted Intervention Proceedings*, 2004.

[40] Y. Yang, A. Tannenbaum, D. Giddens, and W. Coulter. Knowledge-based 3D segmentation and reconstruction of coronary arteries using CT images. *Annual International Conference of the IEEE Engineering in Medicine and Biology Society. IEEE Engineering in Medicine and Biology Society. Conference*, 3:1664–6, 2004.

[41] M. Schaap, R. Manniesing, I. Smal, T. van Walsum, A. van der Lugt, and W. Niessen. Bayesian tracking of tubular structures and its application to carotid arteries in CTA. *Medical image computing and computer-assisted intervention*, 10(Pt 2):562–570, 2007.

[42] A. F. Frangi, W. J. Niessen, R. M. Hoogeveen, T. van Walsum, and M. A. Viergever. Model-based quantitation of 3-D magnetic resonance angiographic images. *IEEE Transactions on Medical Imaging*, 18(10):946–956, 1999.

[43] A. F. Frangi, W. J. Niessen, P. J. Nederkoorn, O. E. H. Elgersma, and M. A. Viergever. Three-dimensional model-based stenosis quantification of the carotid arteries from contrast-enhanced MR angiography. *IEEE Mathematical Methods in Biomedical Image Analysis Proceedings*, 00(c):110–118, 2000.

[44] M. de Bruijne, B. van Ginneken, M. A. Viergever, and W. J. Niessen. Adapting Active Shape Models for 3D Segmentation of Tubular Structures in Medical Images. *Information Processing in Medical Imaging*, 18:136–147, 2003.

[45] C. Lacoste, G. Finet, and I. E. E. Magnin. Coronary Tree Extraction from X-Ray Angiograms Using Marked Point Processes. *3rd IEEE International Symposium on Biomedical Imaging: Macro to Nano, 2006.*, pages 157–160, 2006.

[46] K. Krissian, G. Malandain, N. Ayache, R. Vaillant, and Y. Trousset. Model-Based Detection of Tubular Structures in 3D Images. *Computer Vision and Image Understanding*, 80(2):130–171, 2000.

[47] C. Boldak, Y. Rolland, and C. Toumoulin. An improved model-based vessel tracking algorithm with application to Computed Tomography Angiography. *Journal of Biocybernetics and Biomedical Engineering*, 23(1):41–63, 2003.

[48] S. Wörz and K. Rohr. Segmentation and quantification of human vessels using a 3-D cylindrical intensity model. *IEEE Transactions on Image Processing*, 16(8):1994–2004, 2007.

[49] S. R. Aylward and E. Bullitt. Initialization, noise, singularities, and scale in height ridge traversal for tubular object centerline extraction. *IEEE Transactions on Medical Imaging*, 21(2):61–75, 2002.

[50] Y. Fridman, S. M. Pizer, S. Aylward, and E. Bullitt. Segmenting 3D Branching Tubular Structures Using Cores. *Medical Image Computing and Computer-Assisted Intervention*, 2879:570–577, 2003.

[51] S. Aylward, E. Bullitt, S. Pizer, and D. Eberly. Intensity ridge and widths for tubular object segmentation and description. *Proceedings of the Workshop on Mathematical Methods in Biomedical Image Analysis*, pages 131–138, 1996.

[52] A. Larralde, C. Boldak, M. Garreau, C. Toumoulin, D. Boulmier, Y. Rolland, H. Sud, and C. Beaulieu. Evaluation of a 3D Segmentation Software for the Coronary Characterization in Multi-slice Computed. *Evaluation*, pages 39–51, 2003.

[53] A. Vasilevskiy and K. Siddiqi. Flux maximizing geometric flows. *IEEE Transactions on Pattern Analysis and Machine Intelligence*, 24(12):1565–1578, 2002.

[54] A. F. Frangi, W. J. Niessen, K. L. Vincken, and M. A. Viergever. Multiscale vessel enhancement filtering. *Medial Image Computing and Computer-Assisted Invervention - MICCAI'98. Lecture Notes in Computer Science, vol 1496*, 1496:130–137, 1998.

[55] Q. Li, S. Sone, and K. Doi. Selective enhancement filters for nodules, vessels, and airway walls in two- and three-dimensional CT scans. *Medical physics*, 30(8):2040–2051, 2003.

[56] G. Agam, S. G. Armato, and C. Wu. Vessel tree reconstruction in thoracic CT scans with application to nodule detection. *IEEE Transactions on Medical Imaging*, 24(4):486–499, 2005.

[57] M. H. Hoyos, P. Orłowski, E. Piątkowska-Janko, P. Bogorodzki, and M. Orkisz. Vascular Centerline Extraction in 3D MR Angiograms for Phase Contrast MRI Blood Flow Measurement. *International Journal of Computer Assisted Radiology and Surgery*, 1(1):51–61, 2006.

[58] O. Friman, M. Hindennach, and H. Peitgen. Template-based multiple hypothesis tracking of small vessels. *International Symposium on Biomedical Imaging*, 2(2):2008–2011, 2008.

[59] T. Behrens, K. Rohr, and H. S. Stiehl. Segmentation of Tubular Structures in 3D Images Using a Combination of the Hough Transform and a Kalman Filter. *DAGM Symposium in Pattern Recognition Proceedings*, pages 406–413, 2001.

[60] M. A. Gulsun and H. Tek. Robust vessel tree modeling. *Lecture Notes in Computer Science (including subseries Lecture Notes in Artificial Intelligence and Lecture Notes in Bioinformatics)*, pages 602–611, 2008.

[61] O. Wink, W. J. Niessen, and M.A. Viergever. Fast delineation and visualization of vessels in 3-D angiographic images. *IEEE Transactions on Medical Imaging*, 19(4):337–346, 2000.

[62] S. Y. Wan and W. E. Higgins. Symmetric region growing. *IEEE Transactions on Image Processing*, 12(9):1007–1015, 2003.

[63] C. Metz, M. Schaap, A. van der Giessen, T. van Walsum, and W. Niessen. Semi-automatic coronary artery centerline extraction in computed tomography angiography data. *IEEE International Symposium Biomedical Imaging Proceedings*, 2007.

[64] W. Cai, F. Dachille, G. Harris, and H. Yoshida. Vesselness propagation: a fast interactive vessel segmentation method. *SPIE Medical Imaging Proceedings*, 2006.

[65] C. Kirbas and F. K. H. Quek. Vessel extraction in medical images by 3D wave propagation and traceback. *Proceedings - 3rd IEEE Symposium on BioInformatics and BioEngineering, BIBE 2003*, pages 174–181, 2003.

[66] C. Lorenz, S. Renisch, T. Schlathoelter, and T. Buelow. Simultaneous segmentation and tree reconstruction of the coronary arteries in MSCT images. *SPIE Medical Imaging Proceedings*, 2003.

[67] H. Delingette and J. Montagnat. Shape and Topology Constraints on Parametric Active Contours. *Computer Vision and Image Understanding*, 83(2):140–171, 2001.

[68] T. McInerney and D. Terzopoulos. T-snakes: topology adaptive snakes. *Medical image analysis*, 4(2):73–91, 2000.

[69] R. Toledo, X. Orriols, X. Binefa, P. Radeva, J. Vitrià, and J. J. Villanueva. Tracking elongated structures using statistical snakes. *Computer Vision and Pattern Recognition*, pages 157–162, 2000.

[70] P. J. Yim, J. J. Cebral, R. Mullick, H. B. Marcos, and P. L. Choyke. Vessel surface reconstruction with a tubular deformable model. *IEEE Transactions on Medical Imaging*, 20(12):1411–1421, 2001.

[71] E. Angelini, Y. Jin, and Y. Laine. *Handbook of Biomedical Image Analysis - Registration models*, pages 47–102. Kluwer Academic / Plenum Publishers, 2005.

[72] A. F. Frangi, W. J. Niessen, R. M. Hoogeven, T. van Walsum, and M. A. Viergever. Quantitation of vessel morphology from 3D MRA. *Medical Image Computing and Computer-Assisted Intervention*, 1679:358–367, 1999.

[73] O. Wink, W. J. Niessen, B. Verdonck, and M. A. Viergever. Vessel axis determination using wave front propagation analysis. *Medical Image Computing and Computer Assisted Intervention Proceedings*, 2001.

[74] S. Young, V. Pekar, and J. Weese. Vessel segmentation for visualization of MRA with blood pool contrast agent. *SPIE Medical Imaging Proceedings*, 2001.

[75] L. Hua and A. Yezzi. Vessels as 4-D curves: Global minimal 4-D paths to extract 3-D tubular surfaces and centerlines. *IEEE Transactions on Medical Imaging*, 26(9):1213–1223, 2007.

[76] P. J. Yim, P. L. Choyke, and R. M. Summers. Gray-scale skeletonization of small vessels in magnetic resonance angiography. *IEEE Transactions on Medical Imaging*, 19(6):568–576, 2000.

[77] J. Schindelin, I. Arganda-carreras, and E. Frise. Fiji: an open-source platform for biological-image analysis. *Nature methods*, 9:676–682, 2012.

[78] Mango. `http://ric.uthscsa.edu/mango/index.html`, Accessed: 2015-09-25.

[79] Seg3d. `http://www.sci.utah.edu/cibc-software/seg3d.html`, Accessed: 2015-09-25.

[80] Mipav. `http://mipav.cit.nih.gov/`, Accessed: 2015-09-25.

[81] N. Otsu. A threshold selection method from gray-level histograms. *IEEE Transactions on Systems, Man, and Cybernetics*, 9(1):62–66, 1979.

[82] R. E. Kalman. A New Approach to Linear Filtering and Prediction Problems. *Journal of Basic Engineering*, 82(1):35, 1960.

[83] H. P. Oliveira, J. S. Cardoso, A. T. Magalhães, and M. J. Cardoso. A 3D low-cost solution for the aesthetic evaluation of breast cancer conservative treatment. *Computer Methods in Biomechanics and Biomedical Engineering: Imaging & Visualization*, 2(2):90–106, 2014.

[84] P. Kovesi. Phase preserving denoising of images. *DICTA '99: Fifth International/National Biennial Conference on Digital Image Computing, Techniques and Applications*, pages 212–7, 1999.

[85] A. Denewer, E. E. Hamed, A. Khater, S. Zidan, S. Roshdy, M. Shetiwy, F. Shahatto, O. Farouk, A. Senbel, A. Fathi, F. Denewer, and A. Badrawy. The efficacy of preoperative perforators mapping for choice of the side of pedicled tram in breast reconstruction. *American Journal of Breast Cancer Research*, 2(1):1–8, 2015.

[86] P. E. Hart, N. J. Nilsson, and B. Raphael. A formal basis for the heuristic determination of minimum cost paths. *IEEE Transactions on Systems, Science, and Cybernetics*, SSC-4(2):100–107, 1968.